

RENSIT:

RadioElectronics. NanoSystems. Information Technologies

Journal "Radioelectronics. Nanosystems. Information Technologies" (abbr. RENSIT) publishes original articles, reviews and brief reports, not previously published, on topical problems in **radioelectronics (including biomedical) and fundamentals of information, nano- and biotechnologies and adjacent areas of physics and mathematics.**

Designed for **researchers, graduate students, physics students of senior courses and teachers.**

It turns out **4 times a year** (that includes 4 issues)

Authors of journal are academicians, corresponding members and foreign members of Russian Academy of Natural Sciences (RANS) and their colleagues,

as well as other russian and foreign authors on presentation of their manuscripts by the members of RANS, which can be obtained by authors before sending articles to editors.

And also after its receiving - on recommendation of a member of editorial board of journal, or another member of Academy of Natural Sciences, that gave her opinion on article at request of editor.

The editors will accept articles in both **Russian and English** languages.

Articles are internally peer reviewed (**double-blind peer review**) by members of the Editorial Board.

Some articles undergo external review, if necessary.

Journal RENSIT is included in the **DB SCOPUS (21.10.2017, Elsevier, Amsterdam, Netherlands), EBSCO Publishing**, in the international abstracts database - **Ulrich's International Periodicals Directory** (USA, New York, <http://www.ulrichsweb.com>), in the **AJ and DB VINITI RAS** (<http://www.viniti.ru>), and DB **Russian Science Citation Index (RSCI)** (http://elibrary.ru/project_risc.asp). Included in the **List of Higher Attestation Commission of the Ministry of Education and Science of the Russian Federation (15.01.2018, No. 757).**

Full-text content is posted in the DB of the **Russian Scientific Electronic Library**

- information resource on the Internet <http://elibrary.ru> and is available for registered users.

And also - in Open Access **CyberLeninka NEB** of Russian Federation <http://cyberleninka.ru>.

On journal's website <http://www.rensit.ru> posted metadata publications

and **RENSIT: Radioelectronics. Nanosystems. Information Technologies - english version** (cover-to-cover translation) of journal, which is a party to **CrossRef**.

The founder - the **Russian Academy of Natural Sciences**

Publisher - Publishing Center of the Russian Academy of Natural Sciences

Publisher Address: 119002 Moscow, per. Sivtsev Vrazhek 29/16

CONTENTS

RADIOELECTRONICS

THERMOELECTRIC MODEL OF A HETEROJUNCTION BIPOLAR TRANSISTOR TAKING INTO ACCOUNT THE VOLTAGE DROP ON THE CURRENT-CARRYING METALLIZATION

Vyacheslav A. Sergeev, Alexander M. Hodakov 103

MATHEMATICAL MODEL FOR SPACECRAFTS IDENTIFICATION

Igor L. Afonin, Alexander L. Polyakov, Yury N. Tyschuk, Vladislav V. Golovin, Gennady V. Slezkin 111

RADIOLOCATION

RADAR INFORMATION PROCESSING ALGORITHMS IN A SPECIALIZED COMPUTER-AIDED DESIGN SYSTEM

Maxim Yu. Konopel'kin, Sergey V. Petrov, Daria A. Smirnyagina 119

NANOSYSTEMS

PRIMARY CHEMICAL CURRENT SOURCES IN RESEARCH STUDIES OF RECENT YEARS: A REVIEW

Tatiana V. Krupina, Dmitriy S. Ermakov, Alexander O. Zhbakov, Sergey P. Gubin, Denis Yu. Kornilov 127

OBTAINING INK BASED ON PALLADIUM NANOPARTICLES FOR POSSIBLE USE IN PRINTED ELECTRONICS

Ekaterina G. Rustamova, Maria S. Kagirina, Sergey P. Gubin 143

INFORMATION TECHNOLOGIES

INFORMATION TECHNOLOGIES BASED ON NOISE-LIKE SIGNALS: II. STATISTICAL AND FRACTAL PROPERTIES OF CHAOTIC ALGORITHMS

Vadim V. Kashin, Vladimir I. Grachev, Viktor I. Ryabenkov, Vladimir V. Kolesov 151

APPLICATION OF THE INTERPOLATION METHOD OF SEQUENTIAL COMPUTATION OF THE FOURIER SPECTRUM TO SPARSE IMAGES

Alexander V. Kokoshkin, Evgeny P. Novichikhin 165

NUMERICAL RESEARCH OF THERMAL CHANGES INFLUENCE TO THE GROUND IN PERMAFROST CONDITIONS

Maxim V. Muratov, Denis S. Konov, Igor B. Petrov 175

NUMERICAL EXPLORATION OF MODELS OF GEOLOGICAL MEDIA WITH METHANE CAVITIES BY THE GRID-CHARACTERISTIC METHOD

Polina V. Stognii, Nikolay I. Khokhlov, Igor B. Petrov 181

COMPUTER SIMULATION OF UNSTEADY ELASTIC STRESS WAVES IN A CONSOLE AND A TEN-STOREY BUILDING UNDER FUNDAMENTAL INFLUENCE IN THE FORM OF A HEAVISIDE FUNCTION

Vyacheslav K. Musayev 187

HOLOGRAPHIC PROCESSING OF MOVING SOURCES IN A SHALLOW SEA WITH INTENSE INTERNAL WAVES

Venedikt M. Kuz'kin, Sergey A. Pereselkov, Elena S. Kaznacheeva, Vladimir I. Grachev, Sergey A. Tkachenko, Pavel V. Rybyanets 197

LASER PHYSICS

LONG-TERM PHOSPHORESCENCE IN COOLED ORGANIC SUBSTANCES SOLID SOLUTIONS – TEMPORAL DYNAMICS AND SPECTRAL MEMORY EFFECT

Dmitry Yu. Tsipenyuk, Alexander V. Voropinov 205



RUSSIAN ACADEMY
OF NATURAL SCIENCES

DEPARTMENT OF
RADIOELECTRONICS,
NANOPHYSICS AND
INFORMATION TECHNOLOGIES
PROBLEMS

RENSIT:
**RADIOELECTRONICS,
NANOSYSTEMS,
INFORMATION
TECHNOLOGIES.**

2022, Vol. 14, no. 2

FOUNDED IN 2009

4 ISSUES PER YEAR

MOSCOW

Editor-in-Chief

VLADIMIR I. GRACHEV

grachev@cplire.ru

Deputy Chief Editor

Vladimir A. Makarov, DrSci, MSU

Deputy Chief Editor

Sergey P. Gubin, DrSci, IGIC RAS

Executive Secretary

Rostislav V. Belyaev, PhD, IRE RAS

belyaev@cplire.ru

EDITORIAL BOARD

Anatoly V. Andreev, DrSci, MSU

Vladimir A. Bushuev, DrSci, MSU

Vladimir A. Cherепенin, DrSci, acad.RAS, IRE

Alexander S. Dmitriev, DrSci, IRE

Yuri K. Fetisov, DrSci, MIREA

Yuri V. Gulyaev, DrSci, acad.RAS, IRE

Yaroslav A. Ilyushin, DrSci, MSU

Anatoly V. Kozar, DrSci, MSU

Vladimir V. Kolesov, PhD, IRE

Albina A. Kornilova, PhD, MSU

Alexander V. Okotrub, DrSci, SB RAS

Aleksey P. Oreshko, DrSci, MSU

Igor B. Petrov, DrSci, c-m RAS, MIPT

Alexander A. Potapov, DrSci, IRE

Vyacheslav S. Rusakov, DrSci, MSU

Alexander S. Sigov, DrSci, acad.RAS, MIREA

Valentine M. Silonov, DrSci, MSU

Eugeny S. Soldatov, DrSci, MSU

Ikhsamsuren Enkhtor, DrSci (Mongolia)

Yoshiyuki Kawazoe, DrSci (Japan)

Kayrat K. Kadyrzhanov, DrSci (Kazakhstan)

Peter Paul Mac Kenn, DrSci (USA)

Jiao Licheng, Ph.D. (China)

Deleg Sangaa, DrSci (Mongolia)

Andre Skirtach, DrSci (Belgium)

Enrico Verona, DrSci (Italy)

ISSN 2414-1267

The journal on-line is registered by the Ministry of Telecom and Mass Communications of the Russian Federation. Certificate EL. no. FS77-60275 on 19.12.2014

All rights reserved. No part of this publication may be reproduced in any form or by any means without permission in writing from the publisher.

©RANS 2022

EDITORIAL BOARD ADDRESS

218-219 of, 7 b., 11, Mokhovaya str.,

125009 MOSCOW, RUSSIAN FEDERATION,

TEL. +7 495 629 3368

FAX +7 495 629 3678 FOR GRACHEV

DOI: 10.17725/rensit.2022.14.103

Thermoelectric model of a heterojunction bipolar transistor taking into account the voltage drop on the current-carrying metallization

^{1,2}Vyacheslav A. Sergeev, ¹Alexander M. Hodakov

¹Kotelnikov Institute of Radioengineering and Electronics of RAS, Ulyanovsk Branch, <http://www.ulireran.ru/>

Ulyanovsk 432071, Russian Federation

²Ulyanovsk State Technical University, <https://www.ulstu.ru/>

Ulyanovsk 432027, Russian Federation

E-mail: sva@ulstu.ru, hod22am@mail.ru

Received May 18, 2022, peer-reviewed May 25, 2022, accepted May 31, 2022

Abstract: A 3D thermoelectric model has been developed to calculate the temperature field in the comb structure of a heterojunction bipolar transistor formed on the surface of a rectangular semiconductor crystal with the length of the emitter metallization paths comparable to the size of the crystal, taking into account the inhomogeneous distribution of current density under the emitter paths due to voltage drop on the resistance of current-carrying metallization. The model is based on the solution of the thermal conductivity equation together with a system of equations for the distribution of the potential for metallization of the emitter track and the current density under the track in the COMSOL Multiphysics software environment. It is shown that as a result of the combined effect of the voltage drop on the resistances of the emitter tracks, the inhomogeneity of the temperature field in a crystal with limited dimensions and the strong dependence of the emitter current density on temperature, the temperature and current density distributions along the emitter tracks change character: from monotonously and weakly decreasing from the beginning of the track to the end in the isothermal approximation, these distributions become non-monotonic and significantly heterogeneous. At the same time, the maximum current density and temperature with an increase in the operating current shifts from the beginning to the center of the tracks. It has also been found that with the crystal sizes unchanged, an increase in the length of the tracks leads to a certain decrease in the coefficient of inhomogeneity of the temperature distribution.

Keywords: heterojunction bipolar transistor, current density, temperature, inhomogeneity

UDC 621.382.029

Acknowledgments: The work was carried out within the framework of the state assignment and supported by the Russian Science Foundation (project No. 22-29-01134).

For citation: Vyacheslav A. Sergeev, Alexander M. Hodakov. Thermoelectric model of a heterojunction bipolar transistor taking into account the voltage drop on the current-carrying metallization. *RENSIT: Radioelectronics. Nanosystems. Information technologies*, 2022, 14(2):103-110e. DOI: 10.17725/rensit.2022.14.103.

CONTENTS

1. INTRODUCTION (104)

2. THERMOELECTRIC MODEL (106)

3. RESULTS AND DISCUSSION (107)

4. CONCLUSION (108)

REFERENCES (109)

1. INTRODUCTION

Along with the active development of MOSFET and HEMT microwave transistors, powerful bipolar (BT), including heterojunction (HBT), microwave transistors are widely used in modern radio and telecommunications equipment [1-4]. Devices of this class are the least reliable in the composition of modern radio-electronic systems for various purposes, since they operate in the most severe thermal and electrical modes. This class of devices is characterized by the presence of strong positive thermal feedback and the manifestation of the effects of inhomogeneous and unstable distribution of current density, power and temperature in transistor structures [5-7], which lead to local overheating and thermomechanical stresses of the structure and, as a consequence, to acceleration of degradation mechanisms and failures of devices.

One of the most common geometries of the structures of modern high-power BT and HBT is a strip or comb geometry with a parallel arrangement of elementary transistors (cells) HBT (see **Fig. 1** [4] and **Fig. 2** [7]). Self-heating of each HBT cell by dissipated power and thermal coupling between neighboring cells lead to an uneven temperature profile of the matrix of HBT elementary transistors. Due to the positive temperature coefficient of the emitter current, currents of higher density will flow through the central HBT cells with a higher temperature,

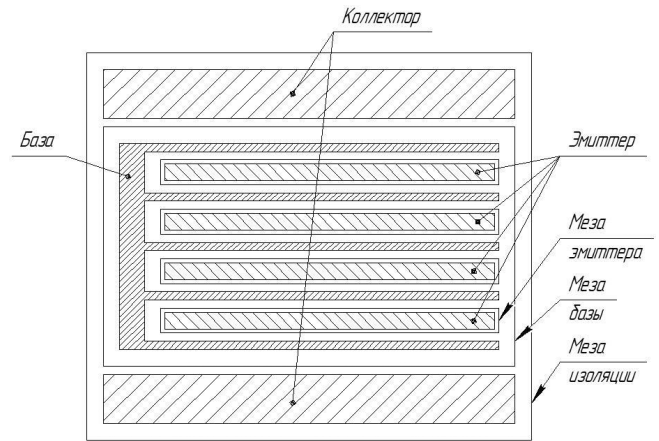


Fig. 1. Topology of the active region of HBT [4].

which leads to an increase in heat generation, which ultimately can lead to thermal breakdown or degradation of the device [8, 9], which is especially pronounced at high injection levels [10].

To reduce the nonuniform temperature distribution and solve these thermal problems, various variants of one-dimensional geometry design are used, including changing the length of the emitter in the HBT cells [7] and changing the distance between

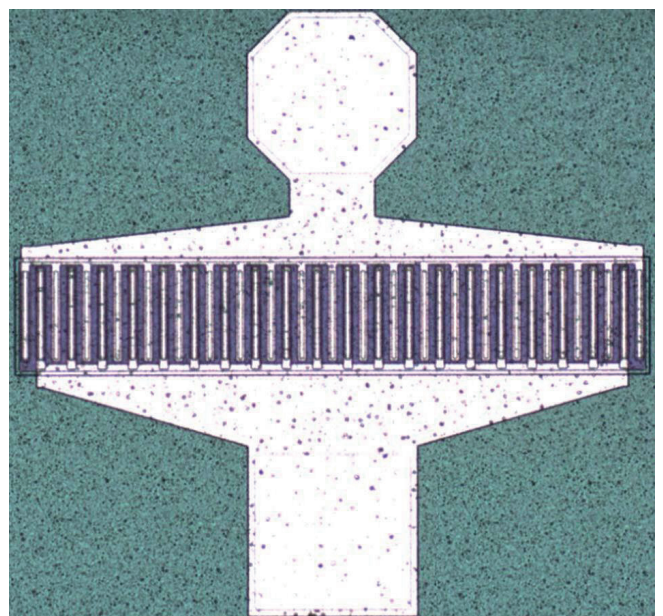


Fig. 2. Comb structure of a HBT with 20 elementary transistors [7].

the emitters between the HBT cells [8], which reduces the temperature difference along the direction of the emitter width.

However, the thermoelectric processes in the comb structures of HBT in the known works are considered without taking into account the voltage drop on the current-carrying paths of emitter metallization, which leads to a significant inhomogeneous distribution of the emitter current density, and hence the power dissipation density along the emitter paths [11-13].

This article presents a 3D thermoelectric model for calculating the temperature field in the comb structure of the HBT, taking into account the combined influence of all the factors listed above of the inhomogeneous distribution of current and temperature in the instrument structure, including the inhomogeneous distribution of current density under the emitter tracks as a result of voltage drop on the resistance of current-carrying metallization.

2. THERMOELECTRIC MODEL

To determine the temperature field in the semiconductor structure of the HBT, a 3D thermoelectric model was constructed, the scheme of which is shown in Fig. 3. The design of the transistor structure is a rectangular semiconductor crystal with dimensions $l_x \times l_y \times l_z$ and 4 emitter metallization tracks of size $a_e \times L_e \times h_e$ each located on its upper surface.

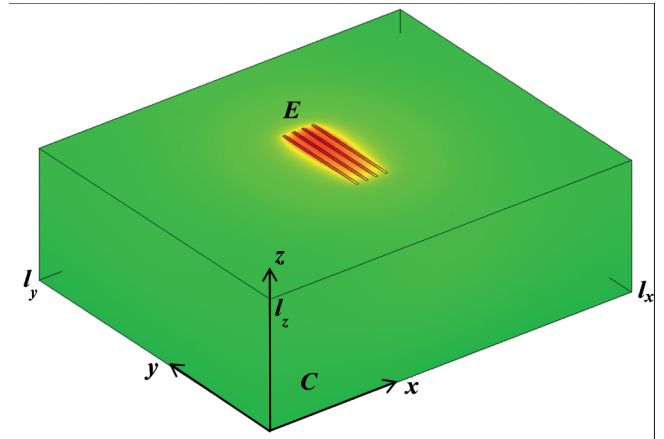


Fig. 3. Scheme of the HBT structure model: E is emitter, C is a semiconductor crystal.

The temperature distribution over the HBT structure is found from the solution of the stationary equation of thermal conductivity

$$\nabla_{x,y,z} (\lambda(T) \nabla_{x,y,z} T(x, y, z)) = 0, \tag{1}$$

where λ is the thermal conductivity coefficient of the crystal.

Boundary conditions of the thermal conductivity problem: the side surfaces and the upper surface of the crystal are thermally insulated; the temperature of the lower surface of the crystal is equal to the temperature of the heat sink T_0 ; the power density is set on the upper surface in the emitter region of the structure:

$$-\lambda(T) \frac{\partial T}{\partial z} \Big|_{z=l_z} = \begin{cases} J_e(x, y) U_c, & (x, y) \in S_e, \\ 0, & (x, y) \in S - S_e, \end{cases} \tag{2}$$

where $S, S_e = n a_e L_e$ are the area of the upper surface of the crystal and its active region, n is number of emitter tracks, J_e, U_c are emitter current density and collector voltage.

To find the current density along the emitter path, we write down the following

system of equations. According to the voltage-ampere characteristics of the transistor

$$J_e(x, y) = J_{e0} (T(x, y) / T_0)^3 \times \exp \left\{ \frac{-E_g + e(U_e - \varphi_e(x, y) - rS_e n^{-1} J_e(x, y))}{kT(x, y)} \right\}, \quad (3)$$

where J_{e0} is weakly temperature-dependent parameter, U_e is direct voltage drop at the emitter p - n junction, E_g is band gap width of a semiconductor, e is electron charge, φ_e is emitter metallization potential, r is input ohmic resistance of the transistor, k is Boltzmann constant.

As a condition for the inclusion of a transistor in an electrical circuit, we will consider the condition of constancy of the total emitter current I_e . This means that for any temperature distribution $T(x, y, l_z)$ over the active region of the semiconductor structure, a restrictive equality must be fulfilled:

$$\iint_{S_e} J_e(x, y, l_z) dx dy = I_e. \quad (4)$$

Let's limit ourselves to an approximation, assuming the emitter tracks are narrow, that is, we neglect the effect of pushing the emitter current to the lateral edges of the tracks along the coordinate x . Then the equations for the distribution of the potential φ_e and current density J_{em} over the metallization of the emitter track will be written as:

$$\frac{dJ_{em}(y)}{dy} = -\frac{J_e(y)}{h_e}, \quad (5)$$

$$\frac{d\varphi_e(y)}{dy} = -\frac{J_{em}(y)}{\sigma_{em}}, \quad (6)$$

with boundary conditions:

$$J_{em}(0) = I_e / h_e a_e, \quad (7)$$

$$J_{em}(L_e) = 0, \quad (8)$$

$$\left. \frac{d\varphi_e}{dy} \right|_{y=y_{eb}} = -\frac{I_e}{\sigma_{em} h_e a_e}, \quad (9)$$

$$\left. \frac{d\varphi_e}{dy} \right|_{y=y_{ee}} = 0, \quad (10)$$

where y_{cb} and y_{ce} are coordinates of the beginning and end of the track, σ_{em} is the specific conductivity of the metallization of the emitter track.

The solution of the model problem (1) – (10) was found by the numerical iterative method, the algorithm of which is presented in [14]. The developed program included an appeal to the COMSOL Multiphysics interactive software environment. InGaP/GaAs HBT [4] with a crystal size of $300 \times 250 \times 100$ microns was chosen as the calculated base object of the study. The active cell of the transistor has a comb structure with 4 emitter tracks, the dimensions of which were: width $a_e = 2 \mu\text{m}$, thickness $h_e = 0.5 \mu\text{m}$, and the length varied within $L_e = (40 \div 80) \mu\text{m}$. The track material is gold. The temperature dependence of the thermal conductivity coefficient of the transistor crystal material $\lambda(T)$ was selected from the COMSOL program

database. Heat sink temperature $T_0 = 300$ K.

As an initial approximation of the dependence $J_e^0(y)$ in the iterative process, the current density values calculated by the formula [11] were chosen:

$$J_e^0(y) = \frac{2\phi_{T_0}}{L_e a_e R_e} \cdot \frac{C^2}{\cos^2[C(1-y/L_e)]}, \quad (11)$$

where ϕ_{T_0} is temperature potential at $T_0 = 300$ K, the value of which is equal to 26 mV; R_e is the metallization resistance of the emitter track, and the constant C is found from the solution of the equation $C \operatorname{tg} C = R_e I_e / 2n\phi_{T_0}$.

3. RESULTS AND DISCUSSION

Further results of numerical calculations are presented for a variant of the transistor operation mode at $I_c = 40$ mA, $U_c = 7$ V. Initial value $U_e = 1.2$ V.

Fig. 4 shows the results of modeling the distribution of emitter current density and temperature under the 3rd emitter track.

As can be seen, the temperature-dependent approximation of the emitter current density (formula 3) has a significant effect on the heterogeneity of the emitter current density and temperature distributions along the track.

Calculations have shown that the maximum value of the potential, if the length of the emitter track changes within the above limits, varies from 10.3 to 23.0 mV (less than the value ϕ_{T_0}), and the heterogeneity of the potential distribution increases with growth (**Fig. 5**).

Coefficient of heterogeneity of temperature distribution η_T , where $\eta_T = \frac{T_{max} - T_{min}}{T_{avg}}$, are

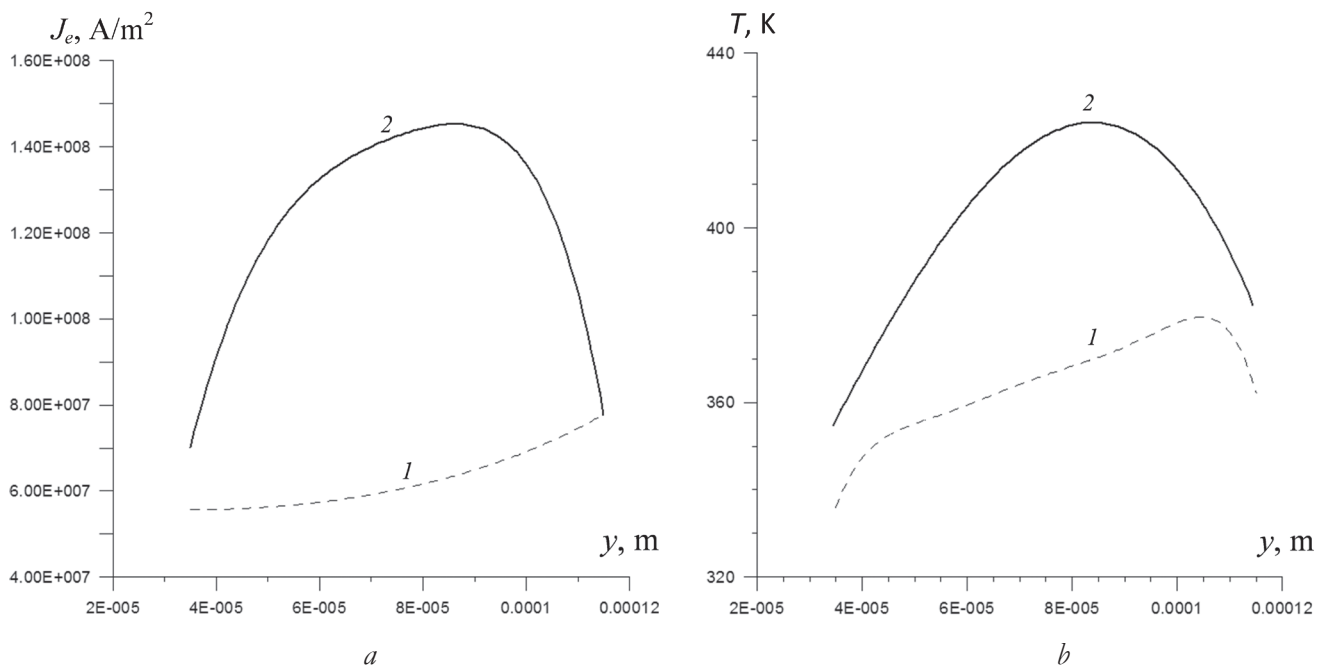


Fig. 4. Distribution of current density (a) and temperature (b) under the 3rd emitter track; $I_c = 40$ mA, $U_c = 5$ V; $a_e = 2 \mu\text{m}$, $h_e = 0.5 \mu\text{m}$, $L_e = 80 \mu\text{m}$; approximation: 1 – formula 11, 2 – temperature-dependent, formula 3.

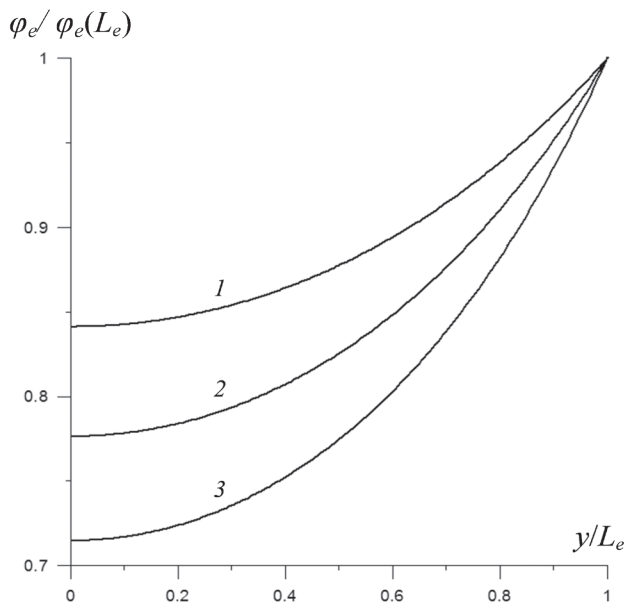


Fig. 5. Distribution of the reduced potential along the emitter path; $I_e = 40 \text{ mA}$, $U_c = 5 \text{ V}$; $a_e = 2 \text{ }\mu\text{m}$, $b_e = 0.5 \text{ }\mu\text{m}$, L_e : 1 –40, 2 –60, 3 –80 μm .

the maximum and average temperature increment, respectively, decreases with an increase in the length of the track by 1.3 times (**Fig. 6**).

4. CONCLUSION

Thus, the proposed thermoelectric model of the HBT comb structure, taking into account the inhomogeneous distribution of emitter current density as a result of voltage drop on the metallization emitter tracks and positive thermoelectric feedback acting in the HBT semiconductor structure, showed that the temperature and current density distributions along the emitter tracks change character: from monotonously and weakly decreasing from the beginning of the track to finally, in the isothermal approximation, these distributions become nonmonotonic and substantially inhomogeneous.

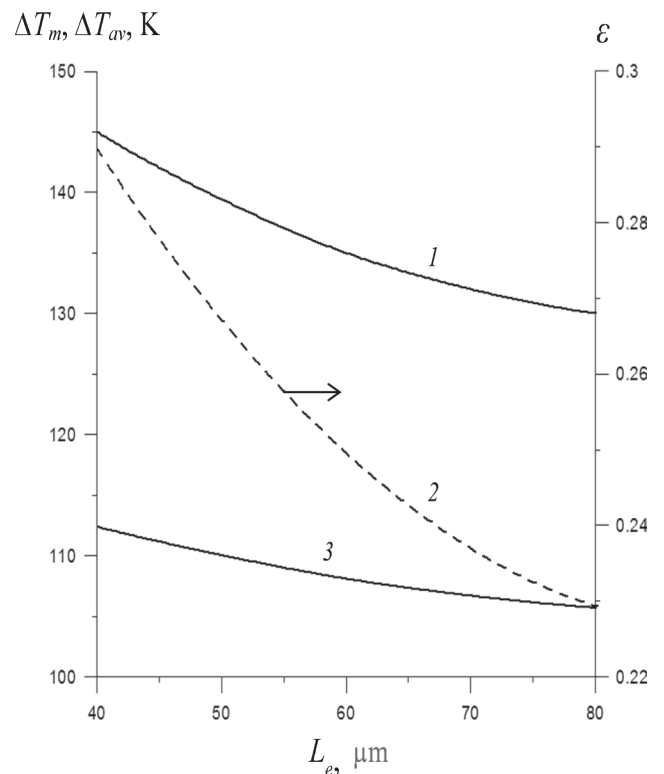


Fig. 6. Dependence of the maximum (1), average (3) temperature increment and inhomogeneity coefficient (2) on the track length; $I_e = 40 \text{ mA}$, $U_c = 5 \text{ V}$; $a_e = 2 \text{ }\mu\text{m}$, $b_e = 0.5 \text{ }\mu\text{m}$.

An increase in the heterogeneity of temperature and current density in the HBT structure leads to a decrease in the maximum functionality of the device in current and power. At the same time, the maximum current density and temperature with increasing operating current shifts from the beginning to the center of the tracks. It has also been found that with the crystal sizes unchanged, an increase in the length of the tracks leads to a certain decrease in the coefficient of inhomogeneity of the temperature distribution.

The proposed model can be used in the development of HBT structures and the

assessment of their limiting functionality in terms of current and temperature.

REFERENCES

1. Jianjun Gao. *Heterojunction Bipolar Transistors for Circuit Design : Microwave Modeling and Parameter Extraction*. United States, John Wiley & Sons Inc, 2015, 280 p.
2. Xin Wen, Akshay Arabhavi, Wei Quan. Performance Prediction of InP/GaAsSb Double Heterojunction Bipolar Transistors for THz applications. *J. Appl. Phys.*, 2021, 130:034502.
3. Lachner R. Industrialization of mmWave SiGe technologies: Status, future requirements and challenges. *IEEE 13th Topical Meeting on Silicon Monolithic Integrated Circuits in RF Systems*, 2013, p. 105-107.
4. Kozlovskij EYu, Zaharov SI, Semenova LM, Tejder AA. Razrabotka tekhnologii izgotovleniya geterobipolyarnyh tranzistorov na osnove struktur InGaP/GaAs. *Sb. trudov 31-oj Mezhdunarodnoj konferencii "SVCH-tekhnika i telekommunikacionnye tekhnologj"*, 2021, Vyp. 3, s. 27-29 (in Russ.).
5. Lee CP, Chau FHF, Ma W, Wang NL. The Safe Operating Area of GaAs-Based Heterojunction Bipolar Transistor. *IEEE Trans. Electron.*, 2006, 53(11):2681-2688.
6. Chen Liang. Thermal stability improvement of a multiple finger power SiGe heterojunction bipolar transistor under different power dissipations using non-uniform finger spacing. *Chinese Physics B*, 2011, 20:018501.
7. Jin Dongyue. Thermal stability of the power SiGe HBT with non-uniform finger length. *Proc. International Conference on Microwave and Millimeter Wave Technology*, 2008, p. 166-169.
8. Dongyue Jin, Wanrong Zhang, Hongyun Xie, Liang Chen, Pei Shen, Ning Hu. Structure optimization of multi-finger power SiGe HBTs for thermal stability improvement. *Microelectronics Reliability*, 2009, 49(4):382-386.
9. Rui Chen. Thermal resistance matrix representation of thermal effects and thermal design in microwave power HBTs with two-dimensional array layout. *Chinese Phys. B*, 2019. DOI: 10.1088/1674-1056.ab3436.
10. Lu Z, Zhou L, X. Hu X. Electro-Thermal analysis of SiGe HBT under HPM Injection. *Proc. IEEE MTT-S International Conference on Numerical Electromagnetic and Multiphysics Modeling and Optimization (NEMO)*, 2020, p. 1-4.
11. Caves KY, Barnes IA. Optimum length of emitter stripes in "comb" structure transistors. *IEEE Trans.*, 1965, ED-12(2):84-85.
12. Sergeev VA. Izotermicheskoe tokoraspredelenie v grebenchatyh strukturah moshchnyh VCH i SVCH bipolyarnyh tranzistorov. *Izvestiya*

- Samarskogo nauchnogo centra RAN*,
2005, 2:344-351 (in Russ.).
13. Sergeev VA. Analiticheskaya model
neizotermicheskogo raspredeleniya
plotnosti moshchnosti v strukturah
bipolyarnykh tranzistorov. *Izvestiya
vuzov. Elektronika*, 2005, 3:22-28. (in
Russ.).
14. Sergeev VA, Hodakov
AM. *Nelinejnye teplovye modeli
poluprovodnikovyyh priborov*. Ul'yanovsk,
UIGTU Publ., 2012, 159 s.

DOI: 10.17725/rensit.2022.14.111

Mathematical model for spacecrafts identification

Igor L. Afonin, Alexander L. Polyakov, Yury N. Tyschuk, Vladislav V. Golovin, Gennady V. Slezkin

Sevastopol State University, <http://www.sevsu.ru/>
Sevastopol 299053, Russian Federation

E-mail: ilafonin@sevsu.ru, alpolyakov@sevsu.ru, yntyschuk@sevsu.ru, vvgolovin@sevsu.ru, gvslszkin@sevsu.ru

Received February 08, 2022, peer-reviewed February 15, 2022, accepted February 22, 2022

Abstract: Proposed below is a mathematical model for reception and processing of spurious (“uncontrolled” radiation) from constantly operating units of the special complex installed onboard a spacecraft. This model makes it possible to implement a new technique for identification of such radiation thus improving the capabilities of the space monitoring. At the same time creation of stand-alone radio systems solely for identification of the spacecrafts based on the proposed mathematic model would require significant expenses therefore it is worthwhile to add new identification hardware to the existing ground-based radio systems used for space flight control. Identifying features in the proposed mathematical model are the parameters of signals of the uncontrolled radiation from constantly operating units installed onboard spacecrafts that “leak” through antenna systems (master generators, heterodyne oscillators in the spacecraft radio receivers). Identification of spacecrafts by uncontrolled radiation from the receiving master generators and heterodyne oscillators involves keeping track of the behavior of oscillation parameters as well as identifying signs that distinguish the oscillations of one generator from another. Since the uncontrolled radiation from heterodyne oscillators is a harmonic oscillation, it features such parameters as amplitude, frequency and initial phase. It is impossible to use the amplitude and initial phase of the signal for identification purposes because the propagation medium strongly affects these parameters. The most informative for identification purposes is the frequency of oscillations, or rather, the behavior of the frequency changes over time. These changes are due to the frequency instability of the onboard master generators. The behavior of the frequency change depends on the characteristics of each onboard generator, which serves as a basis for identification. It should be noted that the identification process can be conditionally divided into two stages: the first stage includes validation of models and processing (evaluation) algorithms while the second stage involves classification of the results of processing (evaluation).

Keywords: identification, spacecraft, radio engineering system, space control, uncontrolled radiation, effective antenna area

UDC 629.7.086

For citation: Igor L. Afonin, Alexander L. Polyakov, Yury N. Tyschuk, Vladislav V. Golovin, Gennady V. Slezkin. Mathematical model for spacecrafts identification. *RENSIT: Radioelectronics. Nanosystems. Information technologies*, 2022, 14(2):111-118e. DOI: 10.17725/rensit.2022.14.111.

CONTENTS

1. INTRODUCTION (112)
2. MAIN PART (112)

3. CONCLUSION (117)

REFERENCES (117)

1. INTRODUCTION

For many space systems it is typical to have onboard transmitting devices of the spacecraft disconnected when outside the visibility range of its radio systems. This fact significantly complicates identification of maneuvering spacecrafts.

Based on the above fact, we found it worthwhile to develop such an identification technique that would eventually improve operational quality of a space monitoring system.

In doing so, for the identification parameters we decided to use signals associated with spurious “uncontrolled” radiation (UCR) coming from constantly operating units of the onboard equipment (i.e. heterodyne oscillators, master generators).

The proposed identification technique is based on the algorithm for evaluating parameters of the correlated component of the instability process of master generators installed onboard the spacecraft, with the process itself regarded as an identifying factor [1].

2. MAIN PART

To solve the problem in question we evaluated the feasibility of reception and processing of spurious signals radiated from certain radio systems (RS) of a ground-based complex. Results of such evaluation showed that antenna arrangements of these systems could be used for SC identification purposes as well [4].

The only signal received from an “enclosed” SC could be an UCR from onboard receiver’s heterodyne oscillators and master generators. Sources of frequency instability in the onboard RS can be conditionally classified by the following criteria [1,9]:

Systematic changes of frequency caused by drifts. These changes are due to aging of

the resonator material and are extremely slow. They are also called “long-term” instability and they are measured in frequency change per hour, day, month or year depending on the device type and application specifics.

Deterministic periodic frequency deviations caused by incidental frequency modulation from surrounding processes, such as instability of power supplies, crosstalks, temperature variations, vibrations, pressure etc.

Frequency deviations triggered by random fluctuations due to the use of electronic components in the devices. Such frequency fluctuations are called “short-term” instability.

Instability will include three main components. The first one is a slowly varying component $g(t)$ (dashed line in **Fig. 1**) that describes non-stationarity of the process and can be considered as a deterministic component (at least throughout a certain sampling period).

This component is described by a polynomial

$$g(t) = C_0 + c_1 t + c_2 t^2 + \dots$$

The second component $m(k)$ accounts for slowly changing fluctuations $\varphi(k)$ relative to component $g(k)$. This component can be considered random local stationary process with long correlation time. In this case

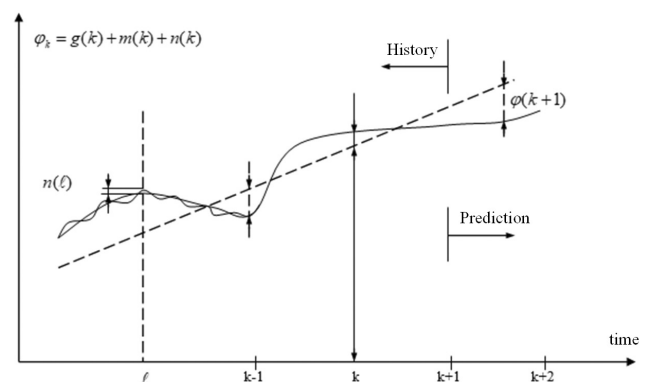


Fig. 1. Illustration of frequency instability process components.

when $g(k) = g_0 = \text{const}$, it is also subject to prediction.

The third component $n(k)$ represents fast frequency fluctuations that are stationary throughout the sampling period but have low correlation time. Therefore, the instability process due to phase drifts will be as follows

$$\varphi(t) = g(t) + m(t) + n(t). \tag{1}$$

However, some peculiarities of the process components (1) require development of special algorithms for their analysis.

Component $g(t)$ of the process (1) features relatively slow changes within the observation time interval. Therefore, it is worthwhile to regard it as constant within this interval and exclude from the analysis of the instability models.

Component $m(t)$ of the process (1) is a locally stationary process with a relatively long correlation time. To determine its parameters, we find it appropriate to use the least squares method [4,5] or dynamic filtration method [6,7]. In order to lower computation time and increase speed we deem necessary to use their recurrent modifications with relatively small portion of the gathered information being involved in the processing.

Component $n(t)$ of the process (1) describes rapid phase fluctuations over time which are the most informative in terms of detecting peculiarities of master generators. $n(t)$ is more informative than $m(t)$ because component $m(t)$ has constituents of unknown Doppler frequency shift. Presence of the Doppler shift often make it impossible to ensure identification by component $m(t)$.

We will analyze component $m(t)$ of the phase shift process $\varphi(t)$ (1) by using a model as defined by state and watch equations

$$\begin{cases} \dot{x}(t) = Fx(t) + Gg(t), \\ m(t) = Hx(t), \end{cases} \tag{2}$$

$$\begin{cases} z(t) = H_1m(t) + n(t), \\ z(t) = \varphi(t) - g(t), \end{cases} \tag{3}$$

while taking into account that process $n(t)$ is regarded as the white noise because its correlation time is considerably lower than correlation time of component $m(t)$. This model is used for making a modification to the dynamic filtration algorithm.

Additionally, evaluation of the model parameters of component $m(t)$ for the least squares method was considered

$$Z(t) = \mathcal{A}M(t) + n(t), \tag{4}$$

where \mathcal{A} is a constraint matrix; $M(t)$ is a vector of the linear model parameters that are being evaluated using the least squares method (LSM); $n(t)$ is a component in (1), $z(t) = \varphi(t) - q(t) = m(t) + n(t)$.

The experience in research of stationary quickly fluctuating processes similar to $n(t)$ shows that they can be highly effectively described by autoregressive models [2,3,6]. Therefore, further description and analysis of component $n(t)$ was done in terms of autoregressive models:

$$\begin{cases} y(t) = \sum_{i=1}^n a_i y(t-i) + e_1(t), \\ n(t) = e_1(t) + e_2(t), \end{cases} \tag{5}$$

where a_i are coefficients of an autoregressive model; $e_1(t)$ is a generating noise, $e_1(t) = \sum_{i=1}^n a_i n(t-i) + e_1(t-i)$, $e_2(t)$ is a white noise of measurements, $e_2(t) = e_1(t) - \sum_{i=1}^n a_i e_2(t-i)$, $y(t)$ is a process of oscillation phase change caused by poorly correlated component of the instability; $n(t)$ is a component of process $\varphi(t)$ (2).

We will develop equations that describe algorithms for evaluation of components (1) $m(t)$ and $n(t)$ for models (2)-(5).

Taking into account the peculiarities of the instability model (1), we will analyze the feasibility of developing a recurrent algorithm of LSM using a “sliding” window. To do so

we will first investigate a linear model of component $m(t)$ of the phase change process $\varphi(t)$ (1), presented as follows

$$Z(t) = AH + n(t)$$

with a measurement vector, where z_1, \dots, z_N are measurements of the signal phase at moments t_1, \dots, t_N , matrix $A = [A_1^T, \dots, A_n^T]$, where $A_i^T = [a_i, \dots, a_r]$ is i -th row of matrix A , vector of parameters in question $M = [M_1, \dots, M_r]^T$, and vector of random measurement errors $[n_1, \dots, n_n]^T$, where n_1, \dots, n_n is a value of component $n(t)$ at time moment t_1, \dots, t_n . Evaluation using the least squares method $\hat{M}(n, n+1)$ can be made based on measurements $z_{n+1}, \dots, z_{n+\ell}$ while using matrix rows from $(n+1)$ to $(n+\ell)$.

As a result, expressions were developed to determine transfer coefficients when a new measurement is selected

$$K^{(1)}(n, n+\ell) = \sum_{n=1}^T (n, n+\ell) A_{n+\ell+1} \times \left[J + A_{n+\ell+1}^T \sum_{n=1}^T (n, n+\ell) A_{n+\ell+1} \right]^{-1}, \quad (6)$$

$$\sum_{n=1}^T (n, n+\ell+1) = (J - K^{(1)}(n, n+\ell) A_{n+\ell+1}^T) \sum_{n=1}^T (n, n+\ell), \quad (7)$$

where ℓ is a unity matrix, or in detail as follows

$$\begin{aligned} \sum_{n=1}^T (n, n+\ell+1) &= \sum_{n=1}^T (n, n+\ell) - \sum_{n=1}^T (n, n+\ell) A_{n+\ell+1} \times \\ &\times \left(A_{n+\ell+1}^T \sum_{n=1}^T (n, n+\ell) A_{n+\ell+1} + 1 \right)^{-1} \times \\ &\times A_{n+\ell+1}^T \sum_{n=1}^T (n, n+\ell), \end{aligned} \quad (8)$$

and when forgetting the outdated information

$$K^{(2)}(n, n+\ell+1) = \sum_{n=1}^T (n, n+\ell+1) \times A_{n+1} \left[J - A_{n+1}^T \sum_{n=1}^T (n, n+\ell+1) A_{n+1}^T \right], \quad (9)$$

$$\begin{aligned} \sum_{n=1}^T (n+1, n+\ell+1) &= (J + K^{(2)}(n, n+\ell+1) A_{n+1}^T) \times \\ &\times \sum_{n=1}^T (n, n+\ell+1). \end{aligned} \quad (10)$$

or in detail as follows

$$\begin{aligned} \sum_{n=1}^T (n+1, n+\ell+1) &= \sum_{n=1}^T (n, n+\ell+1) + \\ &+ \sum_{n=1}^T (n, n+\ell+1) \times \\ &\times A_{n+1} \left[J - A_{n+1}^T (n, n+\ell+1) A_{n+1} \right]^{-1} \times \\ &\times A_{n+1}^T \sum_{n=1}^T (n, n+\ell+1). \end{aligned} \quad (11)$$

Vectors $K^{(1)}$ and $K^{(2)}$ having length of $r+1$ are called transfer coefficients when introducing a new measurement and when forgetting, respectively. Another more PC-friendly presentation of the transfer coefficient $K^{(1)}$ [7] can be used

$$K^{(1)}(n, n+\ell) = \sum_{n=1}^T (n, n+\ell+1) A_{n+\ell+1} \quad (12)$$

and $K^{(2)}$ coefficient

$$K^{(2)}(n, n+\ell+1) = \sum_{n=1}^T (n+1, n+\ell+1) A_{n+1}. \quad (13)$$

Furthermore, by doing a block-by-block multiplication of matrix $A^T(n, n+\ell+1)$ and vector $z(n, n+\ell+1)$, we find that

$$\begin{aligned} A^T(n+1, n+\ell+1) z(n+1, n+\ell+1) &= \\ = A(n, n+\ell+1) z(n, n+\ell+1) - A_{n-1} z_{n+1}. \end{aligned} \quad (14)$$

So, using recurrent procedure of the LSM over the sliding window makes it possible to establish a relatively simple procedure for evaluation of $m(t)$ component parameters of process $\varphi(t)$ (1). This procedure will be used for processing the measurement results of UCR signal phase.

For complete research and synthesis of an optimum algorithm for identification of SC UCR, we performed an analysis of the evaluation procedure by using a linear Kalman filter with a finite memory of component $m(t)$ of process $\varphi(t)$ (1) as an alternative to modification of LSM (7)-(14).

To do so, we analyzed a dynamic system with discrete time being analogous to (2), (3) and described by equations of state

$$\begin{aligned} x(k+1) &= \Phi(k+1, k)x(k) + G(k+1)\xi(k+1), \\ m(k+1) &= Hx(k+1) \end{aligned} \tag{15}$$

and equations of observation

$$\begin{aligned} z(k) &= H_1 m(k) + n(k), \\ z(k) &= \varphi(k) - q(k) = m(k) + n(k), \end{aligned} \tag{16}$$

where $\Phi(k+1, k)$ is a transfer matrix; k is a variable denoting filtration iteration index.

Practical implementation of this identification method was carried out in the following order. Preliminary frequency search is done using a Fourier-transform processor within 50 kHz band based on a sequential scanning method for a given frequency band. After detection of a signal and estimating frequency with an accuracy of 25 kHz, the signal is then directed to the digital spectrograph that uses the same Fourier-transform processor. Data from the analyzer output are then transmitted to a minicomputer for further processing.

Sequence of subsequent operations performed on the received signal is shown as a block diagram in **Fig. 2**.

Detected signal with phase change pattern denoted as $\varphi(t)$ is then directed to a device that subtracts long-term instability component $g(t)$ from $\varphi(t)$. It should be noted that this procedure is performed by using a method that involves finding mean value over the observation interval with

subsequent calculation of the result from each measurement.

In accordance with model (1), calculation of $g(t)$ from $\varphi(t)$ results in the fact that now we need to process a sum of two components of process $\varphi(t)$: $m(t)$ and $n(t)$ (see Fig. 2). Component $m(t)$ is a slowly varying component due to both instability of a generator and unknown Doppler frequency component. Since the Doppler component is unknown, component $m(t)$ of process $\varphi(t)$ cannot be used for SC identification. Therefore, we deem necessary to evaluate parameters of model $m(t)$, and estimate its state vector and then exclude $m(t)$ from further analysis.

To accomplish this purpose we use a procedure for linear optimal filtration and recurrent LSM with a sliding window.

Selection of a finite memory procedure is impeded by not having accurate information about the order of model $m(t)$. It was believed that presence of sliding windows would slightly alleviate this problem.

Evaluation results for component $m(t)$ are subtracted from sum $m(t) + n(t)$ (see Fig. 2) and further processing is performed on the fast-changing component $n(t)$. This component is governed by the peculiarities of a master generator. Its values are then fed into a device that implements time-series analysis procedure. The device outputs

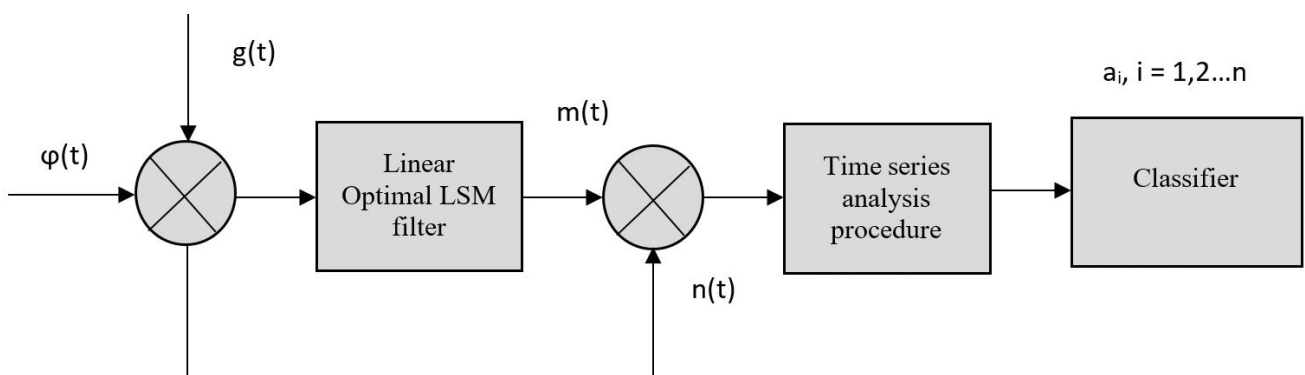


Fig. 2. Sequence of operations performed on the received signal during SC identification.

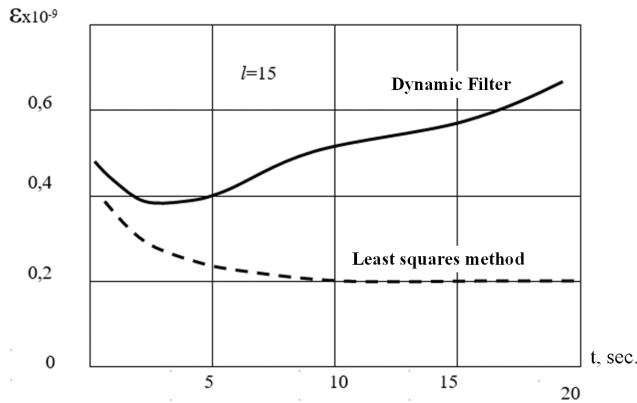


Fig. 3. Algorithm comparison results for “sliding window” with $l = 15$.

estimations of a_1 parameters of process $n(t)$. Values of these parameters are then directed to a classifier where a decision is made about a type and identity of the detected SC.

Fig. 3 and 4 for an observation time of 20 sec. show results of comparison between evaluation algorithms based on the least squares method and dynamic filtration method. Y-axes show mean values $\epsilon(t)$ that are determined as sum of squared differences between measurement results $f(t_i)$ at moments t_i and evaluations of process $\hat{m}(t_i)$ as divided by number i .

$$\epsilon(t) = \frac{1}{i} \sum_{k=1}^i [f(t_i) - \hat{m}(t_i)]^2, \quad i \sim 1, \dots, N,$$

where N is the number of measurements. Parameter i determines the size of the “sliding” window.

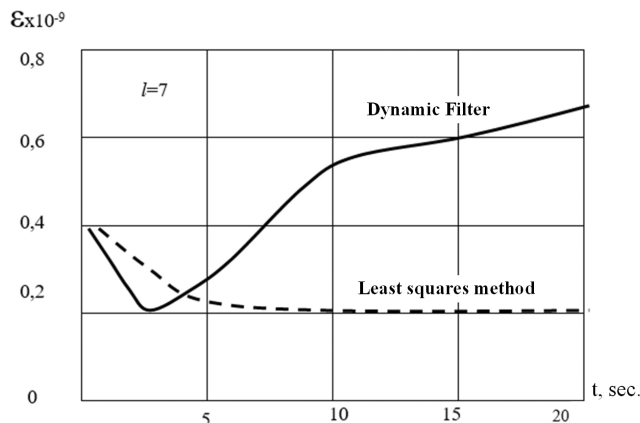


Fig. 4. Algorithm comparison results for “sliding window” with $l = 7$.

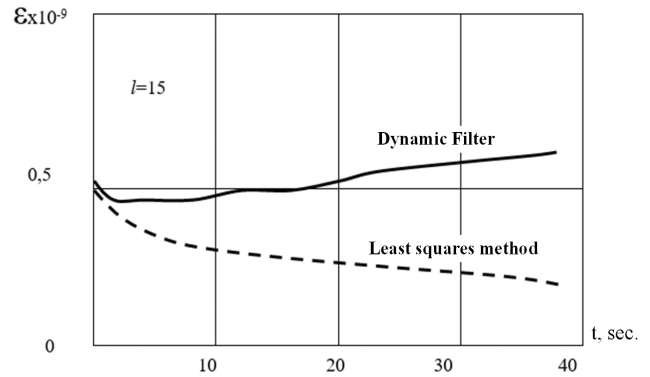


Fig. 5. Algorithm comparison results for “sliding window” with $l = 15$.

Analysis of curves (see Fig. 3 and 4) shows that dynamic filtration algorithm turns out to be unstable under conditions of high prior uncertainty about parameters of the process being filtered. Increasing window size to 15 makes it possible to slightly improve evaluation results obtained using the dynamic filtration algorithm as shown in Fig. 5 for an observation interval of 40 sec.

However, further increasing window size l again results in increased ϵ , which is most likely due to some inconformity of the model with the process (Fig. 6)

Unlike the dynamic filter, recurrent LSM procedure over the sliding window turns out to be more stable and yields appropriate

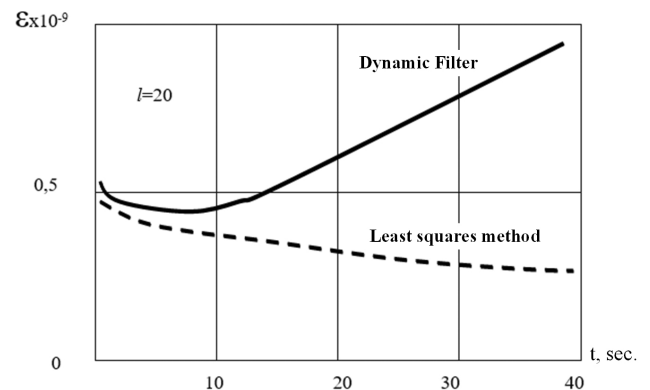


Fig. 6. Algorithm comparison results for “sliding window” with $l = 20$.

results. Analysis of graphs shows that LSM algorithm is sensitive to the window size l.

3. CONCLUSION

Developed data processing algorithm for instability processes of master generators of onboard radio systems makes it possible to significantly simplify evaluation of the model parameters in question. Additionally, use of a “sliding window” when evaluating the parameters being processed improves quality and speed of SC identification.

REFERENCES

1. Kozelkov SV. Primenenie planetnogo radiolokatora dlya zadach navigatsii kosmicheskikh apparatov. *Sistemy obrabotki informacii*, Khar'kov, NANU, PANM, HVU, 1999, 1(5);139-142. [Kozelkov SV. The use of planetary radar for spacecraft navigation tasks (in Russ.). *Sistemy obrabotki informacii*, Kharkiv, NANU, PANM, HVU, 1999, 1(5);139-142].
2. Issledovanie i razrabotka printsipov postroeniya, putej apparaturnoj realizatsii i povysheniya effektivnosti funkcionirovaniya spetsial'nyh sistem navigatsii i peredachi informatsii radiosignalami millimetrovogo diapazona voln. *Otchet o NIR (zaklyuchitel'nyj) p/ya M-5068*. “Raduga”, №398; inv. №2586, 1985, 74 s. [Research and development of the principles of construction, ways of hardware implementation and improvement of the efficiency of special navigation systems and information transmission by millimeter wave radio signals. Research report (final), the post M-5068, “Raduga”, n. 398; inv. n. 2586, 1985, 74 p.].
3. Kantor LYa. *Spravochnik po sputnikovoj svyazi i veshchaniyu*. Moscow, Radio i svyaz' Publ., 1986, 528 s. [Kantor LYa. Handbook of Satellite Communications and Broadcasting. Moscow, Radio i svyaz' Publ., 1986, 528 p.].
4. Chaki F. *Sovremennaya teoriya upravleniya: Nelinejnye, optimal'nye i adaptivnye sistemy*. Moscow, Mir Publ., 1975, 251 s. [Chaki F. Modern control theory: Nonlinear, optimal and adaptive systems. Moscow, Mir Publ., 1975, 251 p.].
5. Puhov GE. *Preobrazovaniya Tejlora i ikh primenenie v elektrotekhnike i elektronike*. Kiev, Naukova dumka Publ., 1978, 180 s. [Puhov GE. Taylor transformations and their application in electrical engineering and electronics. Kiev, Naukova dumka Publ., 1978, 180 p.].
6. Pupkov KA, Kapalin VI, Yushchenko AS. *Funkcional'nye ryady v teorii nelinejnykh sistem*. Moscow, Nauka Publ., 1978, 448 s. [Pupkov KA, Kapalin VI, Yushchenko AS. Functional series in the theory of nonlinear systems. Moscow, Nauka Publ., 1978, 448 p.].
7. Kozelkov SV. Progress kosmicheskoy tekhniki – ot “Shattla” do kosmicheskoy stancii. *Trudy IIER*, 1987, №3, 192 s. [Kozelkov SV. The progress of space technology - from the "Shuttle" to the space station (in Russ.). *Trudy IIER*, 1987, no. 3, 192 p.].
8. Pogorelov AI, Kupchenko LF. *Obshchie voprosy postroeniya signalov izmeritel'nykh radiosistem. Prostranstvenno-vremennaya obrabotka signalov*. Khar'kov, HAI Publ., 1986, s. 3-11. [Pogorelov AI, Kupchenko LF. General issues of building signals of measuring radio systems (in Russ.). *Prostranstvenno-vremennaya obrabotka signalov*. Khar'kov, HAI Publ., 1986, pp. 3-11.].
9. Kozelkov SV, Bogdanovskij AN, Polyakov AL, Rachinskij AP. *Matematicheskaya model' identifikatsii kosmicheskikh*

ob'ektov po nekontroliruemym izlucheniyam bortovoj apparatury kosmicheskikh apparatov. *Sistemy obrabotki informacii*, 2007, Vyp. 4, s. 51-55. [Kozelkov SV, Bogdanovskij AN, Polyakov AL, Rachinskij AP. Mathematical model of identification of space objects by uncontrolled radiation of onboard spacecraft equipment (in Russ.). *Sistemy obrabotki informacii*, 2007, vol. 4, pp. 51-55.].

DOI: 10.17725/rensit.2022.14.119

Radar Information Processing Algorithms in a Specialized Computer-Aided Design System

Maxim Yu. Konopel'kin, Sergey V. Petrov, Daria A. Smirnyagina

"Almaz-Antey" Air and Space Defence Corporation, <http://www.almaz-antey.ru/>

Moscow 121471, Russian Federation

E-mail: m.konopelkin@almaz-antey.ru, sv.petrov@almaz-antey.ru, ponyoo@mail.ru

Received May 20, 2022, peer-reviewed May 27, 2022, accepted June 3, 2022

Abstract: A brief description of the radar CAD software modules responsible for this functionality is given. The module of engineering calculations and simulations allows you to set the scenario of the interference-target situation and conduct a complete, close to reality, simulation of the behavior of the radar in combat conditions. The visual functional editor provides the ability to create a radar simulation model in the form of a graph of streaming calculations from interconnected parameterizable blocks. The library of parameterizable modeling blocks contains modeling blocks designed for calculations and modeling of structural and functional parts of developed radar stations, complexes, systems. Simulation model of an active single-position pulse-Doppler sector-observation radar with electronic beam scanning was created. The following algorithms are implemented in the model: the sum-difference monopulse direction finding algorithm, the MUSIC superresolution direction finding algorithm, and the projection adaptive spatial filtering algorithm. A simulation experiment was carried out with a radar model in three scenarios of an interference-target environment, which differ in the presence of interfering signals. Analysis of the results of the simulation experiment shows that the operation of the algorithms corresponds to the theoretical prediction. The abilities of radar CAD presented in this article can be used by specialists in radar and signal processing.

Keywords: radar station, computer-aided design system, simulation modeling, radar data processing algorithm

UDC 004.94

For citation: Maxim Yu. Konopel'kin, Sergey V. Petrov, Daria A. Smirnyagina. Radar Information Processing Algorithms in a Specialized Computer-Aided Design System. *RENSIT: Radioelectronics. Nanosystems. Information technologies*, 2022, 14(2):119-126e. DOI: 10.17725/rensit.2022.14.119.

CONTENTS

- | | |
|---|---|
| <ol style="list-style-type: none"> 1. INTRODUCTION (120) 2. RADAR CAD TOOLKIT (120) <ol style="list-style-type: none"> 2.1. MODULE OF ENGINEERING CALCULATION AND SIMULATION (120) 2.2. VISUAL FUNCTIONAL EDITOR (121) 2.3. LIBRARY OF PARAMETERIZABLE SIMULATION BLOCKS (122) 2.4. RADAR SIMULATION MODEL (122) 3. SIMULATION EXPERIMENT (123) <ol style="list-style-type: none"> 3.1. RADAR SIMULATION MODEL PARAMETERS (123) | <ol style="list-style-type: none"> 4. RADAR SIMULATION ALGORITHMS (123) <ol style="list-style-type: none"> 4.1. MONOPULSE DIRECTION FINDING ALGORITHM (123) 4.2. DIRECTION FINDING ALGORITHM FOR STOCHASTIC SIGNAL SOURCES (124) 4.3. ADAPTIVE SPATIAL FILTERING ALGORITHM (124) 5. SIMULATION SCENARIO (124) <ol style="list-style-type: none"> 5.1. SIMULATION RESULTS (124) 6. CONCLUSION (125) |
|---|---|

REFERENCES (125)

1. INTRODUCTION

The most part of tasks for performance evaluation of the combat use of various equipment in the aerospace defense system are complex and cannot be reduced to a simple arithmetic sum of mathematical models that are poorly interconnected and tasks for calculating particular indicators. The current level of development of computer technology and mathematical methods for studying complex systems creates objective prerequisites for the system concept of designing complex technical systems, which requires fundamental changes in the methodology of their creation and development. The system approach involves the creation of effective complexes of particular mathematical models of subsystems, which together describe the behavior of the entire system, and computational tasks that function as part of modeling and design systems on a unified information base [1,2].

The computer-aided design system (CAD) for radars, radar complexes and radar systems, as well as their components, is an example of the implementation of the system concept [3-10]. The systematic nature of the calculations in the radar CAD implies:

- a unified methodology for preparing and presenting initial data, as well as calculating and presenting results;
- an equal degree of detail for each particular task (model) solved by users of the same level;
- a specific logical sequence of calculations in each particular task and in their totality;
- obtaining both intermediate and final results for each calculation task in a form convenient for their application in other tasks without additional processing and transformation;
- the possibility of independent calculations for each calculation problem, mathematical model and the use of intermediate and final results in other tasks.

The systematic approach implemented in the radar CAD provides for the unity of information, mathematical, linguistic, software and organizational support.

From the standpoint of a systematic approach, simulation models are the most proper for performance evaluation of complex systems. Therefore, as part of the radar CAD, simulation models of the functioning of the radar have been developed, which, unlike many of the currently existing mathematical models of the radar, make it possible to model in detail the processes of primary and secondary processing of various types of signals reflected from air, ballistic and space objects in a full polarization basis.

This article is devoted to an overview and demonstration of the capabilities of radar CAD in terms of developing and modeling algorithms for processing radar information. The article addresses the following questions:

- description of radar CAD tools, including module of engineering calculation and simulation, visual functional editor and library of parameterizable simulation blocks;
- outlined the principles of assembling simulation models of the radar;
- test simulation of the radar model and its algorithms is described;
- a simulation experiment was carried out, its results are presented.

2. RADAR CAD TOOLKIT

2.1. MODULE OF ENGINEERING CALCULATION AND SIMULATION

One of the key features of the developed radar CAD is the possibility of not only automating the radar development process, but also a fairly wide and comprehensive modeling of the behavior of the radar in combat conditions. In particular, when designing, the engineer is given the opportunity to set a scenario. When sending the scenario for calculation, a complete, close to reality, simulation of the behavior of the

radar in combat conditions is performed. An imitation of a raid on a radar station is carried out, which includes the simulation of the movement of various air targets. At the same time, on the basis of the constructed radar model, the operation of the radar antenna is modeled, it scans the space. During the interaction of an electromagnetic wave that came from the locator antenna beam and an air target, the reflection of an electromagnetic wave from this target is simulated, on the basis of which the signal that came into the receiving channel of the locator is calculated, where, further, its processing is simulated. Noises are superimposed on the incoming signal, which arise, among other things, due to reflection from the Earth's surface. Also, when modeling the transition of a beam through the atmosphere, various kinds of precipitation are taken into account.

The interface of the module of engineering calculations and modeling that implements these capabilities is shown in **Fig. 1**.

During the simulation, a file of the protocol of the simulation experiment is recorded,

containing information about the position of all radars and air targets presented in the scenario, and the results of the radar operation. As a result of processing the simulation protocol file in the performance evaluation module, the quality indicators of radar information received from the radar are calculated.

2.2. VISUAL FUNCTIONAL EDITOR

In radar CAD, to create simulation models, an approach known as “dataflows programming” is used [11]. Popular representatives of software tools using this approach are Simulink and LabView.

The user, using the visual constructor, creates a calculation graph from blocks, configures the parameters of each block and the connections between them. By pressing the start calculation button, the graph is traversed and the output data of each block is calculated based on the input data and block parameters.

The advantages of this paradigm are a natural visual representation (in the form of a calculation graph) and support for parallelism.

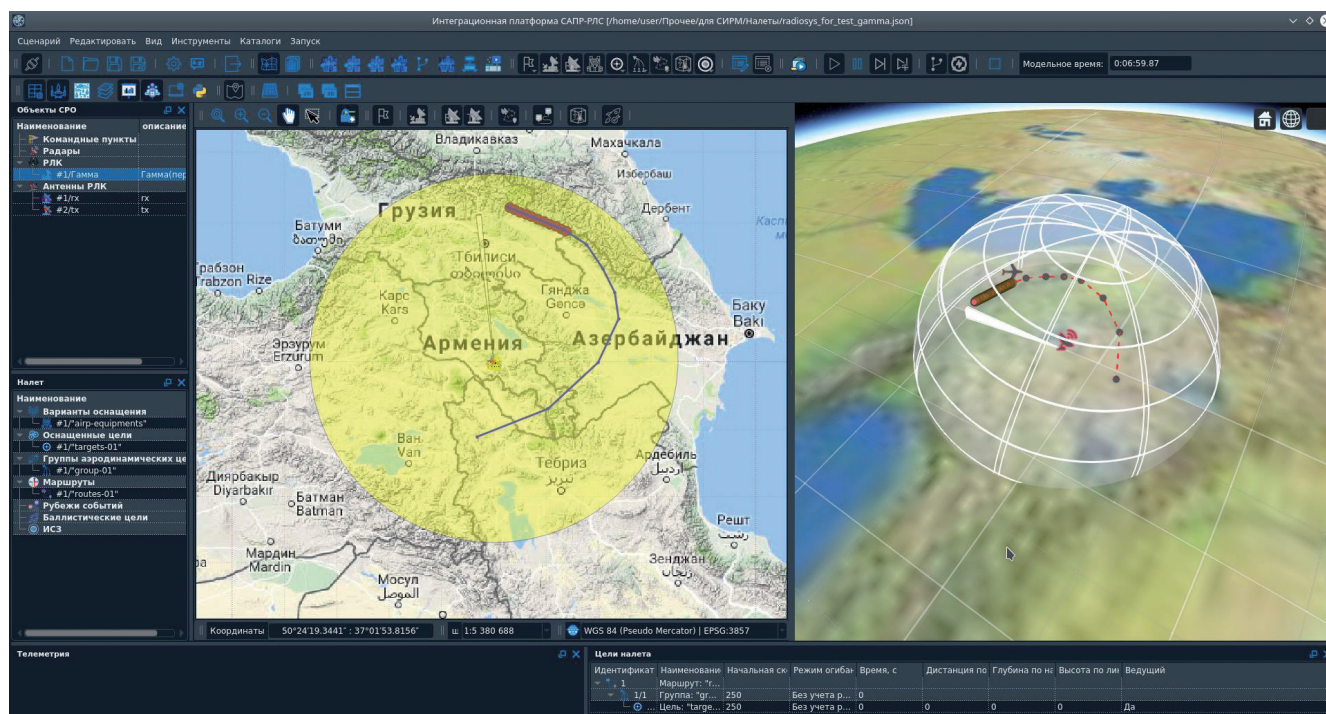


Fig. 1. The interface of the module of engineering calculation and simulation.

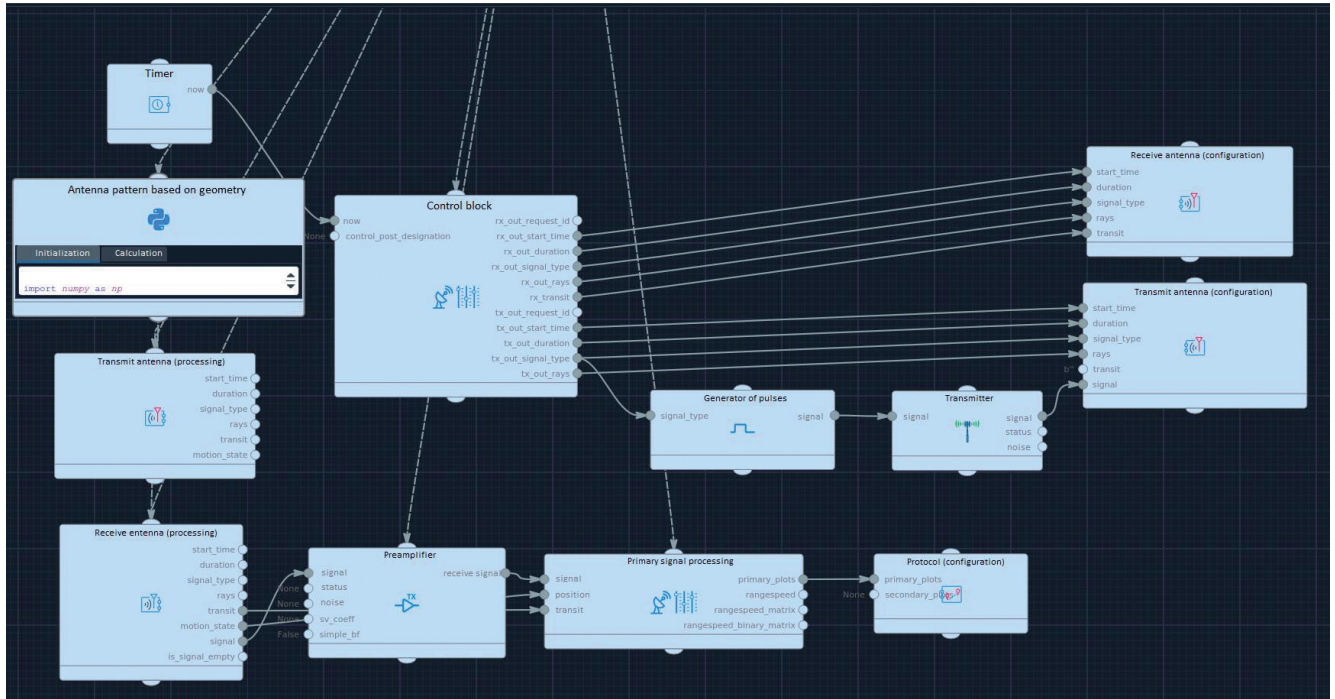


Fig. 2. A typical scheme of the radar model.

A visual functional editor has been developed as part of the radar CAD, which provides the ability to create and calculate a data-flow graph. The graphical user interface is a classic Simulink-like interface for visual design of stream data processing, consisting of parameterizable interconnected blocks (Fig. 2).

2.3. LIBRARY OF PARAMETERIZABLE SIMULATION BLOCKS

When modeling a radar, two levels of abstraction can be distinguished: the lower one, that is, the modeling of particular modules and units (generators, antennas, algorithmic blocks, etc.) and the upper one, that is, the model of the system as a whole. At the same time, if the principle of modularity is kept, then the same set of components can be used to simulate various types and configurations of radars.

In addition, if the program code responsible for the internal operation of particular modules is placed in a separate well-debugged and documented library, then the development of the upper level of abstraction can be highly simplified: the developer of a particular simulation model will need to go into the details

of mathematically complex signal processing algorithms inside individual modules.

To do this, the functional editor includes a library of parameterizable simulation blocks designed for calculations and modeling of the structural and functional parts of the developed radar stations, complexes, systems. The library includes a basic set of blocks that represents an opportunity to create a radar model.

2.4. RADAR SIMULATION MODEL

The main object in simulation modeling is the simulation model of the radar. The radar simulation model in the radar CAD is represented as a set of functional blocks. A typical radar model consists of the following functional blocks:

- generator of radar signals;
- transmitter;
- transmitting antenna;
- receiving antenna;
- beamformer;
- receiver;
- digital signal processing block;
- primary information processing block;
- secondary information processing block;
- operating mode control block.

As seen, the accepted division of the model into blocks corresponds to the classical functional scheme of the radar, known from the literature [12]. At the same time, the open architecture of radar CAD does not impose restrictions on the user - the configuration of blocks in the model can be arbitrary. New blocks that have the functionality necessary for the user can be developed in the programming languages Python, MATLAB and C ++.

3. SIMULATION EXPERIMENT

3.1. RADAR SIMULATION MODEL PARAMETERS

To demonstrate the capabilities of radar CAD in terms of developing and modeling processing radar information algorithms, an airspace surveillance radar simulation model with a set of parameters typical for this class was created [12].

Radar type - active, single-position, sector surveillance with electronic beam scanning.

Signal parameters:

- signal type – chirp;
- carrier frequency = 1.2 GHz;
- signal bandwidth = 1 MHz;
- pulse duration = 200 μs;
- pulse repetition period = 2 ms;
- pulse power = 20 kW.

Antenna parameters:

- type of antenna - digital antenna array (DAA);
- size in elements = 12x16;
- step of elements = 0.5 wavelength;
- gain factor = 28 dB;
- scanning sector in azimuth = -45° – 45°;
- scanning sector in elevation = 0° – 30°;
- antenna tilt to the horizon = 15°.

4. RADAR SIMULATION ALGORITHMS

The radar simulation model implements a typical signal generation and processing scheme for a pulse-Doppler radar, which looks like this:

- generation of a chirp signal;
- calculation of the phase distribution for beamforming;
- filtering the received signal by range using a matched filter;

- short-time Fourier transform for a range-velocity matrix;
- binarization of the range-velocity matrix using a detector with a constant false alarm rate;
- search connected regions of the binary range-velocity matrix;
- reproduction of connected regions for other ranges and speeds for a specific pulse burst;
- search for intersections between multiplied connected regions obtained from different bursts;
- for those regions that intersect with a sufficient number of regions from other bursts (for example, in the case of intersection of regions from three different pulse bursts), the indicators are averaged and a target mark is issued.

In addition, a passive channel is implemented in the radar model, which implements the processing of stochastic signals from external sources. In this case, training data with a DAA of length $K = 384$ time samples are used.

To illustrate the capabilities of the radar CAD, the following algorithms have been implemented and simulated. Для иллюстрации возможностей САПР РАС реализованы и промоделированы следующие алгоритмы.

4.1. MONOPULSE DIRECTION FINDING ALGORITHM

The model implements the sum-difference direction finding algorithm [13], in which the corrections of the target angular coordinates in the generalized biconical coordinate system are calculated by the formulas:

$$\Delta_u = \hat{u} - u_0 = -\gamma_u \operatorname{Re} \left(\frac{\mathbf{W}_u^H \mathbf{X}}{\mathbf{W}^H \mathbf{X}} \right),$$

$$\Delta_v = \hat{v} - v_0 = -\gamma_v \operatorname{Re} \left(\frac{\mathbf{W}_v^H \mathbf{X}}{\mathbf{W}^H \mathbf{X}} \right),$$

where \hat{u} , \hat{v} is the estimation of the target angular coordinates, u_0 , v_0 are the angular coordinates of the sum beam maximum, γ_u , γ_v are the slope coefficients of the direction-finding characteristic (determined by the array geometry), \mathbf{W} is the

weight vector for the formation of the sum beam, \mathbf{W}_u is the weight vector for the formation of the difference beam in azimuth, \mathbf{W}_v is weight vector for forming a difference beam in elevation, \mathbf{X} is the vector of signals from the antenna array, $(\bullet)^H$ is the Hermitian conjugacy symbol. The denominator of the fractions on the right side of the equalities represents the signal at the output of the sum beam, the numerator is the signal at the output of the difference beam (azimuth or elevation, respectively).

4.2. DIRECTION FINDING ALGORITHM FOR STOCHASTIC SIGNAL SOURCES

For direction finding of sources of stochastic signals, the MUSIC algorithm is implemented, which uses the calculation of the spatial spectrum according to the formula [14]

$$Q_M = \frac{1}{\mathbf{V}^H \hat{\mathbf{P}}_n \mathbf{V}},$$

where $\hat{\mathbf{P}}_n$ is the projection matrix onto the noise subspace of the sample estimate of the spatial covariance matrix $\hat{\mathbf{R}} = \frac{1}{K} \mathbf{X}\mathbf{X}^H$, \mathbf{V} is the hypothesis vector of the amplitude-phase distribution in the antenna opening for a predefined angular direction.

4.3. ADAPTIVE SPATIAL FILTERING ALGORITHM

The model implements a projection algorithm for calculating the adaptive weight vector according to the formula [14]

$$\mathbf{W}_a = \hat{\mathbf{P}}_n \mathbf{S},$$

where \mathbf{S} is the steering vector.

All of the above algorithms are implemented in the blocks of the radar model in Python using the NumPy and SciPy modules.

5. SIMULATION SCENARIO

The radar model was located in the area of St. Petersburg. Two azimuthally spaced aerodynamic targets were set (Fig. 3) with the possibility of assignment stochastic signal sources on them. In terms of their presence, three scenarios were modeled:

- 1) there are no sources of stochastic signals;
- 2) one source of stochastic signals;
- 3) two sources of stochastic signals.

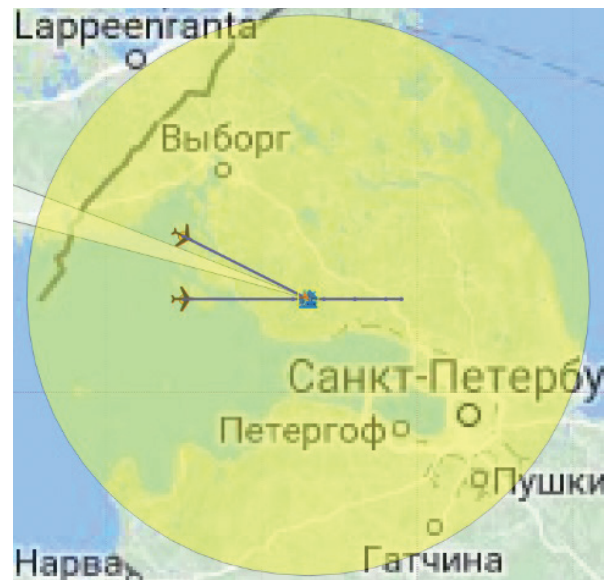


Fig. 3. The position of the radar and targets.

5.1. SIMULATION RESULTS

5.1.1. MONOPULSE DIRECTION FINDING ALGORITHM

The first scenario was used to test the operation of the monopulse direction finding algorithm. The results of the locator for the first target are shown in Fig. 4. The figure shows the indicator "azimuth-elevation angle", the yellow circle is the receiving beam at a level of 3 dB, the blue dot is the true position of the target, the red dots are estimates of the angular coordinates of the target. As seen, the implemented monopulse direction finding algorithm correctly refines the angular coordinates of the target.

5.1.2. DIRECTION FINDING ALGORITHM FOR STOCHASTIC SIGNAL SOURCES

Scenario 3 was used to test the operation of the direction finding algorithm for sources of stochastic signals. In this scenario, two sources of stochastic signals were found. Spatial spectrum in the generalized biconical system coordinates (horizontal axis - azimuth, vertical - elevation) is

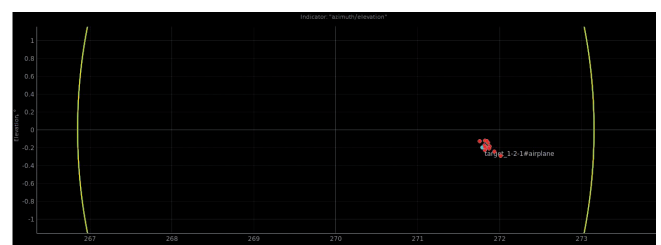


Fig. 4. Indicator "azimuth-elevation".

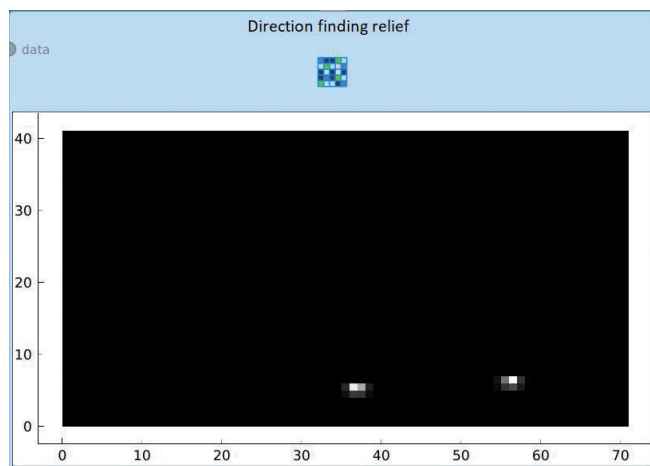


Fig. 5. Spatial spectrum of MUSIC in scenario 3.

based on the results of the MUSIC algorithm, is shown in Fig. 5. Estimates of the angular coordinates of the sources of stochastic signals in the spherical coordinate system are as follows:

- 1st source – (1.3°; 0.3°), true position – (1.8°; -0.2°);
- 2nd source – (27.5°; 0.3°), true position – (27.2°; -0.2°).

As seen, the estimates coincide with the true position of the sources to within fractions of a degree. When using a grid of angles with a smaller discrete when constructing the spatial spectrum, it is possible to increase the accuracy of the estimate.

5.1.3. ADAPTIVE SPATIAL FILTERING ALGORITHM

Scenario 2 was used to test the operation of the adaptive spatial filtering algorithm. In the presence of one interfering signal source located on the right target, the central target was detected, marks were issued (yellow markers in Fig. 6, blue markers - the true position of the targets). The target with the source of the

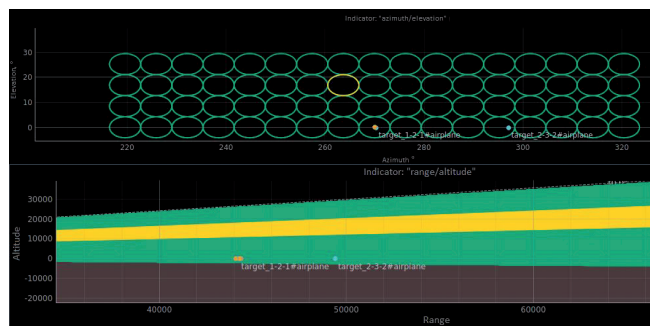


Fig. 6. Indicators "azimuth-elevation" and "range-altitude" in scenario 2.

interfering signal was not detected, because the ASF algorithm cannot suppress the interfering signal, the angular direction of which coincides with the direction of the true signal of the target.

6. CONCLUSION

The domestic radar CAD has great opportunities for developing models of radar operation, which make it possible to model in detail the processes of processing various types of signals. For this, a visual functional editor is used, in which the radar model is assembled from a set of blocks. The module of engineering calculation and simulation gives great opportunities to place the created radar model on the ground and set the raid scenario. To demonstrate these capabilities, a model of a sector surveillance radar with electronic beam scanning was created, in which a passive channel is implemented that implements the processing of stochastic signals from external sources. The following algorithms have been implemented and modeled in three scenarios of the interference-target environment: the monopulse direction finding algorithm, the direction finding algorithm for stochastic signal sources, and the adaptive spatial filtering algorithm. The results of the algorithms work correspond to the theoretical forecast.

REFERENCES

1. Kontorov DS, Golubev-Novozhilov YS. *Vvedeniye v radiolokatsionnyuyu sistemotekhniku* [Introduction to Radar Systems Engineering]. Moscow, Sovetskoe Radio Publ., 1971, 366 p.
2. Petukhov GB, Yakunin VI. *Metodologicheskiye osnovy vneshnego proyektirovaniya tselenapravlennykh protsessov i tselestremlennykh system* [Methodological foundations of external design of purposeful processes and purposeful systems]. Moscow, AST Publ., 2006, 504 p.
3. Sozinov PA, Konoval'chik AP. *Osnovnyye podkhody k razrabotke otechestvennoy sistemy avtomatizirovannogo proyektirovaniya radiolokatsionnykh stantsiy i tekushchiye rezul'taty* [Main approaches

- to the development of a domestic system of computer-aided design of radar stations and current results]. *Radioelektronnaya bor'ba*, 2020, 1(1):62-74 (in Russ.).
4. Sozinov PA, Konoval'chik AP, Saushkin VP. Aktual'nyye voprosy sozdaniya otechestvennoy SAPR dlya proyektirovaniya RLS [Topical issues of creating domestic CAD for radar design]. *Vestnik vozdushno-kosmicheskoy oborony*, 2019, 3(23):106-119 (in Russ.).
 5. Konoval'chik AP, Konopel'kin MY, Plaksenko OA, Shchiryay AO. Postanovka zadachi razrabotki i predvaritel'naya arkhitektura otechestvennoy SAPR RLS polnogo skvoznogo tsikla [Statement of the task of development and preliminary architecture of the domestic CAD radar of a full end-to-end cycle]. *Novyye informatsionnyye tekhnologii v avtomatizirovannykh sistemakh*, 2017, 20:127-130 (in Russ.).
 6. Konoval'chik AP, Plaksenko OA, Shchiryay AO. Kontseptsiya mnogourovnevnogo proyektirovaniya RLS v razrabatyvayemoy SAPR RLS polnogo skvoznogo tsikla [The concept of multi-level design of radars in the developed CAD radar of a full end-to-end cycle]. *Fundamental'nyye problemy radioelektronnogo priborostroyeniya*, 2017, 17(4):889-892 (in Russ.).
 7. Konoval'chik AP, Konopel'kin MY, Plaksenko OA, Shchiryay AO. Otechestvennaya sistema avtomatizirovannogo proyektirovaniya radiolokatsionnykh sistem, kompleksov i stantsiy s uchetom sredstv vozdushno-kosmicheskogo napadeniya [Domestic system for computer-aided design of radar systems, complexes and stations, taking into account the means of aerospace attack]. *Naukoyemkiye tekhnologii v kosmicheskikh issledovaniyakh Zemli*, 2018, 10(1):40-47 (in Russ.).
 8. Konoval'chik AP, Plaksenko OA, Shchiryay AO. Funktsii imitatsii boyevykh deystviy v razrabatyvayemoy otechestvennoy SAPR RLS polnogo skvoznogo tsikla [Functions of simulating combat actions in the developed domestic CAD radar of a full end-to-end cycle]. *Voprosy radioelektroniki*, 2018, 3:30-34 (in Russ.).
 9. Konoval'chik AP, Plaksenko OA, Shchiryay AO. Realizatsiya imitatsionnogo modelirovaniya v razrabatyvayemoy otechestvennoy SAPR RLS polnogo skvoznogo tsikla [Implementation of simulation modeling in the developed domestic CAD radar of a full end-to-end cycle]. *Novyye informatsionnyye tekhnologii v avtomatizirovannykh sistemakh*, 2018, 21:290-293 (in Russ.).
 10. Konoval'chik AP, Plaksenko OA, Shchiryay AO. Obosnovaniye oblika perspektivnykh radiolokatsionnykh stantsiy posredstvom razrabatyvayemoy otechestvennoy sistemy avtomatizirovannogo proyektirovaniya [Substantiation of the appearance of promising radar stations using the developed domestic computer-aided design system]. *Naukoyemkiye tekhnologii v kosmicheskikh issledovaniyakh Zemli*, 2019, 11(1):4-11 (in Russ.).
 11. Van-Roy P, Haridi S. *Concepts, Techniques, and Models of Computer Programming*. Prentice-Hall, 2004, 900 p.
 12. Skolnik MI. *Radar Handbook, Third Edition*. McGraw-Hill, 2008.
 13. Ratynskiy MV, Porsev VI. *Monoimpul'snaya pelengatsiya v RLS s tsifrovymi FAR* [Monopulse direction finding in radar with digital phased array]. Moscow, Radiotekhnika Publ., 2019, 160 p.
 14. Van Trees HL. *Detection, estimation and modulation theory. Part IV. Optimum array processing*. Wiley, 2002.

DOI: 10.17725/rensit.2022.14.127

Primary chemical current sources in research studies of recent years: a review

Tatiana V. Krupina, Dmitriy S. Ermakov, Alexander O. Zhbakov, Sergey P. Gubin, Denis Yu. Kornilov

Scientific production company "Grafenika", www.grafenika.ru/
Moscow 107143, Russian Federation

E-mail: tatiana.v.krupina@gmail.com, jermakov.dmitry@yandex.ru, zhbakov1995@mail.ru, gubin@igic.ras.ru, kornilovdenis@rambler.ru

Received May 20, 2022, peer-reviewed May 27, 2022, accepted June 3, 2022

Abstract: The paper reviews the world research in the field of primary chemical current sources (CCS) from 2016 to the present. Publications in the field of development and modification of anode and cathode materials for primary CCS, as well as electrolytes used in them, are considered. Both studies on classical materials that have proven themselves in recent decades, and the developing direction of creating environmentally friendly and safe elements are noted. Increasingly, alloys are being used to improve the discharge characteristics of batteries. The use of carbon materials, including graphene and graphene oxide with their unique properties, is widespread. Polymer electrolytes have been developed as a profound way to create safer energy sources. The number of scientific works in the field of primary CCS indicates the continuing need for efficient non-rechargeable systems for both domestic and specialized needs of mankind.

Key words: primary battery, composite materials, polymer electrolyte, graphene, graphene oxide, lithium batteries, energy source

UDC 544.6.018.2

For citation: Tatiana V. Krupina, Dmitriy S. Ermakov, Alexander O. Zhbakov, Sergey P. Gubin, Denis Yu. Kornilov. Primary chemical current sources in research studies of recent years: a review. *RENSIT: Radioelectronics. Nanosystems. Information technologies*, 2022, 14(2):127-142e. DOI: 10.17725/rensit.2022.14.127.

CONTENTS

1. INTRODUCTION (127)
2. ANODE (130)
 - 2.1. MULTI-COMPONENT MATERIALS (130)
 - 2.2. MODERNIZATION OF STRUCTURE AND SURFACE (131)
3. CATHODE (131)
 - 3.1. FLUOROCARBON (132)
 - 3.1.1. CF_x IN LITHIUM SYSTEMS (132)
 - 3.1.2. CF_x IN NON-LITHIUM SYSTEMS (133)
 - 3.2. COMPOSITE MATERIALS (133)
 - 3.2.1. LITHIUM SYSTEMS WITH COMPOSITE MATERIALS (133)
 - 3.3. GRAPHENE (134)
 - 3.3.1. GRAPHENE IN LITHIUM SYSTEMS (134)
 - 3.3.2. GRAPHENE IN NON-LITHIUM SYSTEMS (134)
 - 3.4. ME-AIR (135)

3.5. ECO-FRIENDLY CATHODE MATERIALS (136)

4. ELECTROLYTE (136)
 - 4.1. IONIC LIQUIDS (136)
 - 4.2. POLYMER ELECTROLYTES (137)
 - 4.3. WATER ELECTROLYTES (137)
5. CONCLUSION (138)
- REFERENCES (138)

1. INTRODUCTION

Modern life is impossible to imagine without portable energy sources. From watch on the wrist to launch of the spacecraft to the borders of the Solar System - everywhere there is a need for the generation of electrical energy. Just as torches once lit a path in darkness, progress opened up new opportunities for humanity, replacing these torches with lanterns. In the early 18th century,

in less than a century, the world changed forever. The appearance of the first chemical current sources (CCS) marked the beginning for an extensive field of research, in which work is constantly being carried out to improve existing systems and create new ones that meet rigid requirements of technical progress.

CCS is a device in which the energy of chemicals is converted into electrical energy [1-11]. CCS consists of one or more galvanic cells – two electrodes separated by an electrolyte. The execution of a chemical reaction is due to the

nature of these constituents. At the boundaries between the electrodes, first-class conductors, and the electrolyte, a second-class conductor, current-forming reactions occur – oxidation and reduction reactions. The electrode on which the oxidizing agents are oxidized is called the anode, and the electrode on which the oxidizing agents are reduced is called the cathode. At the negative anode, the reducing agent is oxidized, the resulting free electrons pass through the external circuit to the positive cathode, where they participate in the oxidant reduction reaction.

Table 1

Types and fields of application of batteries

Battery type	Application area	Devices
Saline (manganese-zinc)	At home	- remote controls, clocks, scales, simple children's toys, electronic thermometers and other devices with low power consumption
Alkaline (manganese-zinc)	At home	- scales, electronic clocks, remote controls, lamps
	Media	- cameras with flash, camcorders, lighting systems, radios, portable players
	Military	- radio beacons, radios, flashlights, radio-controlled models
	Kids toys	- radio-controlled models, toys with a speaker, etc.
	Medicine	- electronic devices for measuring of blood pressure, body temperature, hearing aids, Holter monitors
Silver (silver-zinc)	Office equipment	- PC motherboards, laser pointers, calculators
	Military	- microflashlights, microchips, radio beacons
	Medicine	- hearing aids, pacemakers
	Other	- musical cards, watches
Mercury	Medicine	- pacemakers, hearing aids
	Military	- night vision devices, portable radio equipment for military purposes, spacecraft, alarm devices, rescue equipment, combat missiles and torpedoes
	Other	- electronic clocks, photoexposure meters, cameras, monitoring systems, control devices for drilling oil and gas wells, rescue equipment
Lithium	IT	- sensors for intelligent parking systems, environmental monitoring equipment, data loggers, energy management systems, equipment for "smart buildings"
	Medicine	- Defibrillators, respirators and oxygen concentrators, continuous monitoring equipment, mobile diagnostic equipment, infusion pumps, telemedicine equipment, pacemakers
	Military	- portable radio communications, night vision devices and thermal vision devices, shooting accuracy training simulators, gas detectors, field radars, weapon systems and ignition systems, flashlights and lamps
	Oil and gas	- systems for measuring parameters while drilling, LWD devices, equipment for pumping and operating wells, subsea equipment, devices for working in an explosive environment, equipment for seismic exploration, pipeline cleaning devices
	Professional electronics	- professional handheld devices and portable devices, professional monitors, ticket terminals and information desks, transport integrated information facilities
	Safety	- security surveillance systems for home and swimming pool, smoke and CO ₂ detectors, security systems with blocking, video surveillance, wireless sirens, manual fire alarms, passive infrared presence detectors, glass break detectors, perimeter protection, biometric readers, non-contact card readers and complex wireless alarm systems
	Tracking	- equipment tracking systems, vehicle tracking systems, toll road transponders
	Energy metering and control	- automatic metering devices, intelligent metering systems for electricity, water, gas and heat, stationary telecommunication devices for the global computer network
	Other	- buoys, signal lamps, beacons, life jackets, toys (musical, radio-controlled), scales, watches, laptops, microchips, etc.

Thus, a stream of negatively charged electrons creates a current.

There are several types of CCS. Primary CCS are called batteries, current sources intended for single use. Rechargeable batteries are secondary CCS, they are capable of being repeatedly charged and discharged by converting the chemical energy of active substances into electrical energy and backward. There are current sources, the active substances (fuel and oxidizer) of which are outside the cell and are supplied separately – fuel cells.

Nowadays, rechargeable batteries are the most popular. Due to the reversibility of chemical reactions inside the storage battery, such a power source can be reused many times. Rechargeable batteries are found in cars and mobile phones, and are used in household appliances and electronics. Thanks to the rechargeable batteries, the carriages are illuminated and computers work in case of an emergency power outage. It seems that rechargeable CCSs should already oust its simplest competitors from the market.

However, the primary CCSs, batteries, are still needed where the use of rechargeable batteries is difficult or economically impractical. Often, without batteries, the work of a child's toy, a medical device, and even a spacecraft is impossible (**Table 1**).

There is a wide variety of primary CCSs on the market today. Some of systems are presented in **Table 2** [1].

Despite the apparent simplicity of the design, the number of proposed modifications to the shape and composition of the battery is growing steadily every year. Along with traditional materials – lithium, various alkali metals, lead and manganese compounds – multicomponent alloys, rare metals, organic compounds and even air are used to create anodes and cathodes. Separators are made of paper, plastic, modified fibers. The composition of electrolytes ranges from complex biocompatible compounds to plain water, and liquids are replaced by gels and solids. And if the inner part of the batteries remains more the subject of interest of

Table 2

Current-producing reactions and theoretical parameters of the main primary CCS

System	Current-generating reaction	Ucc, B	Theoretical energy density, W·h/kg
Zn NH ₄ Cl MnO ₂	2MnO ₂ + Zn + 2NH ₄ Cl = 2MnOOH + [Zn(NH ₃) ₂]Cl ₂	1.7	260
Zn ZnCl ₂ MnO ₂	2MnO ₂ + Zn + 2H ₂ O + ZnCl ₂ = 2MnOOH + 2Zn(OH)Cl	1.6	208
Zn KOH MnO ₂	2MnO ₂ + Zn + 2H ₂ O = 2MnOOH + Zn(OH) ₂	1.6	312
Zn KOH HgO	HgO + Zn = Hg + ZnO	1.35	256
Zn KOH Ag ₂ O	Ag ₂ O + Zn = 2Ag + ZnO	1.6	288
Zn KOH Воздух	O ₂ + 2Zn = 2ZnO	1.64	1344
Zn NaOH CuO	CuO + Zn + 2NaOH + 2H ₂ O = Cu + Na ₂ [Zn(OH) ₄]	1.06	215
Cd KOH HgO	HgO + Cd + H ₂ O = Hg + Cd(OH) ₂	0.91	140.6
Mg Mg(ClO ₄) ₂ MnO ₂	2MnO ₂ + Mg + 2H ₂ O = 2MnOOH + Mg(OH) ₂	2.96	675
Li LiClO ₄ , ПК MnO ₂	MnO ₂ + Li = LiMnO ₂	3.5	1075
Li LiBF ₄ , ПК (CF) _n	(CF) _n + nLi = nLiF + C _n	2.82	2192
Li LiClO ₄ , ДОЛ CuO	CuO + 2Li = Cu + Li ₂ O	2.24	1285
Li LiClO ₄ , ДОЛ Cu ₄ O(PO ₄) ₂	Cu ₄ O(PO ₄) ₂ + 8Li = 4Cu + Li ₂ O + 2Li ₃ PO ₄	2.8	1146
Li LiClO ₄ , ПК, ДМО FeS ₂	FeS ₂ + 4Li = Li ₂ S + Fe	1.75	1273
Li LiBr, АН SO ₂	2SO ₂ + 2Li = Li ₂ S ₂ O ₄	3.1	1175
Li LiAlCl ₄ , SOCl ₂ SOCl ₂	SO ₂ Cl ₂ + 4Li = S + SO ₂ + 4LiCl	3.66	1477
Li LiAlCl ₄ , SO ₂ Cl ₂ SOCl ₂	SO ₂ Cl ₂ + 2Li = 2LiCl + SO ₂	2.91	1405
Li LiAsF ₆ , ПК, ДМЭ Ag ₂ CrO ₄	Ag ₂ CrO ₄ + Li = Li ₂ CrO ₄ + 2Ag	3.35	515
Li LiI ₂ I ₂ , ПВП*	I ₂ + 2Li = 2LiI	2.8	560

*polyvinylpyridine

specialists, then the variety of shapes and sizes of batteries is now known to absolutely anyone. Cylindrical, rectangular, round cases have long found their standard size names like AA, AAA, C, D, etc. New types of batteries regularly add to this list, and what was a prototype in the laboratory yesterday is now becoming the new standard for power supplies.

This review aims to analyze the work in the development of primary CCS over the past 7 years. The main attention is paid to the synthesis and research of cathode and anode materials, as well as electrolytes.

2. ANODE

The structural element of the primary current source, which determines the type of battery, is the anode. Currently, anode materials based on zinc, nickel, magnesium, aluminum, lithium, as well as their alloys, that is, multicomponent systems, are widely used [12].

2.1. MULTI-COMPONENT MATERIALS

To obtain an anode material based on a multicomponent system, the casting method is used in most cases. Mixture of metal powders is melted in a furnace in a gas environment and poured into a prepared form, and at the next step the workpieces are subjected to homogenizing annealing. Using this technique, anodes for Mg-Air batteries are made based on AZ 31, Mg - Li - Al - Ce, Mg - Al - Pb alloys, which have an energy density of about 25 mW/cm². In order to improve this indicator, an alloy based on Mg - Al - Sn was obtained [13]. The discharge characteristics shown that Mg-Air cell on the basis of alloy Mg - Al - Sn provides a higher peak energy density - 94.1 mW/cm² - than that of the alloy anodes AZ 31, Mg - Li - Al - Ce, Mg - Al - Pb. In addition, the resulting alloy was found to have a lower content of harmful discharge products.

Extruded Mg-9Al-xIn alloys are systematically studied as a potential anode material for primary Mg-air batteries [14]. Research has shown that the addition of indium to a magnesium alloy

has a strong positive effect on many parameters. Efficiency of the anode based on Mg-9Al-0.5In is 78.2% at a current of 150 mA/cm², which is significantly higher than the values of magnesium alloys without indium. In addition, the test alloy exhibits a high cell voltage and energy density of about 76.8 mW/cm².

A significant effect on the structure and, respectively, the energy parameters of the final battery has alloys annealing temperature [15]. This is illustrated by the example alloy and Mg-6%Al-1%Sn-1%In (wt.%). Sheet blanks with a thickness of 2 mm were obtained by hot extrusion. After annealing at the temperature of 200°C, 250°C and 300°C, the alloy sheets were tested. As shown by the test results, cells with an anode of Mg-Al-Sn-In have the best performance and can provide an average voltage of 1.527 V at a specific energy of 98.3 W·h/kg. Such results are substantiated by a homogeneous microstructure, fine grains, and small crystal defects.

Binary alloys Mg-xLa (x = 0.2-0.8 wt.%) were investigated as anode materials for magnesium-based batteries. The results show that the magnesium matrix corrosion rate decreases with lanthanum alloying, and it can be associated with the formation of a protective film on the surface of the alloy, containing La₂O₃. However, with an increase in the content of lanthanum, the protective properties deteriorate: an increase in the microgalvanic corrosion reaction is observed, caused by an increase in the amount of the intermetallic phase Mg₁₂La; however, all Mg-La alloys had a corrosion rate less than pure magnesium. Mg-La alloys with a low content of lanthanum (less than 0.6 wt.%) are attractive candidates for high performance anode material for magnesium-based batteries [16].

For the manufacture of anodes, not only the casting method is used, but also printing methods with the integration of laser technologies [17]. So, an anode was made of ink with aluminum nanoparticles (30-40 nm) using squeeze printing. In addition, a laser sintering method was used to

remove the organic solvent from the suspension and increase the conductivity of the printed anode. A Pt/C mixture was chosen as the active material of the cathode electrode, and a KOH based gel electrolyte was also used. This experimental cell at an operating voltage of 0.95 V provided a capacity of 239 mA·h/g and an energy density of 227 mW·h/g.

Now, due to environmental problems in general and the disposal of used batteries in particular, more and more biodegradable materials appear [18]. For example, AZ31 magnesium alloy containing 3% Al and 1% Zn was used as a replacement for pure magnesium, increasing the device life by more than six times, which significantly improved the maximum capacity and energy consumption of the battery, which was 5.2 mA·h and 67 mW respectively, although the area of the anode was a total of 0.8 cm².

2.2. MODERNIZATION OF STRUCTURE AND SURFACE

Anode surface treatment is also one of the promising directions for achieving high discharge characteristics of primary current sources [19]. In one of the studies, carbon materials were applied to the surface of aluminum anodes in order to improve the discharge characteristics of an Al-air battery. NaCl (2M) was used as electrolyte. In the course of research, it was revealed that carbon materials actually increase the values of discharge characteristics. The anodes were made of Al₁₀₈₅ and Al₇₄₇₅ alloys, which demonstrated specific capacities of about 700 mA·h/g and 1200 mA·h/g (at currents of 5 mA/cm² and 10 mA/cm²), respectively. A battery of 4 series-connected cells at a current of 5 mA/cm² had an operating time of 18 hours from a voltage plateau of 2V. This is explained by the fact that a gel consisting of aluminum hydroxide is formed on the surface of untreated aluminum anodes during the discharge process, which prevents diffusion of hydroxyl ions. Carbon materials help to partially prevent the formation of this jelly-like texture.

The reverse situation is also possible – the improvement of carbon anodes with the help of metal alloys. A method for manufacturing flexible graphene batteries containing Ni₅₀Mn₃₅In₁₅ (NiMnIn), Ni₅₀Mn₃₀Ga₂₀ (NiMnGa), and Ni₅₀Mn₄₀Sn₁₀ (NiMnSn) magnetic alloy microparticles is presented. Anodes with magnetic alloy microparticles were treated with phosphoric acid, which leads to the formation of oxides of several metals on the surface of the alloys, which serve as charge accumulation sites. In addition, phosphoric acid has been used instead of lithium salts as an ion source, which allows more defects to form on graphene electrodes, increasing battery capacity. The maximum energy density (343.5 W·h/kg) and capacity (618.4 mA·h/g) were obtained for a battery containing NiMnGa microparticles with the highest porosity. The device voltage was 1.5 V, which is the same as the voltage provided by commercial alkaline primary batteries [20].

Despite the huge number of known galvanic systems and a certain set of metals used, work is constantly being carried out to improve the anode materials. So, batteries based on alkali metals require increased safety during the operation of the system, and for multicomponent systems, due to the diversity of its composition, the issue of effective disposal is relevant.

3. CATHODE

The cathode is the electrode on which the reduction reactions take place - the process of attaching electrons to the atoms of a substance, while its oxidation state decreases. This process is called oxidant reduction. The number of oxidants used in CCS is very large and continues to grow. However, in traditional power supplies with aqueous electrolyte solutions, relatively small amounts of oxidants are used. These are primarily oxides and hydroxides of metals: manganese, lead, nickel, copper, silver, mercury, copper, lead and silver chlorides, as well as atmospheric oxygen. With the advent of CCS with non-aqueous, molten and solid

electrolytes, as well as CCS with new aqueous solutions of electrolytes, the range of oxidants used has significantly expanded. Nowadays, oxides of cobalt, vanadium, chromium, sulfur, thionylchloride, sulfurylchloride, nickel and iron chlorides, iron and copper sulfides, fluorocarbon, bromine, iodine and other oxidizing agents have found application to one degree or another [1].

Work on the study of oxidants continues, and new active substances for cathodes are constantly appearing. In studies devoted to this topic, attention is paid not only to the synthesis of new cathode materials, but also to the mechanism of their destruction and analysis of the characteristics of batteries when using various cathode additives.

3.1. FLUOROCARBON

A number of works are devoted to fluorocarbons CF_x . The advantage of this material is that CF_x batteries are characterized by high energy and specific energy density, as well as a low self-discharge rate and a wide operating temperature range. Currently, research in this direction is mainly associated with various modifications of CF_x .

3.1.1. CF_x IN LITHIUM SYSTEMS

In the case of highly promising lithium systems, it is possible to improve the performance of the Li/CF_x system with the addition of polyaniline [21]. A uniform layer of polyaniline with a thickness of about 160-180 nm, deposited on the surface of the fluorocarbon, leads to an increase in the discharge current of the system. The conductive polyaniline coating provides external bonding between particles, facilitating conduction, resulting in high performance, discharge capacity, discharge voltage and energy density.

To increase the specific energy content of the Li/CF_x system, the CF_x -C cathode material was tested, obtained by adding isophorone diisocyanate, alkylphenolpolyethyleneglycol ester, and polyvinyl alcohol to CF_x , followed by high-speed dispersion, filtration, and

drying [22]. This material has improved electronic conductivity and greater porosity than conventional CF_x .

A strategy for developing a high-performance CF_x cathode using a metal-carbon oxide composite obtained from MOF (metal-organic frameworks) as a starting material is demonstrated. Such samples not only retain the MOF morphology, but also contain a large number of nanopores created during the fluorination process. Due to the advantages of the nanoporous structure, the samples fluorinated at various temperatures show the highest energy density of 2110.7 W·h/kg at a current density of 10 mA/g and the maximum power density of 6540 W/kg at 3000 mA/g. In addition, MOF-based fluorocarbon cathodes have the function of preventing swelling (volumetric expansion is not more than 12%). Moreover, the abundance of structures and low cost of MOFs suggest that it is a promising material for further improvement and popularization of primary Li/CF_x batteries [23].

It is known that the inclusion of a fluorocarbon in the cathode material of a CCS can contribute to a decrease in the self-discharge rate. For example, in primary batteries Li/MnO_2 . The addition of $(CF_x)_n$ to MnO_2 results in improved capacitance and voltage performance [24]. After storage for 60 days at 25°C, the specific capacity of a battery with a cathode made of MnO_2 decreases from 293 mA·h/g to 283 mA·h/g, and the specific capacity when using cathode material $MnO_2-(CF_x)_n$, on the contrary, increases from 312 mA·h/g to 326 mA·h/g. After storage for 30 days at 45°C, the self-discharge rate of batteries with MnO_2 and $MnO_2-(CF_x)_n$ is 9.21% and 1.92%, respectively.

The growth kinetics and orientation of LiF crystals, as the main discharge product of Li/CF_x batteries, are also studied using kinetic models in order to adjust the pore structure of the discharge product layer [25]. These studies may pave the way for the development of a new

electrolyte in the future for high energy density Li/CF_x systems.

3.1.2. CF_x IN NON-LITHIUM SYSTEMS

Typically, fluorocarbons are used in lithium systems. However, their use is also possible in other types of primary CCS. Thus, CF_{0.8} was first demonstrated as a cathode material for magnesium batteries with a high discharge capacity of more than 800 mA·h/g [26]. When using the APC (all-phenyl complex) electrolyte, the cell demonstrates a discharge voltage of 1.23 V and a high discharge capacity – from 813.4 mA·h/g at a discharge to 0.5 V. When LiCl salt is added to the electrolyte, the operating the Mg/CF_{0.8} voltage increases from 1.23 V to 1.6 V.

CF_x can also be used in a sodium anode system. Primary batteries of a new type Na/CF_x have been developed [27]. They are promising for low power applications. For batteries of this type, we studied the effect on the cathode material of carbon nanotubes (CNTs), which were conventional fluorinated CNTs (FCNT-x) and fluorinated graphitized CNTs (FGCNT-x). FGCNT-0.81 material demonstrated very high specific capacities – 798.8 and 751 mA·h/g in lithium and sodium batteries. Besides, the addition of fluorinated graphitized CNTs made it possible to achieve an energy capacity of 2006.6 W/kg in the Li/CF_x system and 1733.4 W/kg in the Na/CF_x system.

3.2. COMPOSITE MATERIALS

A composite material or composite is a multicomponent material made of two or more components with significantly different physical and/or chemical properties, which, in combination, lead to the emergence of a new material with characteristics that differ from the characteristics of the individual components and are not a simple superposition of them. At the same time, individual components remain unchanged in the structure of the composite, distinguishing it from mixtures and solid solutions. It is customary to separate the matrix and filler in the composition of the composite. By varying the composition of the matrix and

filler, their ratio, orientation of the filler, a wide range of materials with the required set of properties is obtained.

The synthesis of composite cathode materials is one of the most commonly used methods for improving the properties of batteries, and for this purpose, the aforementioned fluorocarbons are also used.

3.2.1. LITHIUM SYSTEMS WITH COMPOSITE MATERIALS

Systems with a lithium anode and the use of fluorocarbons as the cathode are of great interest. In order to improve the electronic conductivity of fluorocarbon in the Li/CF_x system, a polythiophene/fluorocarbon (PTh/CF_x (22.94% PTh)) cathode material obtained by insitu polymerization was studied [28]. This material provides 4997 W/kg power density at 4C current, while the maximum power density of a simple CF_x is only 1252 W/kg. A new composite material CF_x-MnO₂ has also been developed [29]. MnO₂ nanowires are synthesized by the hydrothermal method (a method that allows chemical synthesis to be carried out in autoclaves at high temperatures and elevated pressure) on the CF_x surface by insitu polymerization. They intertwine with each other and tightly cover the CF_x surface, forming a three-dimensional conductive framework and improving surface wettability, as well as increasing the capacitance and discharge voltage of Li/CF_x systems.

Also proposed is a solution to the problem of voltage drop at the beginning of the discharge of lithium batteries. Oxygen-containing CF_x was obtained by electrochemical oxidation of graphite in aqueous solution (47%) of hydrofluoric acid at high current densities (200 mA/cm²) [30]. The interlayer distance of such a material was 0.55 nm. The potential profile during the reaction and the X-ray diffraction pattern showed that in the resulting sample, both oxygen and fluorine are bound to each carbon layer. In addition, NMR analysis showed that the oxygen functional groups are uniformly distributed in the obtained samples. The capacity of such material reaches

550 mA·h/g, and the discharge voltage gradually decreases smoothly from an initial mark of 3.4 V.

By creating composites, it is possible to improve sulfur-based cathode materials [31]. Cu_xS was synergistically incorporated into a sulfur cathode in order to improve the specific discharge capacity. A battery with a developed cathode material with a properly selected ratio of sulfur and Cu_xS (40:60) demonstrates a plateau with a long discharge at 2.1 V, improved capacity and energy consumption.

3.3. GRAPHENE

Graphene is increasingly being used to improve the properties of cathode materials. Graphene is a two-dimensional allotropic modification of carbon, formed by a layer of carbon atoms one atom thick. This material has earned special attention to itself for its many useful properties. It conducts heat and electricity perfectly, and is ultra-lightweight and durable at the same time. In addition, graphene is biodegradable and does not pose a threat to the environment [32-47].

3.3.1. GRAPHENE IN LITHIUM SYSTEMS

To increase the energy density and specific energy consumption of Li/CF_x systems, a new hybrid cathode made of fluorine-containing graphene (FG) was proposed [48]. For comparison, two types of FG/S hybrid materials were prepared. In a hybrid cathode of the first type (FG/S-1), a mixture of FG and sublimed sulfur is prepared mechanically using a vortex generator. For the second type (FG/S-2), the melt diffusion method was used, the inclusion of sublimated sulfur in the FG occurred at 155°C for 12 hours in a vessel with argon. For both samples, the sulfur content was 30% of the total mass. Electrochemical tests have shown that hybrid cathodes lead to improved discharge characteristics, including increased specific capacitance and higher discharge voltage. The FG/S-2 cathode has a maximum energy density of 2341 W·h/kg and a maximum specific energy of 13621 W/kg.

The Lithium Thionyl Chloride battery is a promising primary battery due to its highest

theoretical operating voltage (3.6 V), excellent specific energy (up to 590 W/kg) and long operating temperature range [49]. However, disadvantages such as insoluble reaction product (LiCl) and incompletely dissolved sulfur deposited on the electrode can lead to battery failure. Spherical acetylene black is commonly used as the cathode material in this system. Due to its relatively low thermal and electrical conductivity, carbon black char cannot meet performance and safety requirements. The cathode material obtained by assembling acetylene black nanoparticles on graphene nanosheets is intended to improve the discharge characteristics of the system. Acetylene black char nanoparticles are distributed on graphene nanosheets in high concentration and form a micelle-like suprastructure. On the one hand, graphene nanosheets provide excellent mechanical characteristics and high electrical conductivity, as well as prevent the aggregation of acetylene black nanoparticles. On the other hand, the presence of acetylene black char can effectively insulate the graphene nanosheets from refolding and reduce the number of graphene nanosheets. The resulting hybrid of acetylene black char and graphene exhibits excellent discharge characteristics, providing a capacity of up to 1706 mA·h/g at a current density of 5 mA/cm².

3.3.2. GRAPHENE IN NON-LITHIUM SYSTEMS

The use of graphene is also possible in systems with metals other than lithium. Testing of cathode materials Mg/graphite and Mg/graphene was carried out [50]. The cathode material is prepared as follows: take 1 g of MgCl_2 and graphite (graphene), add 200 ml of ethanol to each and stir for 1 hour. Then the MgCl_2 / ethanol and graphite (graphene)/ethanol solutions are stirred for 2 hours. The solution is filtered and dried at 100°C. For comparison of properties, Mg/graphite, Mg/graphene, and a commercial cathode were taken. The conductivity of Mg/graphene (1080 $\mu\text{S}/\text{cm}$) turned out to be noticeably higher than that of Mg/graphite (90

$\mu\text{S}/\text{cm}$) and a commercial cathode ($10 \mu\text{S}/\text{cm}$). All research data show that Mg/graphene can potentially be used as a cathode in magnesium primary CCS.

It is shown that individual graphene monolayers with electrodeposited metals can be used as electrodes for built-in batteries [51]. The anode and cathode were realized by electrodeposition of zinc and copper onto graphene monolayers grown by chemical vapor deposition on a silicon substrate. Cells assembled from the obtained plates achieve capacities up to $15 \mu\text{A}\cdot\text{h}$ at a potential of about 1.1 V and a service life of up to 8 hours. Due to the economical design and simplicity of the presented circuit, such cells can become attractive for use in disposable on-demand power supplies for laboratory research or autonomous sensors.

3.4. ME-AIR

A number of works are devoted to the development and modernization of Me-air batteries. In the Me-air battery, the cathode consists of air and the anode is made of metal. The use of air makes these batteries fundamentally lighter and cheaper, so a lot of research is being done in this direction.

To develop a durable Me-air battery, MnO_2 cathode material was grown on nickel foam using a hydrothermal method [52]. Such unique conditions are used to obtain single crystals and particles of substances that are unstable near the melting point or, under normal conditions, are insoluble in water and other solvents. The foam provides optimum performance due to the balance of hydrophilicity and hydrophobicity. The electrodes synthesized by this method were tested in a primary Zn-air battery. The maximum specific energy density of $95.7 \text{ mW}/\text{cm}^2$ was reached at a discharge voltage of 0.8 V and a current density of $100 \text{ mA}/\text{cm}^2$. A stable discharge is completed in more than 14400 s at a current density of $20 \text{ mA}/\text{cm}^2$. The simplicity of preparation, as well as the high activity and stability of this

new air cathode has great potential for use in Me-air batteries.

As a powder cathode in another promising Me-air battery, MnO_2 was deposited onto a platinum substrate by electrodeposition [53]. At a current density of $330 \text{ mA}/\text{g}$, the cells reach a discharge capacity of $1000 \text{ mA}\cdot\text{h}/\text{g}$ with a specific energy consumption of up to $1890 \text{ mW}\cdot\text{h}/\text{g}$. These results show that the assembled Mn/ MnO_2 battery can occupy an important place in the field of energy storage, its performance is better than that of the classical Zn/ MnO_2 cell.

Also, Me-air batteries use silver electrodes deposited on CFP (Carbon Fiber Paper) to accelerate the oxygen reduction reaction [54]. The synthesis process is shown in the figure (Fig. 1). A battery assembled from Ag/CFP exhibits a discharge current density of more than $100 \text{ mA}/\text{cm}^2$ with an excellent specific energy density of $109.5 \text{ mW}/\text{cm}^2$, a high specific capacity of $2783.5 \text{ mA}\cdot\text{h}/\text{g}$ and a specific energy density of $4342.3 \text{ W}\cdot\text{h}/\text{kg}$.

Air batteries are usually made of hard and heavy materials such as metal or plastic, while a voluminous electrolyte solution in static or circulating mode is required to ensure their stable operation. Thus, they are less suitable for powering flexible and portable devices with lower power consumption. To solve this problem, a flexible and lightweight Al-air battery with low electrolyte content, which is made entirely on cellulose paper, has been developed [55]. The aluminum foil anode is embedded in the paper substrate during the papermaking process, while the breathable cathode is deposited on the

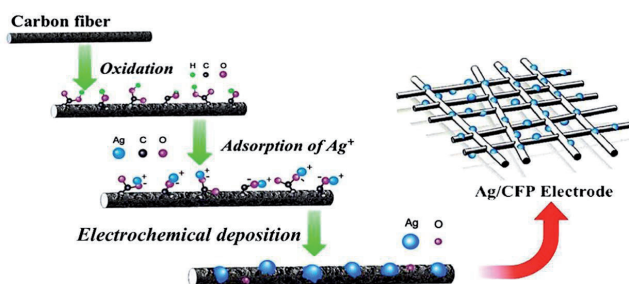


Fig. 1. Ag/CFP electrode fabrication.

surface of the paper using oxygen reduction ink. Despite its simple structure and low cost, this Al-air battery can provide a satisfactory specific energy density of 19 mW/cm², and its service life is 58 hours. The corresponding specific capacity is 2338 mA·h/g. In addition, the battery exhibits excellent flexibility.

3.5. ECO-FRIENDLY CATHODE MATERIALS

Increasingly, the works are investigating the possibility of making batteries from materials that are safe for the environment. The Fe/2,3-dichloro-5,6-dicyano-1,4-benzoquinone (Fe-DDQ) primary CCS operated in pure methanesulfonic acid (MSA) was investigated [56]. Because it uses a large amount of iron and renewable materials such as DDQ and MSA, it is expected to be a cost-effective, single-use power system. Stainless steel (SS-304) is used as the iron source (anode) and the DDQ in MSA is used as the cathode. The Fe-DDQ battery is environmentally friendly, inexpensive and renewable. The operating voltage of the cell is 1.1 V, the maximum current density is 2 mA/cm², and the specific energy density is ~ 1.2 mW/cm².

A new chemistry is reported for an organic lithium primary battery that works by synergistically reducing 9,10-anthraquinone (AQ) and fluoroethylene carbonate (FEC) [57]. In the presence of FEC, the balance between the carbonyl and enol structures is disturbed and replaced by an irreversible process with the formation of methylene and inorganic salts (such as LiF, Li₂CO₃) as products. This irreversible AQ chemistry produces a high energy density of 1300 W·h/kg with a stable discharge voltage of 2.4 V, a wide operating temperature range (-40 to 40°C) and a low self-discharge rate. Combined with the advantages of low toxicity, simplicity and variety of synthesis methods, and readily available AQ, the chemistry of lithium organic batteries promises to be a new candidate for applications requiring low cost, high environmental friendliness and energy density.

Analysis of works focused on studies of cathode materials in primary CCS suggests that in this direction mainly work is being done on the synthesis of new cathode materials, and the most popular of them are graphite-containing materials. Also, great attention is paid to environmental friendliness, in particular, replacing lithium with safer metals. It should be noted that in spite of this, the highest discharge voltages and capacitance indices are achieved precisely on primary lithium CCS. They are trying to compete with Me-air systems; in such systems, high capacitance values are observed, but still low discharge voltages.

4. ELECTROLYTE

Electrolytes are substances that conduct electric current due to dissociation into ions in melts or solutions. These can be acids and bases, salts, some crystalline bodies (silver iodide, zirconium dioxide, etc.). All electrolytes can be divided into aqueous and non-aqueous; solid-phase electrolytes are isolated separately, the conductivity of which is justified by the movement of ions in crystal lattices.

4.1. IONIC LIQUIDS

Ionic liquids are examples of non-aqueous electrolytes. Ionic liquids – low-temperature molten salts with bulky cations and anions - are widely used as polar solvents and catalysts. Since they consist of "free" charge carriers, their use is especially in demand in the development of CCS. Ionic liquids have electrochemical stability, relatively high electrical conductivity and virtually no saturated vapor pressure.

Currently, work is being actively carried out in the direction of modernizing the chemical composition of electrolytes based on ionic liquids to improve the discharge characteristics of primary CCS. Using the example of an Al-air system with 1-ethyl-3-methylimidazolium oligofluorohydrogenate, the advantages of which are ultra-high conductivity, low viscosity and chemical stability in contact with oxygen and water, it was shown as an electrolyte that

practical results differ markedly from theoretical calculations [58]. In theory, such cells should have a capacity of about 227 mA·h, which is equivalent to 200 mAh/cm²; in practice, it was possible to obtain 70% of the theoretical calculations – up to 160 mA·h, which is equivalent to 140 mA·h/cm². Analysis of the battery components after complete discharge of the cell showed the presence of Al₂O₃ on the air cathode and active dissolution on the surface of the aluminum anode. To solve this problem, it was proposed to use ionic liquid electrolytes with tetrabutylammonium dihydrofluoride (TBAH₂F₃) in the Al-air system [59]. Due to the formation of a protective layer of Al_xO_yF_z on the aluminum surface, the formation of an oxide film is prevented and thus higher discharge values are ensured due to the more active surface.

4.2. POLYMER ELECTROLYTES

There is now a worldwide need to develop sustainable, safe and clean energy resources. One of the key directions for the implementation of this requirement is the development of new solid polymer electrolytes, which allow avoiding the leakage and release of toxic compounds during the operation of CCS. Systems based on biodegradable electrolytes are used in the medical field for electrical stimulation of tissue regeneration, in the environmental field to minimize environmental pollution.

Solid electrolytes are thin conductive membranes with a thickness of about 100-200 microns, obtained by mixing solutions of salts or acids and their subsequent drying [60-62]. The choice of the optimal composition of electrolytes is carried out after studying the energy characteristics of membranes obtained from solutions with different concentrations of precursors.

Due to the presence of high ionic reducibility, good biocompatibility, and a wide window of electrochemical potential, a promising material is a polymer electrolyte based on silk fibroin with choline nitrate (SF-[Ch][NO₃]) [63]. In

an experimental cell, such an electrolyte is a conductive membrane that allows the battery to operate for 45 days from a voltage plateau of about 1.03 V.

Polysaccharides are widely used biopolymers with properties suitable for the manufacture of high-performance polymer electrolytes. In particular, algae-based polysaccharides are promising environmentally friendly and biodegradable alternatives to conventional polyelectrolytes. Algae-based polysaccharides meet the key requirements for high performance polymer electrolytes – dominant amorphous phase, solubility, and the ability to form cross-linked networks with additives that improve ionic conductivity. Many of the optimized polymer electrolytes far exceeded the minimum ionic conductivity of electrolytes of 1 mS/cm. In addition, the mechanical properties of the algae-based hydrogel allow the creation of fully personalized wearable and biocompatible devices [64].

4.3. WATER ELECTROLYTES

Water electrolytes, that is, aqueous solutions of salts capable of dissociation into ions, are used quite widely in the creation of CCS. Despite the great popularity of non-aqueous electrolytes and the growing interest in polymer electrolytes, work in the field of aqueous electrolytes is still ongoing.

Changes in the energy parameters of systems with aqueous electrolytes can be achieved by introducing complexing elements [65]. The effect of adding two strong complexing agents at different concentrations to the aqueous electrolyte of a Mg-air battery was investigated. At the first stage, several organic complexing agents with different ability to form complexes Fe³⁺ and Mg²⁺ were investigated in order to assess their influence on the discharge behavior of the anode (pure magnesium). In the course of this study, nitrilotriacetic acid and tyrosine were chosen as complexing agents. The results obtained during the discharge of the cells indicate that the addition of tyrosine and

nitrilotriacetic acid to the electrolyte of a water-based Mg-air battery improves the discharge potential of the battery at concentrations in the ranges of 0.1-0.001 M and 0.1-0.01 M. The maximum improvement in potential during a discharge for 24 h, obtained in these two cases, was about 210 mV and 200 mV, respectively. The results allow us to conclude that strong complexing agents in the composition of an aqueous electrolyte are able to effectively activate the anode and provide a higher discharge potential.

The electrolyte plays an important role in primary CCS, often determining the shape of the entire battery. The realization of the potential of the cathode and anode materials depends on his choice, which is confirmed by continuous research in this area. Striving for environmental friendliness, safety in use and high compatibility with a wide variety of devices, solid materials and biological media are increasingly used as electrolytes.

5. CONCLUSION

Chemical power sources have firmly established their position in modern life. At first glance, the appearance of accumulators and fuel cells should have stopped the development of primary CCS, however, a review of research work only in recent years suggests that primary batteries continue to be improved. The need for energy sources that satisfy a limited set of requirements allowed primary batteries to consolidate their niche in the world market and not give up their positions. Continuing competition motivates to look for ways to get rid of the known shortcomings of primary CCS and to expand the boundaries of their capabilities. In addition to the materials for cathodes and anodes described in this article, as well as electrolytes, attention is drawn to other battery elements. Being sought and new methods of research and new fields of application. Sharper raises the question of recycling; it is logical that it leads to attempts to create more environmentally batteries.

A large number of studies devoted to primary CCS indicates not only how much has been done, but also what remains to be done. All the difficulties and unexpected discoveries open up opportunities for the implementation of new ideas. And these possibilities are, perhaps, endless.

REFERENCES

1. Korovin NV, Skundin AM. *Khimicheskie istochniki toka: Spravochnik* [Chemical current sources: A handbook]. Moscow, MPEI Publ., 2003, 740 p.
2. Reddy T. *Linden's Handbook of Batteries, Fourth Edition*. McGraw-Hill Education, 2010, 1456 p.
3. Garche J, Dyer C, Moseley PT, Ogumi Z, Rand DAJ, Scrosati B. *Encyclopedia of Electrochemical Power Sources, First edition*. Elsevier Science, 2009, 4538 p.
4. Crompton TR. *Battery Reference Book, Third Edition*. Newnes, 2000, 800 p.
5. Garche J, Brandt K. *Electrochemical Power Sources: Fundamentals, Systems, and Applications*. Elsevier, 2018, 670 p.
6. Broussely M, Pistoia G. *Industrial Applications of Batteries. From Cars to Aerospace and Energy Storage*. Elsevier, 2007, 792 p.
7. Cleveland CJ, Morris C. *Dictionary of Energy, Second Edition*. Elsevier, 2014, 700 p.
8. Barak M. *Electrochemical Power Sources: Primary and secondary batteries*. The Institution of Engineering and Technology Publ., 1980, 512 p.
9. Varypaev VN, Dasoyan MA, Nikolsky VA. *Khimicheskie istochniki toka* [Chemical current sources]. Moscow, Higher School Publ., 1990, 240 p.
10. Pistoia G. *Batteries for Portable Devices, First Edition*. Elsevier Science, 2005, 309 p.
11. Kedrinsky IA, Dmitrenko VE, Grudyanov II. *Litievye istochniki toka* [Lithium current sources]. Moscow, Energoatomizdat Publ., 1992, 240 p.
12. Liu X, Liu S, Xue J. Discharge performance of the magnesium anodes with different

- phase constitutions for Mg-air batteries. *Journal of Power Sources*, 2018, 396:667-674.
13. Xiong H, Yu K, Yin X, Dai Y, Yan Y, Zhu H. Effects of microstructure on the electrochemical discharge behavior of Mg-6wt%Al-1wt%Sn alloy as anode for Mg-air primary battery. *Alloys and Compounds*, 2017, 708:652-661.
 14. Li Z, Wang H, Li J, Zhuang Y, Gao J, Li H, Cheng W. Synergistic effect of second phase and grain size on electrochemical discharge performance of extruded Mg-9Al_xIn alloys as anodes for Mg-air battery. *Advanced Engineering Materials*, 2020, 22(3):1-10.
 15. Xiong H, Li L, Zhang Y, Yu K, Fang H, Dai Y, Dai H. Microstructure and discharge behavior of Mg-Al-Sn-In anode alloys. *The Electrochemical Society*, 2017, 164:1745-1754.
 16. Song Y, Yang H, Chai Y, Wang Q, Jiang B, Wu L, Zou Q, Huang G, Pan F, Atrens A. Corrosion and discharge behavior of Mg-xLa alloys (x=0.0-0.8) as anode materials. *Trans. Nonferrous Met. Soc. China*, 2021, 31:1979-1992.
 17. Yu Y, Chen M, Wang S, Hill C, Joshi P, Hu A. Laser sintering of Al nanoparticles for Al-air batteries. *Laser Applications*, 2018, 3:1-5.
 18. Edupuganti V, Solanki R. Fabrication, characterization, and modeling of a biodegradable battery for transient electronics. *Power Sources*, 2016, 336:447-454.
 19. Pino M, Herranz D, Chacon J, Fatas E, Ocon P. Carbon treated commercial aluminium alloys as anodes for aluminium-air batteries in sodium chloride electrolyte. *Power Sources*, 2016, 326:296-302.
 20. Lopez-Medina M, Hernandez-Navarro F, Martinez AI, Oliva AI, Rodriguez-Gonzalez V, Camarillo-Garcia JP, Aguilar-Ortiz CO, Flores-Zuñiga H, Oliva J. Enhancing the capacity and discharge times of flexible graphene batteries by decorating their anodes with magnetic alloys NiMnM_x (M_x=Ga, In, Sn). *Materials Chemistry and Physics*, 2020, 256:1-12.
 21. Li L, Zhu L, Pan Y, Lei W, Ma Z, Li Z, Cheng J, Zhou J. Integrated Polyaniline-coated CF_x Cathode Materials with Enhanced Electrochemical Capabilities for Li/CF_x Primary Battery. *International Journal of Electrochemical Science*, 2016, 11:6838-6847.
 22. Zhu L, Pan Y, Li L, Zhou J, Lei W, Deng J, Ma Z. Preparation of CF_x@C Microcapsules as a High-rate Capability Cathode of Lithium Primary Battery. *International Journal of Electrochemical Science*, 2016, 11:14-22.
 23. Li X, Zhang H, Liu C, Qiao J, Zhou X. A MOF-derived multifunctional nano-porous fluorinated carbon for high performance lithium/fluorinated carbon primary batteries. *Microporous and Mesoporous Materials*, 2021, 310:1-8.
 24. Chang Y, Wang M, Wang S, Na J, Bund A, Nanjundan AK, Yamauchi Y. Ultralong storage life of Li/MnO₂ primary batteries using MnO₂-(CF_x)_n with CeF semi-ionic bond as cathode materials. *Electrochimica Acta*, 2019, 320:1-9.
 25. Long S, Chen F, Ding F, Han Y, Liu X, Xu Q. Study on Crystal Growth Kinetics and Preferred Orientation for LiF Crystal in Dimethyl Sulfoxide/1,3-dioxolane Based Electrolyte. *The Journal of Physical Chemistry*, 2019, 123(46):28048-28057.
 26. Miao X, Yang J, Pan W, Yuan H, Nuli Y, Hirano S. Graphite fluoride as a cathode material for primary magnesium batteries with high energy density. *Electrochimica Acta*, 2016, 210:704-711.
 27. Li Y, Wu X, Liu C, Wang S, Zhou P, Zhou T, Miao Z, Xing W, Zhuo S, Zhou J. Fluorinated multi-walled carbon nanotubes as cathode materials of lithium and sodium primary batteries: effect of graphitization of carbon nanotubes. *Journal of Materials Chemistry A*, 2019, 7:7128-7137.

28. Yina X, Lia Y, Fenga Y, Fenga W. Polythiophene/graphite fluoride composites cathode for high power and energy densities lithium primary batteries. *Synthetic Metals*, 2016, 220:560-566.
29. Luo Z, Wan J, Lei W, Zhao Y, Pan Y, Ma Z. A simple strategy to synthesis CF_x@MnO₂-nanowires composite cathode materials for high energy density and high power density primary lithium batteries. *Materials Technology*, 2018, 35(13-14):836-842.
30. Matsuo Y, Hirata S, Dubois M. Electrochemical oxidation of graphite in aqueous hydrofluoric acid solution at high current densities. *Journal of Fluorine Chemistry*, 2016, 185:36-41.
31. Cheng JJ, Liu LF, Ou SW, Ou Y, Liu Q, Song HJ, Pan Y. Sulfur/Cu_xS hybrid material for Li/S primary battery with improved discharge capacity. *Materials Chemistry and Physics*, 2019, 224:384-388.
32. Lakra R, Kumar R, Sahoo PK, Thatoi D, Soam A. A mini-review: Graphene based composites for supercapacitor application. *Inorganic Chemistry Communications*, 2021, 133:1-10.
33. Wang Y, Caob H, Chena C, Xieb Y, Sunc H, Duand X, Wang S. Metal-free catalytic ozonation on surface-engineered graphene: Microwave reduction and heteroatom doping. *Chemical Engineering Journal*, 2019, 355:118-129.
34. Wang X, Niandong J, Tung S, Liu L. Photoresponsive graphene composite bilayer actuator for soft robots. *ACS applied materials & interfaces*, 2019, 11(33):30290-30299.
35. Cheng H, Huang Y, Shi G, Jiang L, Qu L. Graphene-based functional architectures: sheets regulation and macrostructure construction toward actuators and power generators. *Accounts of chemical research*, 2017, 50(7):1663-1671.
36. Jin X, Feng C, Ponnamma D, Yi Z, Parameswaranpillai J, Thomas S, Salim N. Review on exploration of graphene in the design and engineering of smart sensors, actuators and soft robotics. *Chemical Engineering Journal Advances*, 2020, 4:1-66.
37. Pierrata P, Gaumet JJ. Graphene quantum dots: Emerging organic materials with remarkable and tunable luminescence features. *Tetrahedron Letters*, 2020, 61(49):1-9.
38. Mudusu D, Nandanapalli KR, Lee S, Hahn YB. Recent advances in graphene monolayers growth and their biological applications: A review. *Advances in Colloid and Interface Science*, 2020, 283:1-18.
39. Tran TS, Dutta NK, Choudhury NR. Graphene inks for printed flexible electronics: graphene dispersions, ink formulations, printing techniques and applications. *Adv Colloid Interf.*, 2018, 261:41-61.
40. Shen C, Oyadiji SO. The Processing and Analysis of Graphene and the Strength Enhancement Effect of Graphene-based Filler Materials: A Review. *Materials Today Physics*, 2020, 15:1-27.
41. Wang Q, Qi G, Wang Y, Zheng H, Shan S, Lu C. Research progress on the effect of graphene oxide on the properties of cement-based composites. *New Carbon Materials*, 2021, 36(4):729-750.
42. Petukhov DI, Kapitanova OO, Eremina EA, Goodilin EA. (2021). Preparation, chemical features, structure and applications of membrane materials based on graphene oxide. *Mendeleev Communications*, 2021, 31(2):137-148.
43. Farjadian F, Abbaspour S, Sadatlu MAA, Mirkiani S, Ghasemi A, Hoseini-Ghahfarokhi M, Mozaffari N, Karimi M, Hamblin MR. Recent Developments in Graphene and Graphene Oxide: Properties, Synthesis, and Modifications: A Review. *Chemistry Select*, 2020, 5(33):10200-10219.
44. Joshi DJ, Koduru JR, Malek NI, Hussain CM, Kailasa SK. Surface modifications and analytical applications of graphene oxide: A

- review. *TrAC Trends in Analytical Chemistry*, 2021, 144:1-15.
45. Dramou P, Dahn SL, Wang F, Sun Y, Song Z, Liu H, He H. Current review about design's impact on analytical achievements of magnetic graphene oxide nanocomposites. *TrAC Trends in Analytical Chemistry*, 2021, 137:1-17.
46. Nebol'sin VA, Galstyan V, Silina YE. Graphene oxide and its chemical nature: Multi-stage interactions between the oxygen and graphene. *Surfaces and Interfaces*, 2020, 21:1-70.
47. Alemi F, Zarezadeh R, Sadigh AR, Hamishehkar H, Rahimi M, Majidinia M, Rashtchizadeh N. Graphene Oxide and Reduced Graphene Oxide: Efficient Cargo Platforms for Cancer Theranostics. *Journal of Drug Delivery Science and Technology*, 2020, 60:1-15.
48. Zhang J, Zhou H, Zhu H, Hu P, Hang C, Yang J, Peng T, Mu S, Huang Y. Fluorinated graphene/sulfur hybrid cathode for high energy and high power density lithium primary batteries. *RSC Adv.*, 2018, 8:12701-12707.
49. Wei JH. Acetylene Black Loaded on Graphene as a Cathode Material for Boosting the Discharging Performance of Li/SOCl₂ Battery. *International Journal of Electrochemical Science*, 2017, 12:898-905.
50. Simanjuntak C, Siburian R, Marpaung H, Tamrin. Properties of Mg/graphite and Mg/graphene as cathode electrode on primary cell battery. *Heliyon*, 2020, 6:1-6.
51. Iost RM, Crespilho FN, Kern K, Balasubramanian K. A primary battery-on-a-chip using monolayer graphene. *Nanotechnology*, 2016, 27:1-8.
52. Xu K, Loh A, Wang B, Li X. Enhancement of Oxygen Transfer by Design Nickel Foam Electrode for Zinc-Air Battery. *Journal of The Electrochemical Society*, 2018, 165:809-818.
53. Moulai F, Messaoudi B, Zerroual L, Hadjersi T, Achour A. Assembled manganese and its nanostructured manganese dioxide rich electrodes. *Materials Chemistry and Physics*, 2020, 244:1-27.
54. Hong Q, Lu H. In-situ Electrodeposition of Highly Active Silver Catalyst on Carbon Fiber Papers as Binder Free Cathodes for Aluminum-air Battery. *Scientific Reports*, 2017, 7:1-12.
55. Wang Y, Kwok HYH, Pan W, Zhang Y, Zhang H, Lu X, Leung DYC. Combining Al-air battery with paper-making industry, a novel type of flexible primary battery technology. *Electrochimica Acta*, 2019, 319:947-957.
56. Ramavath JN, Ramachandra C, Ramanujam K. Iron-Dicyano Dichloro Quinone Primary Battery. *Chemistry Select*, 2018, 3:10281-10286.
57. Sun P, Bai P, Chen Z, Su H, Yang J, Xu K, Xu Y. A Lithium-Organic Primary Battery. *Small*, 2019, 16(3):1-6.
58. Gelman D, Shvartsev B, Ein-Eli Y. Aluminum-air battery based on an ionic liquid electrolyte. *Materials Chemistry A*, 2014, 2(47):1-8.
59. Levy NR, Lifshits S, Yohanan E, Ein-Eli Y. Hybrid ionic liquid propylene carbonate-based electrolytes for aluminum-air batteries. *ACS Applied Energy Materials*, 2020, 3(3):2585-2592.
60. Perumal P, Abhilash KP, Sivaraj P, Selvin PC. Study on Mg-ion conducting solid biopolymer electrolytes based on tamarind seed polysaccharide for magnesium ion batteries. *Materials Research Bulletin*, 2019, 118:1-11.
61. Mahalakshmi M, Selvanayagam S, Selvasekarapandian S, Moniha V, Manjuladevi R, Sangeetha P. Characterization of biopolymer electrolytes based on cellulose acetate with magnesium perchlorate (Mg(ClO₄)₂) for energy storage devices. *Advanced Materials and Devices*, 2019, 4:276-284.

62. Monisha S, Mathavan T, Selvasekarapandian S, Benial AMF, Prema latha M. Preparation and characterization of cellulose acetate and lithium nitrate for advanced electrochemical devices. *Ionics*, 2017, 23:2697–2706.
63. Jia X, Wang C, Ranganathan V, Napier B, Yu C, Chao Y, Forsyth M, Omenetto FG, MacFarlane DR, Wallace GG. A biodegradable thin-film magnesium primary battery using silk fibroin-ionic liquid polymer electrolyte. *ACS Energy Letters*, 2017, 2:831–836.
64. Torres FG, De-la-Torre GE. Algal-based polysaccharides as polymer electrolytes in modern electrochemical energy conversion and storage systems: A review. *Carbohydrate Polymer Technologies and Applications*, 2021, 2:1-17.
65. Vaghefnazari B, Hoche D, Lamaka SV, Snihirova D, Zheludkevich ML. Tailoring the Mg-air primary battery performance using strong complexing agents as electrolyte additives. *Journal of Power Sources*, 2020, 453:1-11.

DOI: 10.17725/rensit.2022.14.143

Obtaining Ink Based on Palladium Nanoparticles for Possible Use in Printed Electronics

¹Ekaterina G. Rustamova, ¹Maria S. Kagirina, ^{1,2}Sergey P. Gubin

¹Scientific production company “Grafenika”, <https://www.grafenika.ru/>

Moscow 107143, Russian Federation

²Kurnakov Institute of General and Inorganic Chemistry of RAS, <http://www.igic.ras.ru/>

Moscow 119991, Russian Federation

E-mail: nebukina@yandex.ru, mariakagirina@rambler.ru, gubin@igic.ras.ru

Received March 22, 2022, peer-reviewed March 29, 2022, accepted April 5, 2022

Abstract: The possibility of obtaining conductive ink based on palladium nanoparticles obtained by the polyol method is considered. The composition of the ink is adapted for use in printed electronics. The ink contains 20 mass% palladium, has a viscosity of 17-20 cps and a surface tension of 35-38 N/m. During heat treatment, the specific surface resistance of palladium nanostructures changes from 0.38 to 0.07 Ω . These and other characteristics, such as high stability and good wettability of the substrate, make it possible to use palladium nanoink in printer printing.

Keywords: synthesis, palladium nanoparticles, nanoink, printed electronics

UDC 54.05'06

Acknowledgements: The work was supported by the Ministry of Education and Science of Russia within the framework of the state task of the Kurnakov Institute of General and Inorganic Chemistry of the Russian Academy of Sciences. The authors of this work express their gratitude to the Educational and Methodological Center for Lithography and Microscopy of Lomonosov Moscow State University for their help in the study of palladium nanoparticles using SEM equipment.

For citation: Ekaterina G. Rustamova, Maria S. Kagirina, Sergey P. Gubin. Obtaining Ink Based on Palladium Nanoparticles for Possible Use in Printed Electronics. *RENSIT: Radioelectronics. Nanosystems. Information Technologies*, 2022, 14(2):143-150e. DOI: 10.17725/rensit.2022.14.143.

CONTENTS

1. INTRODUCTION (143)

2. EXPERIMENTAL PART(144)

3. RESULTS AND DISCUSSION (145)

4. CONCLUSION (148)

REFERENCES (149)

1. INTRODUCTION

Printer technologies are of increasing interest for the production of electronic

devices such as gas sensors [1], transistors [2], organic light-emitting diodes [3], RFID tags [4], etc. Conductive inks are one of the important components of printing. The inks can be based on various materials such as conductive polymers [5], carbon [6], organometallic compounds and metallic nanoparticles [7]. The leading place among conductive inks is occupied by systems based on metallic nanoparticles. The reason is that their resistivity is close

to the specific gravity of the material (2-3 times higher) and much lower than that of conductive polymers and other materials. Silver nano-ink is most commonly used in printer printing. Silver has undeniable advantages in terms of electrical and thermal conductivity, oxidation resistance, optical and antibacterial properties. We have previously reported on the possibility of using silver nanoparticles in input-organic solvents in 2D printing [8]. However, silver is not without disadvantages: metal atoms can diffuse inside the dielectric under conditions of high humidity, tend to form dark Ag_2S films, which limits the use of silver near sulfur-containing materials (rubber). Therefore, the creation of nano-ink based on nanoparticles of other precious metals is important.

It is known that platinum group metals exhibit chemical inertness with respect to atmospheric constituents, which makes them indispensable for the manufacture of electronic devices.

Palladium is a unique element of the platinum group. The element is widely used in the manufacture of capacitors, some types of relays, contacts, parts of microcircuits. Palladium, having good anti-corrosive properties, improves stability of functioning of parts in any environment, including at significant temperature increase. Palladium is most actively used in electronic, chemical, military and aerospace industries. Scientists are conducting scientific research to expand the use of this precious metal [9]. Palladium nanoparticles are used in the form of dispersions in liquid phases or fixed on the surface of various substrates [11].

The production of palladium nanoparticles and materials based on them still remains interesting and significant. Therefore, the main goal of this work was to synthesize and study the properties of palladium nanoparticles, as well as to produce inks based on them for possible use in printer technology printing.

2. EXPERIMENTAL PART

The following materials were used for the experimental work: palladium chloride (crude, JSC "Aurat"), sodium hydroxide (crude, LLC "RusChem"), polyvinylpyrrolidone (CAS-No: 9003-39-8 (K15), AppliChem), ethylene glycol (h.d, "ECOS-1"), acetone (h.d.a., RusChem LLC), ethanol (hh, "CONSTANT PHARM-M" LLC), deionized water (resistivity is 18 Mohm-cm).

Synthesis of palladium nanoparticles was carried out in an oil bath in a three-neck flask equipped with a reflux condenser, under continuous stirring with a magnetic stirrer. Ethylene glycol, a stabilizer –polyvinylpyrrolidone and a small amount of sodium hydroxide (to create a slightly alkaline environment) were placed in the reaction vessel, then stirred and heated. When the temperature reached 120°C , an aqueous solution of palladium chloride was slowly (drop by drop) introduced into the system. After all precursor solution was added, the reaction mixture was heated to 160°C and kept under stirring for 3 h. During the reaction, a color change from burgundy to black was observed, indicating the formation of palladium nanoparticles.

At the end of the synthesis, the palladium nanoparticles were precipitated by triple excess of acetone by centrifugation for

5 min at a rotor speed of 7000 rpm. The resulting precipitate was decanted and washed several times with ethanol to remove reaction products and excess stabilizer.

In order to obtain ink, the impurity-free nanoparticles were ultrasonically redispersed in a mixture of ethylene glycol and ethyl alcohol, taken in a ratio of 4:1, respectively.

The obtained palladium nanoparticles were applied to glass substrates by spin-coating. The obtained films were annealed at 150°, 200°, 250° and 300°C.

Microphotographs in the mode of scanning electron microscopy were obtained on a Zeiss Supra 40 Scanning Electron Microscope with Field Emission cathode with an operating accelerating voltage of 25 kV. The morphology of the samples was determined in the secondary electron detector mode (In-lens SE). Sample preparation consisted of applying a dispersion sample of palladium nanoparticles with a pipette to a silicon substrate, which after complete drying of the preparation was placed in the microscope.

Absorption spectra of the samples were obtained using a spectrophotometer Leki SS2107UV (CJSC LOIP, Russia) in the wavelength range from 200 to 1100 nm. Working samples were prepared by 30-fold dilution of the reaction mass (or dispersion of palladium nanoparticles) with deionized water. The sample volume was 3 ml and the optical path length was 1 cm.

X-ray phase analysis (XRF) was carried out on a DRON-7 setup with a graphite monochromator on $\text{CuK}\alpha$ – radiation ($\lambda = 1.54056 \text{ \AA}$) with Ni filters.

The concentration of palladium nanoparticles in the nanoink was determined gravimetrically.

The viscosity of palladium nanoink was measured on an AND SV 10A vibrating viscometer.

The surface tension of palladium nanoink was determined by stalagmometry.

To measure the sheet resistance of palladium thin films, a four-probe method was used. The value of sheet resistance was calculated by the formula:

$$R_s = F \cdot U / I,$$

where R_s – value of Ohm; F – correction factor $F = \pi / \ln 2 = 4.53236$; U – value of electric voltage, V ; I – value of electric current, A .

3. RESULTS AND DISCUSSION

Palladium nanoparticles were produced using the polyol method. Simultaneously ethylene glycol, was used as the reaction medium and reducing agent. At the beginning of the synthesis, polyvinylpyrrolidone (PVP), used as a stabilizer, due to the presence of heterocyclic pyrrolidol groups in the structure, entered into donor-acceptor interaction with the noble metal ions, forming complex PVP-Pd^{2+} . According to the literature, the formation of a metal-polymer complex is the result of contact between one palladium ion and three monolinks of the polymer ligand [12]. Thus, palladium ions were coordinated to the polymer molecules prior to the reduction reaction. When heated, ethylene glycol was oxidized to glycolic acid. Glycolic acid was deprotonated in the reaction medium, forming glycolate anions. Receiving electrons from the oxidation products of the polyalcohol, the

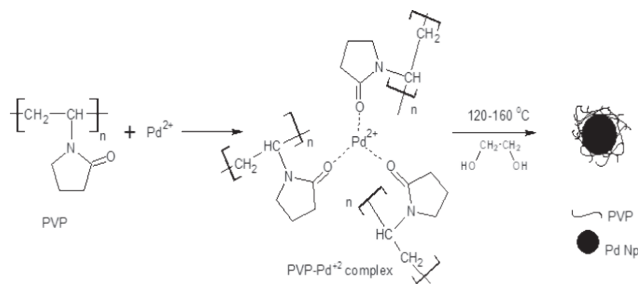


Fig. 1. Mechanism of formation of palladium nanoparticles.

polymer-ion complexes were reduced to form metal colloids.

In the process of synthesis, carbonyl C=O groups of polyvinylpyrrolidone side chains began to actively interact with the surface of the formed nanoparticles, thereby slowing down their further growth and providing the stabilization process. **Fig. 1** shows the mechanism of palladium nanoparticles formation.

The process of nanoparticle formation was monitored using UV spectroscopy. In the absorption spectrum (**Fig. 2**) recorded at the initial stage of synthesis, there is a peak in the near ultraviolet region (271 nm) corresponding to the PVP-Pd²⁺ complex.

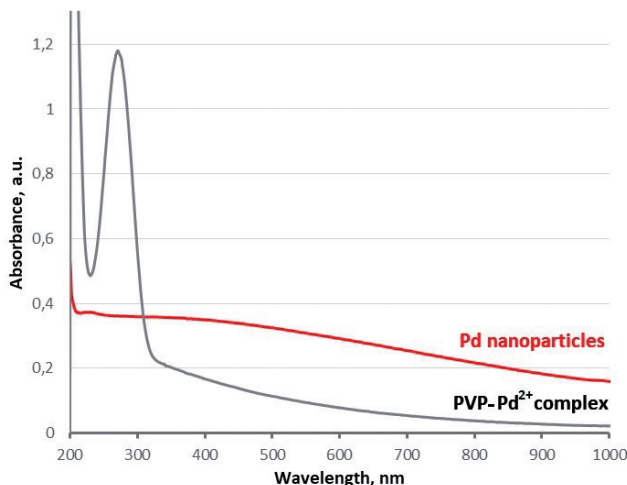


Fig. 2. UV-visible absorption spectrum of palladium nanoparticles.

In the process of PVP-Pd²⁺ complexes reduction, the peak began to flatten out and at the end of the synthesis, the spectrum acquired a wide absorption region falling smoothly into the visible region, which is characteristic of metallic palladium nanoparticles.

The study by scanning electron microscopy made it possible to establish the morphology of the obtained nanoparticles. Small and large spherical particles are present in nano-ink (**Fig. 3**). Large palladium particles have a pronounced multifaceted crystalline structure, in turn, small particles are

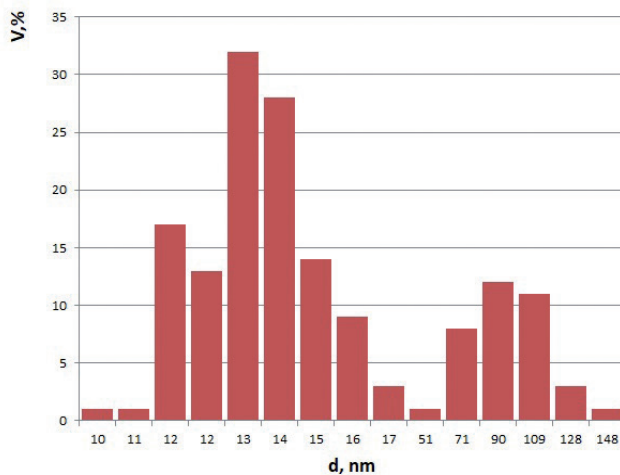
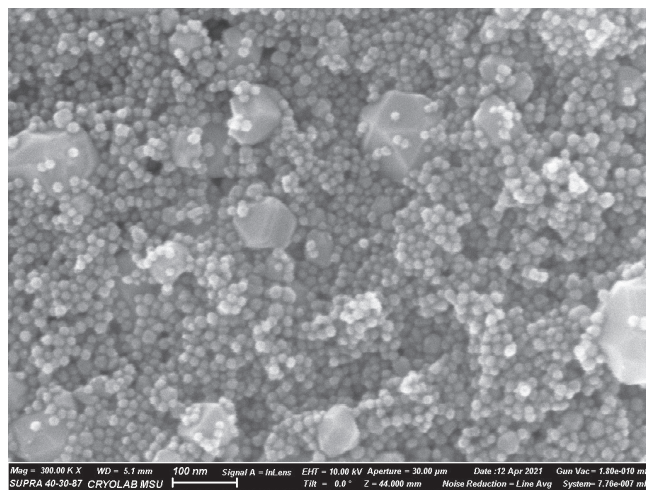


Fig. 3. SEM-image of palladium nanoparticles and histogram of nanoparticles size distribution.

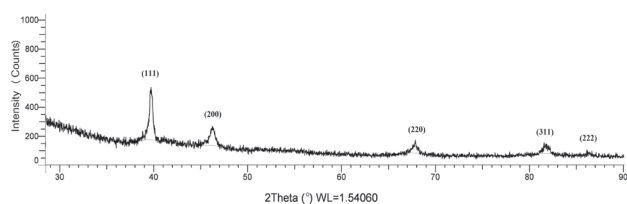


Fig. 4. XRD of palladium nanoparticles.

characterized by a smoother surface relief. Results of analytical processing of SEM images allowed making a conclusion about bimodal character of nanoparticles distribution. The dominant maximum in particle content in the sample belongs to palladium nanoparticles with the average size of 13 nm. The average size of large particles was 90 nm.

Identification of the phase composition of the obtained nanoparticles was carried out based on the XRD. The diffractogram (Fig. 4) shows reflexes in the region of reflection angles $2\theta = 40, 46, 68, 82, \text{ and } 87$ deg corresponding to the palladium phase with cubic crystal structure (JCPDS 05-0681). The low intensity and broadened nature of the coherent scattering regions indicate the nanoscale nature of the particles under study.

In order to investigate the temperature treatment behavior of palladium nanoparticles the films were obtained from the ink and annealed at 150-300°C.

SEM microphotographs (Fig. 5a,b) show that nanoparticles at 150°C-200°C

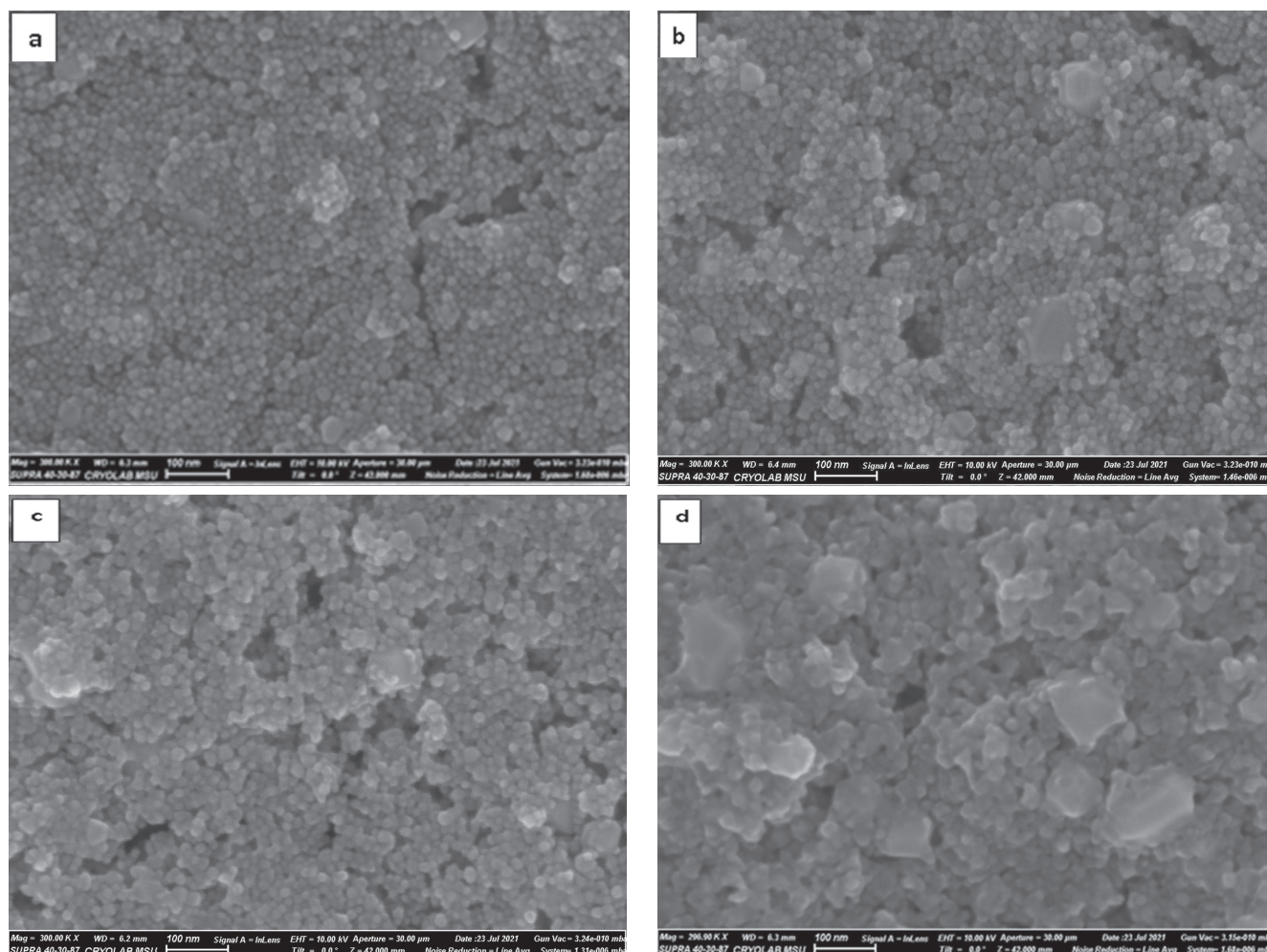


Fig. 5. SEM images of annealed palladium nanoparticles at the following temperatures: a – 150°C, b – 200°C, c – 250°C, d – 300°C.

do not form a continuous film and have outlined contours. During the temperature treatment at 250°C (Fig. 5c), a pronounced convergence of palladium nanoparticles is observed due to the destruction of the stabilizing "coat" and the formation of agglomerates. Metallic films obtained at 300°C (Fig. 5d) are characterized by an obvious blurring of the boundaries between small-sized nanoparticles, the surface acquires a smoothed structure.

The lower melting temperature of palladium films (300°C) relative to compact metal (1554°C) is characteristic of nanoscale objects. This circumstance opens ample opportunities for using palladium as an alternative material in flexible microelectronics.

Variation of surface resistivity values with treatment temperature is shown in Fig. 6.

With increasing of annealing temperature the decrease of surface resistivity from 0.38 to 0.07 Ohm is observed (Fig. 6)

According to thermogravimetric analysis, the palladium content in the ink was 20 wt%.

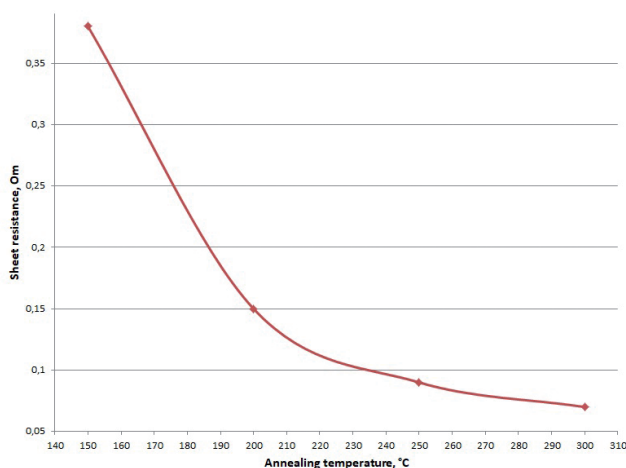


Fig. 6. Dependence of surface resistivity of palladium films on processing temperature.

The use of a combination of high and low – boiling solvents in the composition of the ink contributes to good wettability to various materials (glass, ceramics, polymer) and provides optimal values of viscosity (17-20 cP) and surface tension (35-38) N/m for successful printing. The obtained palladium nano-ink is stable for more than 6 months and can be recommended for use in printed electronics.

4. CONCLUSION

In this work, the synthesis of palladium nanoparticles by the polyol method was proposed. The obtained nanoparticles and inks based on them were investigated and characterized by a complex of physical and chemical methods.

According to the results, nanoparticles contain small ($d = 13$ nm) and large ($d = 90$ nm) spherical particles. The phase composition of the nanoparticles in the sample corresponds to palladium with a cubic crystal structure. The SEM data of metallic films obtained from palladium nano-ink under temperature treatment (150°-300°C) report a change in surface morphology. As the annealing temperature increases, the boundaries between nanoparticles are blurred and the surface acquires a smoothed structure. This effect is reflected in the decrease of the films surface resistivity from 0.38 to 0.07 Ohm.

The obtained nano-ink has relatively high time stability (more than 6 months), is characterized by good wettability to various materials (glass, ceramics, polymer), contains 20% wt% palladium and can be recommended for use in the field of printed electronics.

REFERENCES

1. Vasiliev AA, Kim VP, Tkachev SV, Kornilov DYU, Gubin SP, Vlasov IS, Jahatspanian IE, Sizov AS. Platinum Based Material for Additive Technology of Gas Sensors. *Materials Science. Proceedings of Euroensors 2018 Conference*, Graz, Austria, 9–12 September, 2018, 2(13):738. DOI: 10.3390/proceedings2130738.
2. Tao R, Ning H, Chen J, Zou J, Fang Z, Yang C, Zhou Y, Zhang J, Yao R, Peng J. Inkjet Printed Electrodes in Thin Film Transistors. *IEEE Journal of the Electron Devices Society*, 2018, 6:774-790. DOI:10.1109/JEDS.2018.2852288.
3. Amruth C, Szymanski MZ, Luszczynska B and Ulanski J. Inkjet Printing of Super Yellow: Ink Formulation, Film Optimization, OLEDs Fabrication, and Transient Electroluminescence. *Scientific Reports*, 2019, 9(1):1-10. DOI: 10.1038/s41598-019-44824-w.
4. Dang MC, Nguyen DS, Dang TMD, Tedjini S and Fribourg-Blanc E. Design and testing of RFID sensor tag fabricated using inkjet-printing and electrodeposition. *Advances in Natural Sciences: Nanoscience and Nanotechnology*, 2014, 5(2:025012):1-7. DOI: 10.1088/2043-6262.5.2.025012.
5. Basak I, Nowicki G, Ruttens B, Desta D, Prooth J, Jose M, Steven Nagels, Boyen H-G, D'Haen J, Buntinx M and Deferme W. Inkjet Printing of PEDOT:PSS Based Conductive Patterns for 3D Forming Applications. *Polymers*, 2020, 12(12):2915. DOI: 10.3390/polym12122915.
6. Hrytsenko O, Hrytsenko D, Shvalagin V, Grodziuk G and Kompanets M. The Use of Carbon Nanoparticles for Inkjet-Printed Functional Labels for Smart Packaging. *Materials Science. Journal of Nanomaterials*, 2018, 2018:1-10. DOI: 10.1155/2018.6485654.
7. Kamyshny A, Steinke J, Magdassi S. Metal-based Inkjet Inks for Printed Electronics. *The Open Applied Physics Journal*, 2011, 4(19):19-36. DOI: 10.2174/1874183501104010019.
8. Tkachev SV, Gubin SP, Kim VP, Kushnir AE, Kornilov DYU. The dispersions of nanoparticles in water-organic solvents as the basis for the silver nano-ink for inkjet printing. *RENSIT: Radioelectronics. Nanosystems. Information technologies*, 2016, 8(2):171-184. DOI: 10.17725/rensit.2016.8.171.
9. Wolfe DB, Love JC, Paul KE, Chabinye ML and Whitesides GM. Fabrication of palladium-based microelectronic devices by microcontact printing. *Applied Physics Letters*, 2002, 80(12): 2222-2224. DOI:10.1063/1.1463719.
10. Shakil Hussain SM, Kamal MS and Hossain MK. Recent Developments in Nanostructured Palladium and Other Metal Catalysts for Organic Transformation. *Journal of Nanomaterials*, 2019, 2019:1-17. DOI: 10.1155/2019.1562130.
11. Tereshchenko AA, Polyakov VA, Guda AA, Bulgakov AN, Tarasov AL, Kustov LM, Butova V, Trigub A, Soldatov AV. Synthesis and Description of Small Gold and Palladium Nanoparticles on CeO₂ Substrate: FT-IR Spectroscopy Data. *Journal of Surface Investigation: X-Ray, Synchrotron and Neutron Techniques*,

2020, 14(3):447-458. DOI: 10.1134/S1027451020030180.

12. Akbayeva DN, Bakirova BS, Seilkhanova GA, Sitzmann H. Synthesis, Characterization, and Catalytic Activity of Palladium-polyvinylpyrrolidone Complex in Oxidation of Octene-1. *Bulletin of Chemical Reaction Engineering & Catalysis*, 2018, 13(3):560-572. DOI: 10.9767/BCREC.13.3.1980.560-572.

DOI: 10.17725/rensit.2022.14.151

Information Technologies Based on Noise-like Signals: II. Statistical and Fractal Properties of Chaotic Algorithms

Vadim V. Kashin, Vladimir I. Grachev, Viktor I. Ryabenkov, Vladimir V. Kolesov
Kotelnikov Institute of Radioengineering and Electronics of RAS, <http://www.cplire.ru/>
Moscow 125009, Russian Federation

E-mail: vvkashin@cplire.ru, grachev@cplire.ru, ryabenkov.vi@list.ru, kvv@cplire.ru

Received June 11, 2022, peer-reviewed June 18, 2022, accepted June 25, 2022

Abstract: Discrete chaotic signals with high information capacity have been developed and studied on the basis of nonlinear systems with dynamic chaos. The influence of the main parameters of the generating chaotic algorithm with a delay on the statistical, correlation, structural and fractal characteristics of non-periodic pseudorandom integer and binary sequences generated by the algorithm is analyzed by numerical methods. It is shown that non-periodic pseudorandom sequences (PRSs) formed by a chaotic algorithm with a delay, for all values of the main parameters, have good statistical, correlation, structural and fractal characteristics close to random sequences of independent tests. It is shown that these characteristics are provided on a long PRS cycle in a multidimensional phase space with all the basic parameters of the chaotic algorithm and an arbitrary choice of initial conditions. Such binary PRSs can be used quite effectively in telecommunication systems using stream coding of large blocks of information messages from the point of view of secrecy, noise immunity and cryptographic stability of the communication channel.

Keywords: information technology, chaotic dynamics, pseudorandom sequences, redundant codes, noise-like signals

UDC 621.391

Acknowledgments: The work was carried out within the framework of the state task of the Kotelnikov IRE of RAS from the Ministry of Education and Science of the Russian Federation.

For citation: Vadim V. Kashin, Vladimir I. Grachev, Viktor I. Ryabenkov, Vladimir V. Kolesov. Information Technologies Based on Noise-like Signals: II. Statistical and Fractal Properties of Chaotic Algorithms. *RENSIT: Radioelectronics. Nanosystems. Information Technologies*, 2022, 14(2):151-164e. DOI: 10.17725/rensit.2022.14.151.

CONTENTS

- | | |
|---|---|
| 1. INTRODUCTION (152) | 8. SIGNAL SYSTEM VOLUME (159) |
| 2. RESEARCHED ALGORITHM (153) | 9. INFLUENCE OF THE SIZE OF THE ALGORITHM DEFINITION AREA (160) |
| 3. INFLUENCE OF THE DELAY PARAMETER (153) | 9.1. DISTRIBUTION FUNCTION P(x) (161) |
| 4. FRACTAL PROPERTIES OF PSEUDO-RANDOM CYCLES (154) | 9.2. CORRELATION PROPERTIES (162) |
| 5. GEOMETRIC STRUCTURE OF THE PRC (157) | 9.3. BLOCK STRUCTURE (162) |
| 6. BINARY SIGNAL (158) | 9.4. SIGNAL SYSTEM VOLUME (163) |
| 7. BLOCK STATISTICS IN PRC (159) | 10. CONCLUSION (163) |
| | REFERENCES (164) |

1. INTRODUCTION

At present, the most promising method for forming pseudorandom sequence (PRS) is the use of chaotic algorithms that describe the complex nonequilibrium behavior of nonlinear dynamic systems. For application in radio engineering systems, a new class of random sequences is proposed, which are formed on the basis of algorithms that describe the behavior of self-oscillating systems with delay, having dynamic chaos modes [1]. A feature of such systems is their non-linearity and non-periodicity of the time process generated by them. By changing the parameters of such a dynamic system and the initial conditions, it is possible to change the nature of its behavior over a wide range and thereby purposefully control the type and properties of the generated chaotic signal.

The proposed algorithms for generating a chaotic signal simulate the behavior of ring self-oscillatory systems with delayed feedback and strong amplitude-phase nonlinearity. When the signal circulates through the feedback circuit, the non-linearity of the system leads to an expansion of the signal spectrum. The width of this spectrum is limited by the filtering properties of the self-oscillating system. The relationship between these two competing factors—nonlinearity, which broadens the spectrum, and filtering, which narrows the spectrum—makes it possible to create a chaotic signal with a given spectrum width. The signals generated in this case belong to the class of broadband chaotic signals.

In nonlinear dynamical systems described by nonlinear equations with regular (nonrandom) coefficients and oscillating under the action of regular external forces, unpredictable or chaotic oscillations arise. In other words, the solutions to these equations are very sensitive to small changes in the initial conditions. Another important property of chaotic oscillations

is the loss of information about the initial conditions: chaotic oscillations “forget” the initial state.

Despite the fact that random number generators have been known for a long time, recently, however, much attention has been paid to the study of a new method for obtaining pseudo-random sequences based on systems with dynamic chaos. Random number generators play an important role in the statistical modeling of systems. In this case, one of the main issues is the assessment of their stochasticity. The efficiency of statistical modeling of systems on a computer and the reliability of the results obtained significantly depend on the quality of the initial (basic) sequences of pseudo-random numbers, which are the basis for obtaining stochastic effects on the elements of the system being modeled. The number of random numbers used to obtain a statistically stable estimate of the characteristics of the system functioning process when implementing a modeling algorithm on a computer varies within a fairly wide range depending on the class of the simulation object, the type of estimated characteristics, the required accuracy and reliability of the simulation results.

All used random number generators undergo thorough preliminary testing, which is a set of checks on various statistical criteria, including as the main checks (tests) for equability, stochasticity and independence. Therefore, the availability of simple and economical methods for generating sequences of random numbers of the required quality largely determines the possibility of their practical use in machine statistical modeling of systems and when used in noise-immune information channels.

In information systems with redundant coding during information transmission, the problem of the possibility of absolutely accurate reproduction of the code sequence at

a known key for the numerical reproduction of a chaotic process of long duration remains relevant, which is rather problematic in dynamic systems with continuous time.

This problem can be largely solved by using chaotic random integer generators, the study of the statistical properties of which at a new level has become possible with the development of a new approach - dynamic chaos in discrete systems.

2. RESEARCHED ALGORITHM

In this paper, we consider the chaotic algorithm with delay proposed in [1], which forms a non-periodic pseudo-random sequence (PRS) of integer numbers $\{x_n\}$. Algorithm defined on a finite closed interval of the natural series $[1, M]$, $M > 1$:

$$\begin{aligned} \tilde{x}_n &= x_{n-1} + (-1)^{x_n - Kz} \cdot x_{n-Nz}, \\ (Kz \in [2, Nz-1], Nz > Kz, x_n \in [1, M]), \\ x_n &= \tilde{x}_n, \quad \text{if } \tilde{x}_n \in [1, M], \\ x_n &= \tilde{x}_n - M, \text{ if } \tilde{x}_n > M, \\ x_n &= \tilde{x}_n + M, \text{ if } \tilde{x}_n < 1. \end{aligned} \tag{1}$$

where Nz is the delay parameter that determines the dimension of the phase space (PS) of the algorithm, and the number Kz is selected from the interval of integer numbers $[1, Nz]$ of the delayed members of the sequence, the parameter M determines the largest of the PRS numbers. It was shown in [1] that algorithm (1), with an appropriate choice of parameters, generates the PRS of integers, and after clipping, binary sequences with statistical and correlation properties close to those of random sequences. In this case, the length of a non-periodic segment of the sequence before the loop closes can be very large: $N = 10^{12}$ and more.

The phase space (PS) of the algorithm is a finite set of M^{Nz} points of states of a given discrete dynamic system (DS), which, in its movement in the PS, from the initial state with

the corresponding radius vector $\vec{R}_0(x_{-1}, x_{-2}, \dots, x_{-Nz})$ passes discretely to another PS point with a radius vector \vec{R} according to the law determined by mapping (1). Due to the limited set of PS points, the movement of system (1) occurs along closed "trajectories" of one or several cycles, which, due to the uniqueness of the transformations used, do not have common points. All PS points belong only to one particular cycle, or to an isolated point with coordinates (M, M, \dots, M) . All cycles are nested one inside the other, covering all states of the DS.

Note that for $Kz = Nz$ the behavior of the DS differs from the behavior of the system described by algorithm (1). With an appropriate choice of the values of the algorithm parameters and a sufficient number of points on the cycle, transitions in the PS, as a rule, are random in nature, and at the same time are completely determined, and the algorithm forms herewith a pseudo-random sequence before the cycle is closed. Such cycles we will call pseudo-random cycles (PRCs), i.e., "strange" regions [2] of a given conservative system that preserves the phase space. These cycles are isolated numerical sets, not connected by trajectories, which are not attracting regions, in contrast to the "strange attractor" of continuous time DS.

3. INFLUENCE OF THE DELAY PARAMETER

The main parameter of the algorithm (1) is the delay parameter Nz , which determines the main characteristic of the algorithm - the dimension of the PS and the total number of state points of a given DS in this space - M^{Nz} . To demonstrate the main results of the analysis, we confine our studies to small values of the algorithm parameters. For example, **Table 1** shows the number of PS points and the cycle spectra (i.e., the periods of cycles existing in

Table 1

Cycle spectrum of algorithm (1) for $M = 5, K_z = 3$

N_z	M^{N_z}	Number of DS state points on cycles
4	625	562, 27(2 cycles), 8, 1
5	3125	2291, 183, 170, 169, 1
6	15625	11687, 3223, 463, 110, 1
7	78125	56640, 9948, 2761, 1744, 1429, 420, 423, 339, 211, 150, 1
8	390625	252618, 106377, 10679, 10152, 2990, 1 (spectrum is not shown in full)

the PS and their number) of algorithm (1) with a change in the quantity delay and fixed values of the parameters K_z and M .

From Table 1 it can be seen that when the delay value changes, the spectrum of cycles changes completely. Herewith does not happen simple addition of new or repeating cycles.

On **Fig. 1** and **Fig. 2** shows the structure of PS of algorithm on the example of individual cycles from $N_c = 118$ points ($N_z = 3, K_z = 2, M = 5$) and $N_c = 414$ ($N_z = 3, K_z = 2, M = 9$). For clarity, the successive points of the state of the DS on the cycles are connected by straight lines.

It can be seen from the figures that the successive points of the states of this DS on the cycle are located randomly. These points correspond to the PRS formed by the given

algorithm. In this case, the cycle occupies almost the entire volume of the PS.

4. FRACTAL PROPERTIES OF PSEUDORANDOM CYCLES

To assess the degree of chaotic state of the processes, generated by the algorithm before the cycles are closed, one can use the fractal properties of the PRCs.

In the classical dynamics of systems, three types of dynamic motion were known: equilibrium, periodic motion, or limit cycle, and quasi-periodic motion. These states are called attractors, since in the presence of damping the system is “attracted” to one of the listed states.

Chaotic oscillations represent a new class of motions that cannot be reduced to any of the above. This class of motions is often associated with a state called a strange attractor. Classical attractors correspond to classical geometric regions in phase space: a point, a closed curve, or a surface in three-dimensional phase space. The strange attractor, as it turned out, is associated with a new geometric object – a fractal. The concept of a fractal was first formulated by Benoit Mandelbrot [4]. The

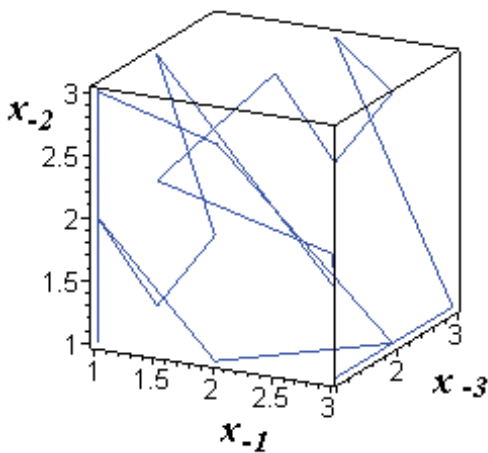


Fig. 1. Phase portrait of algorithm (1) with parameters $N_z = 3, K_z = 2, M = 5$ ($N = 51$ cycle points $N_c = 51$ are shown). $M^{N_z} = 125$.

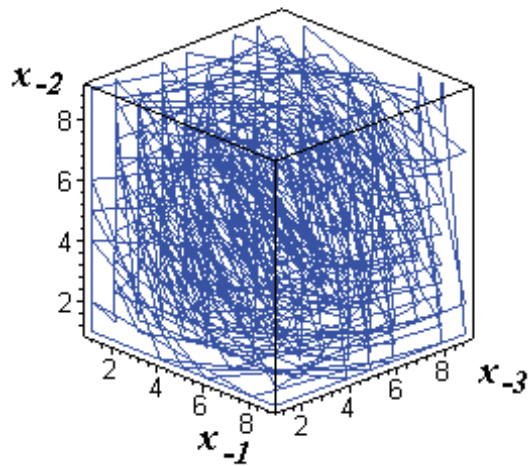


Fig. 2. Phase portrait of algorithm (1) with parameters $N_z = 3, K_z = 2, M = 9$ ($N_c = 414, N = 414$). $M^{N_z} = 729$.

main content of the theory of fractals is that, within the framework of this theory, objects are considered whose dimension is greater than their topological dimension and is a fractional value.

We study the change in the parameter of the correlation dimension of the cycles of algorithm (1) with a change in the value of the parameter N_z . We will determine the correlation dimension of the set of points on cycles based on the calculation of the correlation integral $C(l)$, determined by the number of pairs of points, the distance between which in the PS is less than l [3].

We will calculate the correlation integral for small values of all parameters of the algorithm: N_z , M , and K_z . The last two parameters $M = 5$ and $K_z = 3$ will be unchanged, and the delay parameter will be changed within $N_z = 4 \div 7$. The results obtained are shown in **Fig. 3** and **Fig. 4**, on which the dependences of the logarithm of the correlation integral on the logarithm l are plotted. The bases of the logarithms are 2.

First, it is necessary to analyze the dependence of the correlation dimension on

the number of points at the cycle taken to calculate the correlation integral. Obviously, for a relatively short cycle length, all its points are taken. But as the cycle length increases, the counting time required to determine the distances between all possible pairs of numbers sharply increases, so only a part of the system state points is analyzed on long cycles.

On Fig. 3 plots $\log C(l)$ versus $\log l$ for cycles of algorithm (1) with parameters $M = 5$, $K_z = 3$ and $N_z = 6$, $\mathbf{R}_0(4, 1, 4, 4, 4, 3)$. One curve in this figure corresponds to taking into account all points on a cycle with a small period $N_c = 463$. The total number of pairs of points introduced into consideration in this case is $N_R = 104196$. Three other dependencies are determined for another, longer cycle containing $N_c = 3223$ system state points, $\mathbf{R}_0(3, 4, 1, 2, 4, 3)$. At the same time, the calculation of the correlation integral took into account not all points of the set, but only part of them: 500 for $N_R = 122265$, 1000 for $N_R = 494515$, or 2290 for $N_R = 2.6 \cdot 10^6$ cycle points. It can be seen from the graph that all four curves almost completely coincided. Consequently, the fractal dimension of the two studied

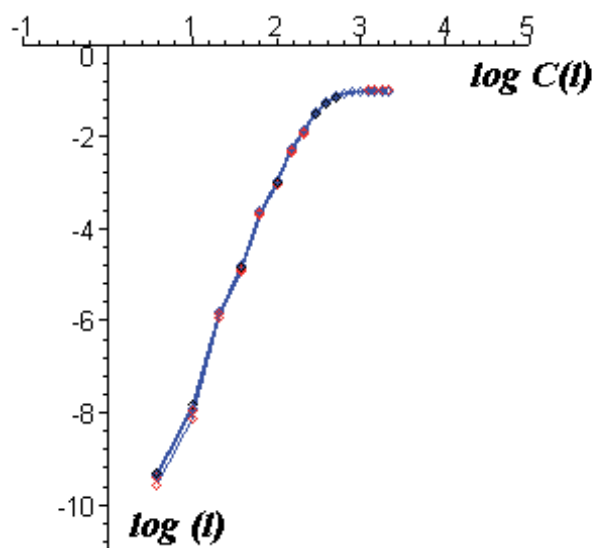


Fig. 3. Dependence of the correlation integral logarithm on the logarithm l for four cycles of the algorithm ($M = 5$, $K_z = 3$, and $N_z = 6$).

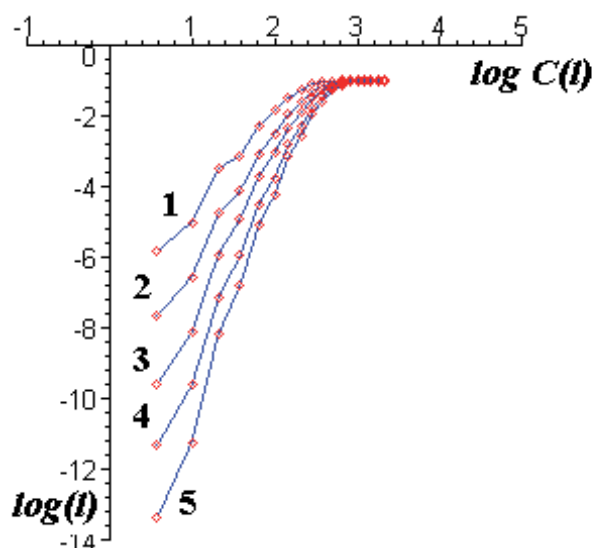


Fig. 4. Dependence of the correlation integral logarithm on the logarithm l for different values of the parameter N_z ($M = 5$, $K_z = 3$).

cycles of the algorithm ($N_c = 463$ and $N_c = 3223$) is the same and is completely determined only by the parameters of the algorithm, and not by the sizes of the cycles.

Graphs Fig. 3 and Fig. 4 do not have clearly defined linear segments, therefore, the exact determination of the fractal dimension of the cycles from the local angular slope of the graph curves gives a significant scatter, while the estimate of the correlation dimension gives the value $D_2 \sim 4.8$ with the geometric dimension of the PS equal to 6.

On Fig. 4 plots $\log C(l)$ versus $\log l$ for separate cycles of algorithm (1) with the same parameters $M = 5$, $K_z = 3$ and different delay values:

$N_z = 4$, $N_c = 562$, $\mathbf{R}_0(3, 5, 3, 2)$, $N = 561$, $N_R = 155396$, $D_2 \sim 3.0$ (curve 1),

$N_z = 5$, $N_c = 2291$, $\mathbf{R}_0(4, 3, 1, 4, 2)$, $N = 1000$, $N_R = 495510$, $D_2 \sim 3.7$ (curve 2),

$N_z = 6$, $N_c = 3223$, $\mathbf{R}_0(3, 4, 1, 2, 4, 3)$, $N = 2290$, $N_R = 2.6 \cdot 10^6$, $D_2 \sim 4.8$ (curve 3),

$N_z = 7$, $N_c = 1429$, $\mathbf{R}_0(2, 2, 1, 2, 3, 2, 4)$, $N = 14228$, $N_R = 1.06 \cdot 10^6$, $D_2 \sim 5.2$ (curve 4),

$N_z = 8$, $N_c = 10152$, $\mathbf{R}_0(5, 3, 3, 4, 3, 2, 2, 4)$, $N = 2000$, $N_R = 2.0 \cdot 10^6$, $D_2 \sim 6.5$ (curve 5).

The results obtained show that as the delay parameter increases, the fractal dimension of pseudorandom cycles increases, which leads to better chaotization of processes in a discrete DS and, accordingly, to an improvement in the statistical characteristics of the formed PRS. At the same time, the observed difference between the correlation dimension and the geometric dimension of the PS indicates some inhomogeneity in filling the space with points of the pseudorandom cycle, at least for relatively small values of N_z , M .

The probability distributions of the generated numbers $p(x)$ for many cycles, especially long ($N \sim N_c$) cycles, are close to a

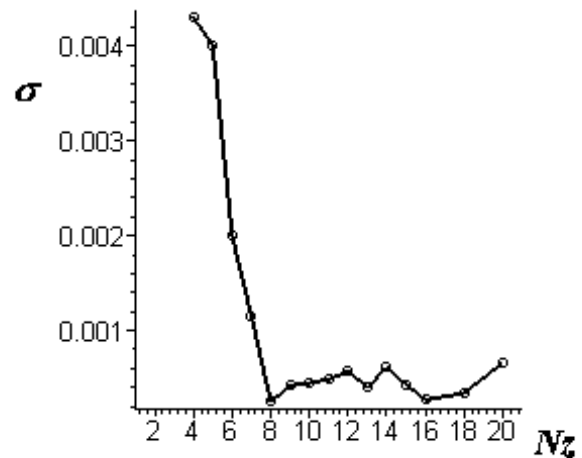


Fig. 5. Root-mean-square deviation from the uniform distribution of pseudo-random sequences generated by the algorithm depending on the parameter N_z ($M = 5$, $K_z = 3$).

uniform distribution ($p(x) = 1/M$). The root-mean-square deviations from the uniform law for the PRS generated by the algorithm at $M = 5$, $K_z = 3$ and different delay values are shown in Fig. 5:

The numerical values of σ obtained on this graph at $N_z = 4 \div 10$ refer to the longest of the set of cycles in the PS (see Table 1) with the corresponding initial conditions. In this case, the analyzed length of the sequence was equal to the length of the cycle: $N = N_c$. For delays $N_z = 11 \div 20$, at which the length of cycles exceeded $N = 10^7$, the initial conditions were taken to be unitary (1, 1, ..., 1), and the length of the analyzed PRS was $N = 500000$.

As the analysis showed, for all studied delay values, the algorithm generates a PRS with a probability distribution that is continuous over all generated numbers and is close to a uniform law. But, as follows from the data in Fig. 5, if at small delays the rms deviation is about 10^{-3} , then with an increase in the parameter N_z , the difference from the uniform distribution density $p(x) = 1/M$ decreases.

For practical purposes of encoding information, it is expedient to use a large

length PRS, and, consequently, large values of the parameters N_z , M are required. Similar conclusions for the distribution function will be valid in this case as well. So, when studying the dependence $\sigma = f(N_z)$ for pseudorandom cycles of algorithm (1) with the domain of definition [1, 255], i.e. $M = 255$, and with the same parameter $K_z = 3$, the following result was obtained: with an increase in the delay from $N_z = 4$ to $N_z = 24$ and the length of the analyzed implementations of the PRS from $N = 210000$ terms, the difference between the distribution density $p(x)$ and the uniform law is approximately the same, and is in the range from $\sigma = (1.3 \div 1.5) \cdot 10^{-4}$.

Thus, it is shown that the sequence generated by the algorithm has an almost uniform distribution law, which is actually independent of the delay quantity. It should be noted that the difference from the uniform distribution law decreases significantly with the expansion of the domain of definition of the algorithm [1, M].

5. GEOMETRIC STRUCTURE OF THE PRS

Let us analyze the behavior of the DS state points on a pseudo-random cycle using fractal geometry methods, considering a random sequence generated by algorithm (1) as an analogue of the geometric relief of a complex "coastline" with a digitized value of its heights and depths of depressions. Let us estimate the geometric structural complexity of such a relief by determining the probabilities of the modulus of equal distances between adjacent points of the geometric relief. In arithmetic representation, this is equivalent to the modulus of the same difference between neighboring numbers in the PRS.

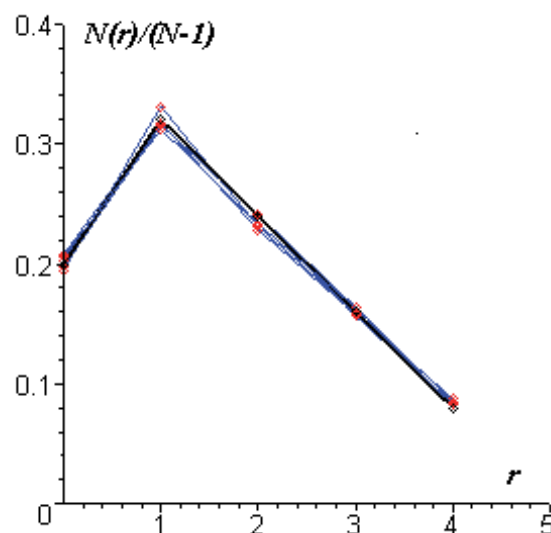


Fig. 6. Probabilities $p(r) = N(r)/(N - 1)$ of differences between neighboring numbers $r = |x_n - x_{n+1}|$ in realizations of sequences with $K_z = 3$, $M = 5$.

On **Fig. 6** plots the frequency dependences $N(r)/(N - 1)$ of the occurrence of identical events: $|x_n - x_{n+1}| = r$, $n = 1, \dots, (N - 1)$, $r = 0, \dots, (M - 1)$ in a sequence of N members depending on the value of r for the same cycles as in **Fig. 4**.

On **Fig. 6** plots the dependence of $N(r)/(N - 1)$ on r for the same cycles as in **Fig. 4** ($N_z = 4 \div 8$), as well as a reference (prototype) graph for a random process with a uniform distribution. The total value of the deviation modules of probabilities $p(r)$ from the reference values $p_{ref}(r)$: $s = \sum |p(r) - p_{ref}(r)|$ and the coefficient of geometric structural complexity of the sequence $\{x_n\} - S/(1 + s)$, are presented in **Table 2**.

From the data in **Fig. 6** it can be seen that all points $p(r)$ for all the studied cycles with different delays N_z are very close to

Table 2

N_z	N_c	s	S
4	562	$1.15 \cdot 10^{-2}$	0.988
5	2291	$2.87 \cdot 10^{-2}$	0.972
6	3223	$2.93 \cdot 10^{-2}$	0.971
7	1429	$3.17 \cdot 10^{-2}$	0.969
8	10152	$1.49 \cdot 10^{-2}$	0.985

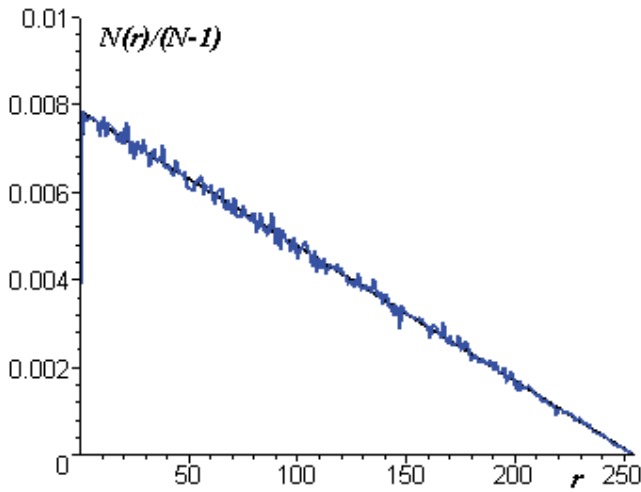


Fig. 7. Probabilities $p(r) = N(r)/(N - 1)$ of differences between neighboring numbers $r = |x_n - x_{n+1}|$ in realizations of sequences at $M = 255$.

each other and to the reference values, and, accordingly, the coefficients of structural complexity of the generated PRSs are close to unity.

Similar results were obtained for the PRS of algorithm (1) with the domain of definition [1, 255], $Kz = 3$, unit initial conditions and implementation length $N = 2100$: when the parameter Nz changes from the value 4 to the value $Nz = 24$. The summary difference from the reference graph is within $(2.5 \div 3.2) \cdot 10^{-2}$, coefficient S is close to the value of 0.97. On **Fig. 7** plots the dependence $p(r)$ for the delay $Nz = 24$ ($s = 2.54 \cdot 10^{-2}$, $S = 0.975$) and the theoretical line $p(r)$. It can be seen from the figure that both graphs are close to each other.

Thus, for the studied values of the algorithm parameters, the fractal geometric structural complexity of the PRS formed by pseudo-random cycles, for fixed parameters M and Kz , any delay values $Nz > 4$, and a cycle length greater than at least $0.02 MNz$, practically does not differ from the complexity of a random evenly distributed process.

6. BINARY SIGNAL

Estimation of the correlation characteristics of clipped (reduced to binary) segments of the generated sequences at different values of the delay parameter (Nz from 3 to 24) showed that the lateral outliers of aperiodic autocorrelation functions and cross-correlation functions for the analyzed values of Nz are practically within the same limits: $(1.3 \div 4.5)/\sqrt{N}$ for ACF of arbitrarily chosen 100 segments of length $N = 128$ symbols, and $(2.4 \div 5.0)/\sqrt{N}$ for ACF of arbitrarily chosen 50 segments of length $N = 1024$. The largest outliers of cross-correlation functions are approximately in the same range (**Table 3**).

The analysis was carried out for clipped PRSs formed by algorithm (1) with a domain of definition [1, 255] and unitary initial conditions. It follows from the results obtained that one of the most important statistical characteristics of the process being formed – the level of the highest correlation function outliers, is close to the corresponding characteristic of random sequences [5], somewhat yielding to it, and with a significant volume of PS, practically does not depend on the quantity of the feedback parameter.

The result obtained is possible only if the values taken by the sequence on all projections of the state vector in the PS are

Table 3

Statistical characteristics $R_{\max} \sqrt{N}$ of clipped PRSs generated by algorithm (1) for different values of the delay parameter

Nz	ACF		CCF	
	N = 128	N = 1024	N = 128	N = 1024
3	1.3 - 4.5	2.6 - 4.6	1.7 - 4.2	2.4 - 5.0
5	1.5 - 3.8	2.7 - 4.9	1.6 - 4.1	2.8 - 4.5
7	1.5 - 4.0	2.7 - 4.2	1.5 - 4.0	2.5 - 4.3
9	1.7 - 4.4	2.4 - 4.4	1.6 - 3.5	2.5 - 4.2
12	1.7 - 3.8	2.6 - 5.0	1.6 - 4.1	2.4 - 4.5
16	1.3 - 3.6	2.5 - 4.7	1.5 - 4.0	2.3 - 4.4
24	1.5 - 3.8	2.5 - 4.3	1.5 - 3.8	2.7 - 4.2

statistically independent. At the same time, adding additional coordinates to the PS practically does not change the characteristics of the process in the case of finding the state vector on a chaotic trajectory. At the same time, by increasing the PS dimension, and, therefore, increasing the total number of admissible state vectors and reducing the proportion of short cycles, the possibilities of obtaining a non-periodic movement of a long duration increase significantly. The same conclusion is confirmed by the results of the analysis of the block structure of generated sequences after clipping and the selection of balanced codes with given correlation properties.

7. BLOCK STATISTICS IN PRS

The dependence of the block structure $V(k)$ of clipped sequences on the value of the feedback parameter Nz is shown in Fig. 8. The number of blocks of the greatest length k_{max} recorded in the experiment and their number $V(k_{max})$ are presented in Table 4. Counting blocks of identical characters in sequences of $N = 270000$ members indicates that with $Nz \leq 5$, the algorithm generates sequences with a block structure that has significant differences from the law $P(k) = 1/2^k$. Curve 1 in Fig. 8, corresponding to the feedback

Table 4

Number of max blocks		
Nz	k_{max}	$V(k_{max})$
3	13	32
5	16	4
7	17	1
9	19	1
12	18	2
16	19	1
24	18	1

parameter $Nz = 3$, deviates significantly from this law, starting from a block of size $k = 7$. At the same time, blocks with a size greater than $k = 13$ were not recorded over the analyzed sequence length.

As the delay increases from $Nz = 3$ to $Nz = 9$, the presence of ever longer blocks up to $k = 19$ is fixed in the generated sequence of a given length, and the statistics of the block structure noticeably improves. With a further increase in the delay to $Nz = 24$, the probabilities of the number of blocks $P(k)$ as a function of their size k differ little from the ideal dependence $P(k) = 1/2^k$. The size of the largest block on the studied segment of the formed sequence of 270000 members practically does not change anymore, remaining at the level of $k_{max} = 18 \div 19$ symbols. At the same time, the presence of one or two such blocks over the length of the sequence is consistent with the expected probability of their occurrence.

Thus, the performed numerical experiment and the results obtained show that the block structure of the clipped sequence generated by algorithm (1) turns out to be close to the ideal distribution law $1/2^k$ with a delay $Nz > 5$, when the probability distribution of the numbers generated by the algorithm is almost uniform, and the initial conditions are chosen in such a way as to ensure their statistical independence. The distribution uniformity and statistical independence of the PRS values are

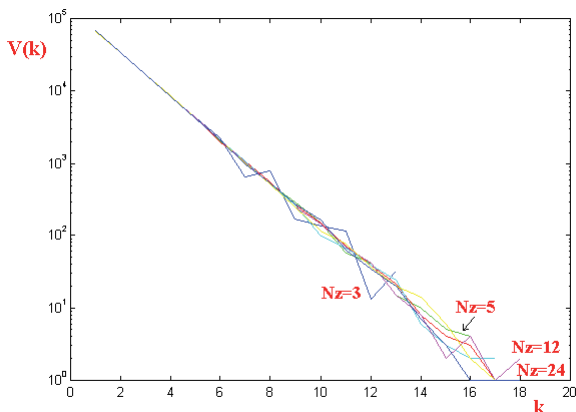


Fig. 8. The number of blocks of identical symbols in the clipped PRS depending on the parameter Nz

necessary conditions for the high quality of the statistical and correlation characteristics of the pseudo-random process generated by the algorithm.

8. SIGNAL SYSTEM VOLUME

Signals system volume generated by the algorithm when the value of the feedback parameter Nz was changed was estimated by selecting from the generated clipped sequence balanced (admissible imbalance no more than ±1) codes from $N_{code} = 128$ symbols with the following correlation properties:

- lateral outliers of the aperiodic autocorrelation function (ACF) do not exceed $R_{max} = 2.26/\sqrt{N_{code}} = 0.2$,
- outliers of aperiodic cross-correlation functions (CCFs) over the entire array of selected codes are less than or equal to $R_{max} = 3.39/\sqrt{N_{code}} = 0.3$.

Aperiodic correlation functions were calculated by the formula for balanced sequences $\{x_j\}, \{y_j\}, j = 1, 2, \dots, N_{code}$ [5]:

$$R(m) = \frac{1}{N_{code}} \sum_{j=m+1}^{N_{code}} x_j \cdot y_{j-m}, \quad m \geq 0.$$

The selection of sequences with given correlation properties was carried out on the same fixed length of the generated sequence of $N = 60000$ members. The number of signals $V(\text{codes})$ of balanced codes selected to the system in the numerical experiment, depending

Table 5

Number of selected codes with given correlation properties, $N_{code} = 128$

Feedback parameter Nz	Number of selected codes V(codes)
3	68
4	92
5	94
7	91
9	103
12	91
16	103
24	97

on the value of the feedback parameter of the algorithm, is given in **Table 5**:

Thus, the numerical experiment showed that the number of selected balanced codes of size 128, generated by the algorithm when changing the delay parameter, depends to a small extent on the value of this parameter, remaining approximately at the level of 91÷103 codes with a fixed implementation length of 60,000 symbols. A significant decrease in the number of codes selected in the signals system was observed only at $Nz = 3$. It should be noted that the above results refer mainly to the selection of short segments of the sequence with the size $N_{code} = 128$. It is quite possible that in the formation of a system of long-duration code signals, the role of the delay parameter will be more significant.

9. INFLUENCE OF THE QUANTITY OF THE DEFINITION AREA OF ALGORITHM

When changing the value of the integer interval of the domain of definition of the algorithm $[1, M]$, i.e. values of the parameter M , the number of independent coordinates of the phase space remains unchanged, but its volume M^{Nz} , the number of system state points, changes significantly. Significant changes are also observed in the PS pattern.

For odd values of M , all cycles, as a rule, have a different period, i.e. presented in the singular. For an even value of M , cycles of the same period occur many times. As an example, **Table 6** shows the spectra of cycles for fixed values $Nz = 4, Kz = 2$ (in parentheses the number of cycles in the PS at a multiplicity greater than one is indicated).

It can be seen from the data presented that, for even values of M , the cycles have a short period and, as a rule, are presented repeatedly. At odd values of M , simple regularities in the structure of the spectra of cycles are not observed, and all cycles, with rare exceptions, have different periods.

The influence of the parameter quantity M of the algorithm on the statistical properties

Table 6
Spectra of cycles in the PS of algorithm (1) for different values of the parameter M

M	Spectrum of cycles
2	1, 15
4	1, 15, 30 (8)
8	1, 15, 30 (8), 60 (64)
16	1, 15, 30(8), 60(64), 120(512)
6	1, 15(3), 30(3), 80, 90(12)
12	1, 15, 30(72), 80, 90(192), 240(5)
18	1, 15(6), 30(21), 80, 90(105), 240(27), 270(324)
10	1, 15(5), 30(10), 150(6), 312(2)
20	1, 15, 30(93), 150(918), 312(2), 1560(6)
14	1, 3(2), 15(7), 30(21), 210(168), 342(7)

M	Spectrum of cycles
3	1, 7, 29, 44
5	1, 8, 27 (2), 562
7	1, 9, 22, 427, 653, 1289
9	1, 7, 10, 20, 22, 24, 29, 44, 75, 134, 296, 767, 5132
11	1, 21, 24, 41, 101, 173, 250, 14030
13	1, 626, 2992, 3712, 5056, 7977, 8197
15	1, 27, 44, 176, 562, 828, 1637, 4702, 7764, 11405, 11484, 11881
17	1, 529, 2471, 2549, 3619, 73684
19	1, 4182, 4219, 5067, 5408, 5916, 28778, 75061
21	1, 1289, 2833, 5228, 5401, 25900, 58208, 88633

of the generated sequence was studied by numerical simulation for several odd values $M = 127, 255, 511, 1023$ with a delay parameter equal to $N_z = 16$. The odd values of M are chosen from the considerations of obtaining a non-periodic PRS of obviously large length with an initial vector in a PS with unit coordinates. For large values of the number of states in the PS of the algorithm $M^{N_z} > 127^{16} = 4.6 \cdot 10^{33}$, the probability of getting into a short cycle with non-periodic segments of the generated sequence of size N of the order of 300,000 members is quite small. Since algorithm (1) with an odd value of $M = 255$ was taken as the basis for numerical analysis, odd values of this parameter were also chosen for comparison.

9.1. DISTRIBUTION FUNCTION P(x)

As shown by numerical analysis, algorithm (1) generates a PRS with a probability distribution

of generated numbers close to uniform for all selected values of the parameter M . The difference from the uniform law is characterized by the relative average and maximum difference between the histograms of the frequency of occurrence of numbers in the generated sequence by absolute value, as well as the RMS deviation (Table 7).

When calculating the distribution function, it is necessary to take into account the increase in the sample size with the growth of M in such a way that a proportionally equal number of possible values would fall into each discharge of the histogram. Therefore, Table 7 shows the results of determining $p(x)$ in the case of one implementation duration of $N = 210,000$ members (the first 4 rows), and in the case of an increase in the duration of N each time by a factor of two (the last 4 rows of the table).

For the same value of N , with increasing M , there is a slight increase of distribution difference from uniform one. In this case, the RMS deviation remains the same level. With an increase in the sample length (in proportion to the growth of M), the differences in the modulo distribution of $p(x)$ from the uniform law are the same. In this case, the RMS deviation decreases with increasing M .

Table 7
The difference between the distribution of the frequency of generating numbers from the uniform law when changing the length of the interval of the domain of definition

M	$\Delta p_{av.rel.}$	$\Delta p_{max.rel.}$	σ
127 (N = 210000)	$1.89 \cdot 10^{-2}$	$6.3 \cdot 10^{-2}$	$2.02 \cdot 10^{-3}$
255 (N = 210000)	$2.74 \cdot 10^{-2}$	$9.16 \cdot 10^{-2}$	$2.17 \cdot 10^{-3}$
511 (N = 210000)	$3.84 \cdot 10^{-2}$	$17.8 \cdot 10^{-2}$	$2.15 \cdot 10^{-3}$
1023 (N = 210000)	$5.70 \cdot 10^{-2}$	$22.1 \cdot 10^{-2}$	$2.24 \cdot 10^{-3}$
511 (N = 420000)	$2.72 \cdot 10^{-2}$	$11.43 \cdot 10^{-2}$	$1.53 \cdot 10^{-3}$
127 (N = 60000)	$3.70 \cdot 10^{-2}$	$13.4 \cdot 10^{-2}$	$4.14 \cdot 10^{-3}$
255 (N = 105000)	$4.01 \cdot 10^{-2}$	$13.3 \cdot 10^{-2}$	$3.10 \cdot 10^{-3}$
511 (N = 210000)	$3.84 \cdot 10^{-2}$	$17.8 \cdot 10^{-2}$	$2.15 \cdot 10^{-3}$
1023 (N = 420000)	$3.98 \cdot 10^{-2}$	$17.7 \cdot 10^{-2}$	$1.58 \cdot 10^{-3}$

From the data of Table 7 it can be seen that the distribution of generated numbers is almost uniform for all values of the parameter M and the deviation from this law is actually the same. The distribution of conditional probabilities also confirms the uniform distribution of points (x_{i+j}, x_i) over the entire area of the square $[1, M, 1, M]$ in the transition tables (matrices) $x_j(n + s) = f(x_i(n))$ for algorithm with the corresponding values of the parameters M and Nz.

9.2. CORRELATION PROPERTIES

When selecting segments to the signal system, strictly balanced blocks of the clipped sequence with specified correlation properties $R_{max} \leq \epsilon = \alpha / \sqrt{N_{code}} = 0.2 \div 0.3$ were selected. In this numerical experiment, the amplitude of the autocorrelation functions (ACFs) and cross-correlation functions (CCFs) lateral surges was determined with respect to the level $1 / \sqrt{N_{code}}$, i.e. value α . Thus, the obtained values show how many times the CF emissions exceed the level $1 / \sqrt{N_{code}}$. The calculations were carried out for clipped segments of the implementation of the PRS with a length of 270,000 symbols. The results of calculations for 100 segments sequentially formed by the algorithm are shown in Table 8.

The results of Table 8 show that with an appropriate choice of a pseudo-random cycle, which is determined by the initial conditions,

Table 8

The magnitude of the largest outliers $R_{max} \sqrt{N_{code}}$ of the correlation functions of pseudorandom sequences generated by algorithm (1) for various values of the interval length $[1, M]$.

M	Clipped sequence			
	ACF		CCF	
	N = 128	N = 1024	N = 128	N = 1024
127	1.5 - 3.8	2.4 - 4.1	1.8 - 3.8	2.4 - 4.1
255	1.3 - 3.6	2.5 - 4.7	1.5 - 4.0	2.3 - 4.4
511	1.3 - 3.7	2.5 - 4.7	1.3 - 4.3	2.3 - 4.4
1023	1.5 - 3.9	2.5 - 4.6	1.6 - 3.4	2.4 - 4.6

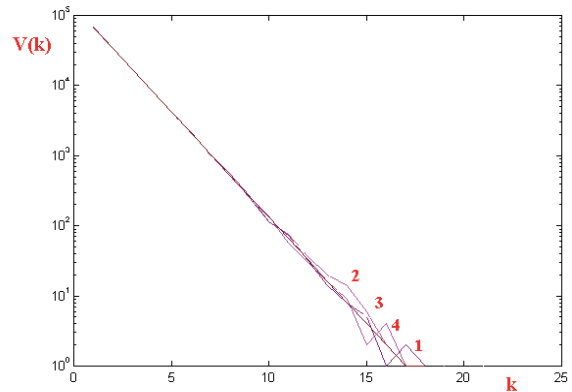


Fig. 9. The number of blocks of identical symbols in the clipped pseudo-random sequence depending on the parameter M: $M_2 = 127$ (curve 1), $M_2 = 255$ (curve 2), $M_2 = 511$ (curve 3), $M_2 = 1023$ (curve 4).

the correlation characteristics of the sequences generated by the algorithm (1) are practically independent of the size of the algorithm definition area and are at the same level as in the formation of code segments of 128 numbers, and in 1024 characters.

9.3. BLOCK STRUCTURE

The distribution of the block structure $V(k) = \text{func}(k)$ of clipped sequences generated by the algorithm with areas of definition $M = 127, 255, 511$ and 1023 is shown in Fig. 9. The sizes of the largest blocks of identical symbols, fixed in the numerical experiment, are shown in Table 9. The length of the analyzed sequence in this case is also 270000 symbols.

As follows from the obtained results, the block structure of binary sequences exactly follows the ideal law $1/2^k$ up to blocks of size $k = 14$, regardless of the interval of the domain of definition of M. In practice, differences from

Table 9

The number and size of the maximum block, fixed in a numerical experiment

M	k_{max}	$V(k_{max})$
127	18	1
255	19	1
511	21	1
1023	1	1

this law for large k can be neglected, because for reliable fixation of rare large blocks of symbols, it is required to analyze the generated sequence over a much longer length. Thus, the data in Fig. 9 indicate the high statistical quality of the PRS generated by the algorithm for any domain of definition chosen for analysis area of definition $[1, M]$.

9.4. SCOPE OF SIGNAL SYSTEM

To estimate the volume of the signal system, the selection of balanced codes of size $N_{code} = 128$ into the signal system with specified correlation properties $R_{max} \leq 0.2$ for ACF and $R_{max} \leq 0.3$ for CCF was carried out for all four values of the parameter $M = 127, 255, 511$ and 1023 . The number of selected balanced codes with given correlation properties at a fixed length of the implementation of the sequence N is different for each case of choosing the value of the parameter M (Fig. 10). For some N , the difference in the number of selected codes reaches 1.5 times. At the same time, the selection rate in this case turned out to be the best for the algorithm with $M = 255$. However, with an increase in the implementation length, the number of selected code segments for all

M becomes close and in the interval $N = 60000$ this number is within $85 \div 103$.

The data on the selection of codes with given correlation properties also confirm the actual independence of the quality of the pseudo-random sequences generated by the algorithm (1) on the size of the domain of definition – parameter M .

Thus, the analysis of the behavior of the dynamic system under consideration with a change in the parameter M has shown that the studied statistical characteristics of the formed PRSs, in fact, little depend on the value of this parameter. In this case, it should be taken into account that the full number of possible states MN_z in the PS of the N_z dimension algorithm (the volume of the PS) depends on the value of M . Nevertheless, for practical purposes of encoding information, it is advisable to choose large values of the algorithm parameters N_z and M and a "long" (i.e., with a large number of DS state points) cycle in the PS, which provides good statistical and correlation properties and the required length of a continuous non-periodic coding sequence.

10. CONCLUSION

Based on a numerical experiment, it is shown in the work that non-periodic pseudo-random sequences (PRSs) generated by the analyzed chaotic algorithm with delay, for all values of its main parameters, have good statistical, correlation and fractal characteristics, close to random sequences of independent trials. It is shown that these characteristics are provided on a long PRS cycle in a multidimensional phase space for almost all the main parameters of the chaotic algorithm and an arbitrary choice of initial conditions. Such binary PRSs can be quite effectively used in telecommunication systems using streaming coding of large

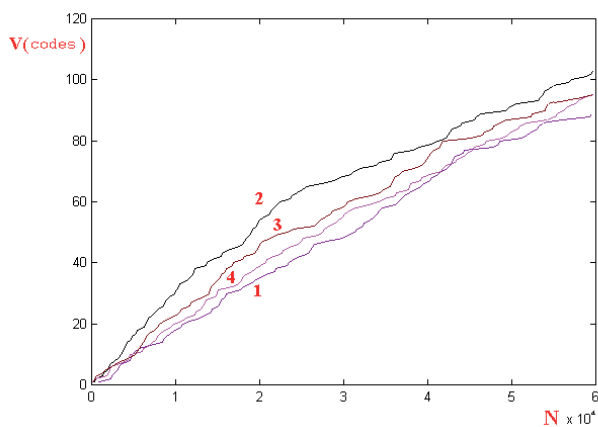


Fig. 10. The number of selected codes ($N_{code} = 128$) with specified properties depending on the length of the implementation of the sequence N , generated by the algorithm (1) for different values of the parameter M : $M_2 = 127$ (curve 1), $M_2 = 252$ (curve 2), $M_2 = 511$ (curve 3), $M_2 = 1023$ (curve 4).

blocks of information messages from the point of view of secrecy, noise immunity and cryptographic stability of the communication channel.

REFERENCES

1. Nikita A. Ageykin, Vladimir I. Grachev, Viktor I. Ryabenkoy, Vladimir V. Kolesov. Information Technologies Based on Noise-like Signals: I. Discrete Chaotic Algorithms. *RENSIT: Radioelectronics. Nanosystems. Information Technologies*, 2022, 14(1):47-64. DOI: 10.17725/rensit.2022.14.047.
2. Schuster HG. *Deterministic Chaos: an Introduction*. Weinheim, Physik-Verlag, 1984, 220 p.
3. Francis C. Moon. *Chaotic and fractal dynamics: An introductions for applied scientists and engineers*. New York, J.Wiley&Sons, cop., 1992, 508 p.
4. Mandelbrot BB. *The Fractal Geometry of Nature*. N.Y., WH Freeman&Co, 1983.
5. Varakin LE. *Sistemy svyazi s shumopodobnymi signalami* (Systems with Noise-Like Signals). Moscow, Radio i Svyaz' Publ., 1979.

DOI: 10.17725/rensit.2022.14.165

Application of the Interpolation Method of Sequential Computation of the Fourier Spectrum to Sparse Images

Alexander V. Kokoshkin, Evgeny P. Novichikhin

Kotelnikov Institute of Radioengineering and Electronics of RAS, Fryazinsky branch, <http://fireras.su/>
Fryazino 141190, Moscow region, Russian Federation

E-mail: shvarts65@mail.ru, epnov@mail.ru

Received April 28, 2022, peer-reviewed May 5, 2022, accepted May 12, 2022

Abstract: Interpolation Method of Sequential Computation of the Fourier spectrum (IMSCS) is used for the reconstruction of sparse digital images. Peculiarities of application of the method are investigated on different types of images with a large sparseness (from 90 to 99 percent of information is missing). To improve the work of IMSCS, when considering the large sparseness of the initial data, its totality includes a procedure for additional iterative refinement of each of the restored harmonics of the spatial spectrum. As an alternative approach, to determine the analysis by objective criteria, spline interpolation is chosen. The conducted study allows us to conclude that it is fundamentally possible to use IMSCS to restore rarefied images, both for the reconstruction of gaps, and in order to reduce the amount of data.

Keywords: remote sensing, sparse digital images, image processing, interpolation method of sequential computation of the Fourier spectrum

UDC 621.397

Acknowledgments: The work was carried out within the framework of the state task of the Kotelnikov IRE of RAS.

For citation: Alexander V. Kokoshkin, Evgeny P. Novichikhin. Application of the Interpolation Method of Sequential Computation of the Fourier Spectrum to Sparse Images. *RENSIT: Radioelectronics. Nanosystems. Information Technologies*, 2022, 14(2):165-174e. DOI: 10.17725/rensit.2022.14.165.

CONTENTS

1. INTRODUCTION (165)
 2. APPLICATION OF IMSCS TO SPARSE IMAGES (166)
 3. CONCLUSION (171)
 4. APPENDIX (172)
- REFERENCES (172)

1. INTRODUCTION

The problem of restoring a signal distorted by various types of lacunae (unfilled data areas) is extremely relevant. It occurs in many practical problems of image and signal processing [1-9]. For example, during remote sensing of the Earth using aerospace vehicles, gaps often appear in the space-time data structure. These losses (areas that are not filled with data) may occur due to the technical features of the

equipment and measurement techniques. This happens due to the specifics of the trajectories and because when we register images in the optical range, the image can be partially covered by clouds. In such cases, it is argued that the image is distorted by the loss of adjacent samples (continuous gaps).

In the work proposed here, sparse images (from unevenly spaced samples) are considered. That is, such images, throughout the field of which there are only a certain number of elements, while most of the elements are missing. Often, in remote sensing, a large amount of memory is required to record the measured data, which affects the processing speed and does not allow real-time observations. Therefore, at present, as a rule, they deliberately resort to reducing the number of measured signals by thinning it out.

An example here is the technology of ultrasonic testing using piezoelectric antenna arrays. It was shown in [10] that the recognition method with compression (Compressive Sensing (CS)) [11–13] makes it possible to increase the rate of recording echo signals by an average of five times by reducing the number measured echoes, and at the same time to obtain high resolution. Generally speaking, in almost all video surveillance systems, in order to save the amount of data, images are subjected to the procedure of "sparseness" (compression) according to various algorithms. The most common compression methods are Discrete Cosine Transformation (DCT), Discrete Wavelet Transformation (DWT), Gabor transformation, and others [14]. Each method that reduces the size of the amount of required memory leads to losses. They appear visually either in the manifestation of the block structure (for DCT) or in blurring of the image (for DWT). The challenge is to find a compromise between the degree of compression, which reduces file sizes, and the worsening of image quality.

The work presented here explores the application of the Interpolation Method of Sequential Computation of the Fourier spectrum (IMSCS) for the reconstruction of various types of images with a high degree of sparseness (90 to 99 percent of information is missing). In the article [15], when we first described the IMSCS, we already demonstrated the preliminary results of the operation of this method with sparse images. There, as the most "hard" case, an example was considered with the absence of about 70 percent of the original image data. And based on the processing examples, it has been argued that IMSCS retouching and restoration can give good results even with a significant proportion of the missing image. In [16], we showed that image inpainting methods, including those implemented using neural networks, do not allow restoring images in continuous gaps. The same applies to all types of image interpolation. At the same time, [16]

demonstrates the ability of IMSCS to partially restore the contents of a continuous gap, while competing methods only retouch those places where image data is lost. Description of the algorithm of the Interpolation Method of Sequential Computation of the Fourier spectrum (IMSCS), according to [16], is given in the Appendix. In the work proposed here, in order to improve the operation of the IMSCS, with a strong sparseness of images, its algorithm includes an internal procedure for additional iterative refinement of each of the harmonics. A similar modification of the technique was used by us to reconstruct one-dimensional acoustic signals from incomplete data [17].

2. APPLICATION OF IMSCS TO SPARSE IMAGES

As a first example, we use the original digital image from the database: <https://www.goodfon.ru/download/lods-franck-portret-lea/1280x1024/>. Let's give this image the name "Portrait" and for the convenience of processing we will make its size 512 by 512 pixels, in addition, we will convert its color in grayscale from 1 - conditionally black, to 255 - white. The result of the transformations is shown in **Fig. 1a**. Based on this, we will model a rarefied image. That is, according to a random uniform law, we will remove ninety percent of the information from Fig. 1a, thus obtaining Fig. 1b. Black field (gradation of brightness = 0) in Fig. 1b corresponds to the missing data, and the remaining ten percent of the informative elements of the image have their original values as in Fig. 1a (from 1 to 255).

In the absence of 90 percent of the data for image reconstruction using the Interpolation Method of Sequential Computation of the Fourier spectrum, it was not necessary to apply the procedure for additional iterative refinement of each of the harmonics. Result of sparse image restoration Fig. 1b is shown in Fig. 1c. "Portrait" is quite recognizable. When comparing Fig. 1a and Fig. 1c, it can be established that the reconstructed image contains a certain number



Fig. 1. Original digital image "Portrait" sized 512 by 512 pixels - (a); Sparse image (10 percent of the total data volume is known Fig. 1a) - (b); IMSCS recovery Fig. 1b (256 harmonics 1 iteration) - (c).

of interfering artifacts. In addition, a visually noticeable decrease in the overall sharpness. This circumstance can be fixed according to objective criteria – "average contrast" and "sharpness rating" [18]. **Table 1** shows these quantitative characteristics. In the left column of Table 1 are

Table 1

Image quality scores for Fig. 1.

Original digital image 512 by 512 pixels "Portrait"	Original digital image (100 percent of the total data is known)	IMSCS reconstruction (10 percent of the total data is known)
Sharpness rating	1.665	1.007
Average contrast	0.063	0.054

shown the results of evaluations for the original image, in the right column – for the reconstruction using IMSCS. The sharpness estimate and average contrast of the reconstructed image are significantly lower than those of the original image. Nevertheless, the information content and quality of Fig. 1c can be considered satisfactory.

For additional control over the preservation of the information content of the reconstructed image, we use Content-based image retrieval (CBIR) – a section of computer vision that solves the problem of finding images that have the required content in a large set of digital images. The Yandex intelligent recognition system will help us with this, which does not experience problems with searching for images on the Internet by the content of the uploaded image Fig. 1c.

Let's consider an even more complicated case. A sparse image with a known one percent of the total data. Let's remove ninety-nine percent of the information from Fig. 1a thus obtaining **Fig. 2a**. As before, the black field (brightness gradation = 0) in Fig. 2a corresponds to the missing data, and the remaining one percent of the informative elements of the image have their original values as in Fig. 1a (from 1 to 255). Fig. 2b demonstrates the result

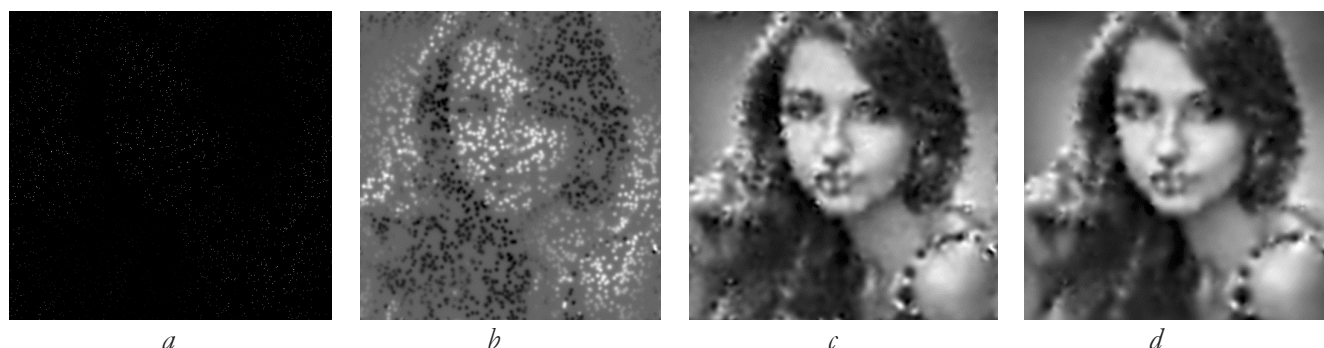


Fig. 2. Sparse image (1 percent of the total data volume is known Fig. 1a) - (a); Restoration of IMSCS (256 harmonics, 1 iteration) - (b); IMSCS recovery (256 harmonics, 20 iterations) - (c); Restoration by spline interpolation - (d).

of applying IMSCS to Fig. 2a without additional iterative refinement of the reconstructed harmonics of the spatial spectrum. With such a reconstruction, the unsatisfactory quality of restoration is obvious. This manifests itself in the form of a "spotted" structure (Fig. 2b). Those, some small recovery area is formed around each informative pixel, and the rest of the image field is filled with average brightness values (grey background). To overcome this limitation, we propose a modification of the IMSCS, which consists in the procedure of additional iterative refinement of each of the harmonics. The number of iterations is chosen empirically and is limited when an acceptable result is achieved. We believe that the sufficient number of iterations is such that the "grey" background of the reconstructed image is completely filled with significant interpolation data. A further increase in the number of iterations not only does not improve the quality of the reconstruction, but also increases the number of interfering artifacts. In the considered example Fig. 2c the number of iterations is 20.

In this work, for a comparative analysis with the proposed Interpolation Method of Sequential Computation of the Fourier spectrum, the missing data are also filled in using the spline interpolation (spline) described in [19,20]. The physical meaning of this algorithm is that for an arbitrary set of reference points (nodes) a system of linear equations is solved that simulates the behavior of a curved elastic plate. The result is a relation that describes a two-dimensional spline surface. Fig. 2 shows the result of applying the spline to the image Fig. 2a. Compared to IMSCS, with iterations (Fig. 2c), spline interpolation reveals a smoother recovery. However, IMSCS, with iterations is better at restoring image details. This becomes apparent if one carefully examines the eyes of the "portrait" in Fig. 2b and Fig. 2c. Of course, the quality of reconstruction in Fig. 2 compared to Fig. 1 is not good enough from an expert point of view. This is natural since the last case is the limit (missing 99 percent of

relevant information). Nevertheless, the Yandex intelligent system (search on the Internet by image) unmistakably finds the original. And not only does it find the original of this photo, this system recognizes the face of a particular person, since it gives out the same girl among the search options, but from a different angle.

In this example (one percent of the data), the spline procedure is comparable in processing time to IMSCS, with iterations. However, to implement calculations of spline interpolation of an image of 512 by 512 pixels, significant computing power is required, therefore, in the seemingly simpler case – the first case (with ten percent of the information), where using IMSCS, with only one iteration, the restoration of a sparse image is much faster and it is better. **Table 2** shows the results of objective methods for evaluating reconstructed images – sharpness evaluation and average contrast. Specified in Table 2 IMSCS, means IMSCS, with 20 iterations. Compared with the data in Table 1 in Table 2 shows a more significant drop in the estimated parameters for IMSCS, compared to the original. In addition, in Table 2 shows the results of estimates for spline interpolation. The estimates of sharpness and average contrast in the reconstruction of the image by spline are even further from the original digital image than the estimates for IMSCS.

As a second example, let's take an optical image received from a satellite – a fragment of the city of San Diego in the USA. For this, a public Yandex map is used. We translate the cut fragment 512 by 512 pixels into a black and white image, where the brightness is distributed

Table 2

Image quality scores for Fig. 2.

Original digital image 512 by 512 pixels "Portrait"	Original digital image (100 percent of the total data is known)	IMSCS reconstruction (1 percent of the total data is known)	Spline reconstruction (1 percent of the total data is known)
Sharpness score	1.665	0.339	0.241
Average contrast	0.063	0.032	0.027

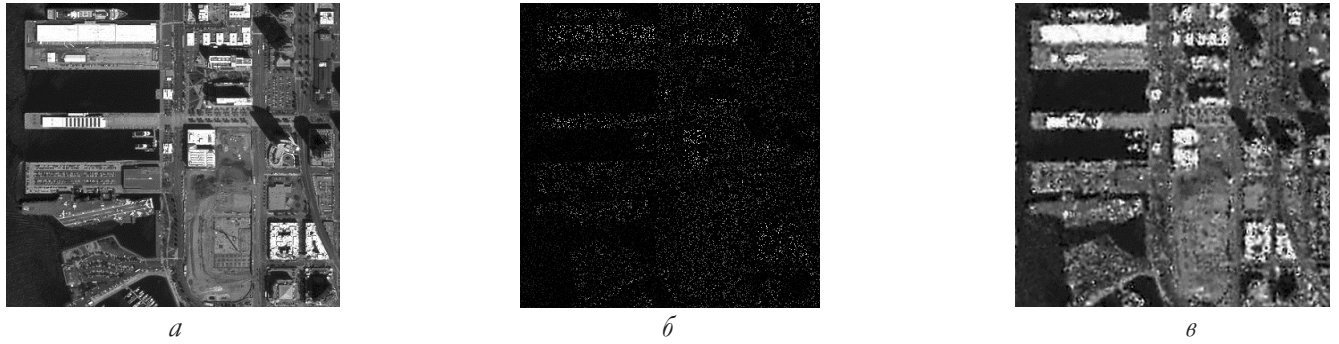


Fig. 3. The original digital image of "San Diego", 512 by 512 pixels in size - (a); sparse image (10 percent of the total data volume is known Fig. 3a) - (b); IMSCS recovery Fig. 1b (256 harmonics 1 iteration) - (c).

from 1 - conditionally black, to 255 - white. The initial sample thus formed is shown in Fig. 3a, let's call it "San Diego". This aerospace image clearly shows the USS "Midway" aircraft carrier moored in the port, which has been turned into a museum ship since 1998 (located in the middle of the left side of the picture). Based on Fig. 3a we simulate a sparse image. That is, as in the first example "Portrait", according to a random uniform law, we will remove ninety percent of the information from Fig. 3a, thus we get Fig. 3b. Black field (gradation of brightness = 0) in Fig. 3b corresponds to the missing data, and the remaining ten percent of the informative elements of the image have their original values as in Fig. 3a (from 1 to 255).

Restoration of Fig. 3b using IMSCS, is shown in Fig. 3c. As in the case with Fig. 1c, to reconstruct a sparse image by interpolating a sequentially calculated Fourier spectrum, it is enough to calculate 256 harmonics of the spectrum and additional iterations of refinement of each harmonic are not required. Despite small artifacts, all significant objects

(city buildings, the outline of the port, an aircraft carrier) have a completely recognizable appearance. However, small image elements (cars, aircraft on board an aircraft carrier, etc.) are not restored. To implement spline interpolation (with ten percent of meaningful information present) requires extremely large computing power. Therefore, the calculations of statistical characteristics were carried out with an image of a smaller size (1/4 part of Fig. 3 is cut out) 256 by 256 pixels Fig. 4.

Visually, that is, by expert evaluation, it is difficult to determine which of the Fig. 4c or 4d is better. Table 3 shows the data of objective assessments of image quality. It can be seen that the sharpness and average contrast of the

Table 3

Image quality estimations for Fig. 4

Original digital image 256 by 256 pixels "San Diego"	Original digital image (100 percent of the total data is known)	IMSCS reconstruction (10 percent of the total data is known)	Spline reconstruction (10 percent of the total data is known)
Sharpness rating	14.071	4.908	3.374
Average contrast	0.16	0.117	0.093

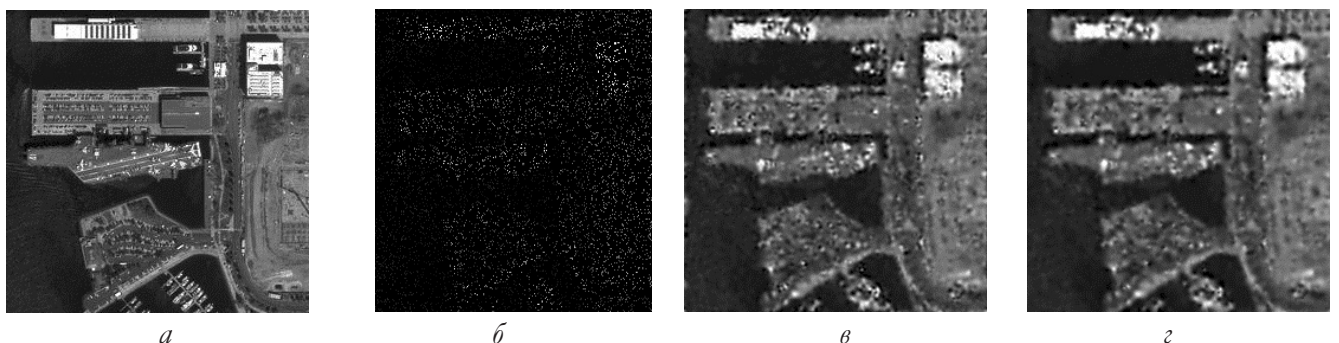


Fig. 4. Original digital image 256 by 256 pixels - (a); Sparse image (10 percent of the total data volume is known) - (b); Reconstruction of IMSCS (128 harmonics, 1 iteration) - (c); Spline reconstruction - (d).

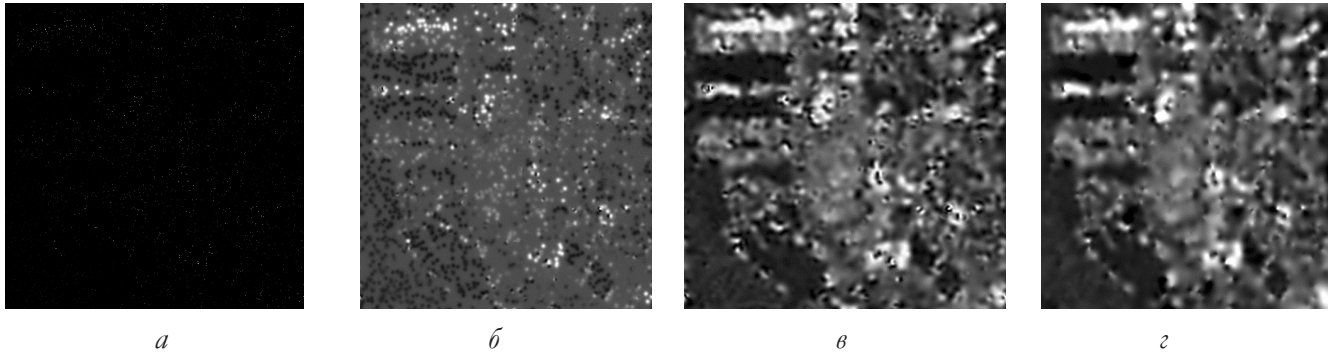


Fig. 5. Sparse image (1 percent of the total amount of data in Fig. 3a is known) - (a); Restoration of IMSCS (256 harmonics, 1 iteration) - (b); Reconstruction of IMSCS (256 harmonics, 20 iterations) - (c); Reconstruction by spline interpolation - (d).

reconstructed images, relative to the original sample, for the "San Diego" example suffered a much more significant decrease than for the "Portrait" example (compare with Table 1). At the same time, the overall sharpness of the original images 1.665 for "Portrait" and 14.071 for "San Diego" differ by almost an order of magnitude. A significant difference in values is also the average contrast of 0.063 for "Portrait" and 0.16 for "San Diego".

Fig. 5 shows the results of the reconstruction of a sparse image when one percent of the total data volume is known of Fig. 3a. It should be noted that with only one percent of the initial data known, the procedure of iterative additional refinement of each of the restored harmonics is necessary. In our work, the number of iterations is 20.

Statistical quality estimates for reconstructions of the 99 percent sparse San Diego image are shown in **Table 4**.

If the restoration of the sparse image "San Diego" when it's known 10 percent of the total amount of data still passes more or less

acceptable, then if 99 percent of the original information is lost, it is no longer necessary to talk about any reconstruction, see Fig. 5. With a certain amount of imagination, you can see the rough outline of the coastline. The Yandex intelligent system for searching images on the Internet based on Fig. 5c or Fig. 5e can't even classify what it is. While for 90 percent sparsity recovery (Fig. 3c), Yandex classifies this as an aerospace image and offers "similar" ones. We remind you that with one percent of the original data for the "Portrait" example, Yandex search unmistakably recognized the image. The point is that the two images taken here as initial ones have significantly different autocorrelation functions (ACF). **Fig. 6** shows the normalized ACF for the original image "Portrait". **Fig. 7** - normalized ACF for "San Diego".

Table 5 shows the number of pixels at which the ACF decreases to a certain level (0.8; 0.7; 0.5) relative to the maximum of the normalized ACF.

Let's call the data Table. 5 conditional correlation radii of the original tested images for different ACF levels. By definition,

Table 4
Image quality estimations for Fig. 5.

Original digital image 512 by 512 pixels "San Diego"	Original digital image (100 percent of the total data is known)	IMSCS reconstruction (1 percent of the total data is known)	Spline reconstruction (1 percent of the total data is known)
Sharpness score	16.441	1.364	0.798
Average contrast	0.176	0.072	0.053

Table 5
Conditional image correlation radius.

Decrease from the maximum of the normalized ACF	0.8	0.7)	0.5
"Portrait" 512*512 Distance in pixels from maximum ACF	28	50	91
"San Diego" 512*512 Distance in pixels from maximum ACF	3	6	25

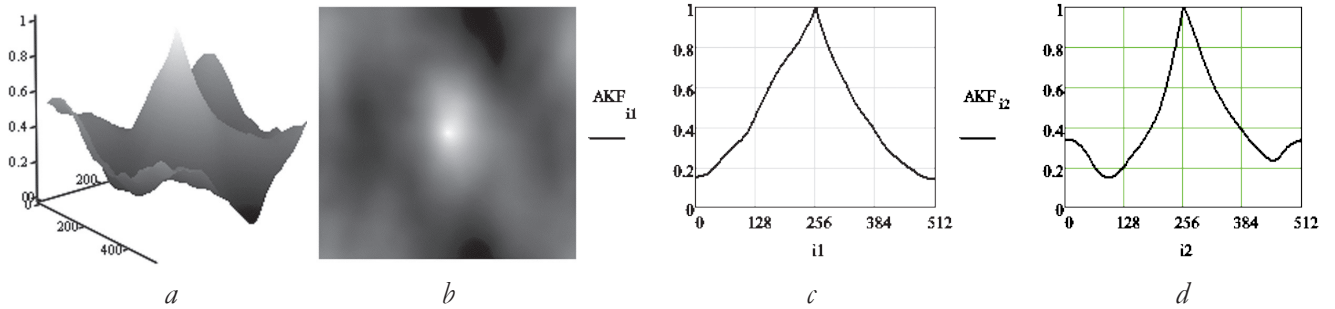


Fig. 6. Autocorrelation function for the original image "Portrait" (Fig. 1a). Volumetric image of the ACF - (a); Volumetric image of the ACF top view - (b); Cross section of the ACF - (c); Cross section of the ACF orthogonal to the section Fig. 6c - (d).

the signal correlation radius indicates at what distance the signal samples can be considered statistically independent. The more homogeneous is the area image, the larger the correlation radius for it. Areas with a small variation in brightness in the image field, from the point of view of correlation analysis, are of little information. For "Portrait" it is a slowly changing background, cheeks, forehead, shoulder, etc., for "San Diego" it is the sea. And vice versa, the more frequent brightness changes in the image, the narrower the autocorrelation function becomes, indicating to the researcher that sparsity should be used with great care to save memory space. Otherwise, if the number of pixels of a sparse image sufficient for the reconstruction of small image details does not fit into the radius of the ACF, then restoration will not occur. If, in the San Diego aerospace example, the most informative areas are the city, roads, port outlines with moored large ships, then it is possible to thin out the original image by 90 percent.

However, if the target is individual cars and small boats, then meaningful information needs to be added to the sparse image. Thus, the allowable sparseness must be chosen for each specific technical task, and for a certain type of image.

3. CONCLUSION

The work proposed here investigates the application of the interpolation method of a sequentially calculated Fourier spectrum for the reconstruction of different types of images with a high degree of sparseness (in the absence of 90 to 99 percent of significant elements). To improve the operation of the IMSCS, with a strong sparseness of the initial data, its algorithm includes an internal procedure for additional iterative refinement of each of the reconstructed harmonics of the spatial spectrum. The possibility of restoring an image distorted by sparseness, with the degree of information content necessary for a specific technical task, must be evaluated by the radius

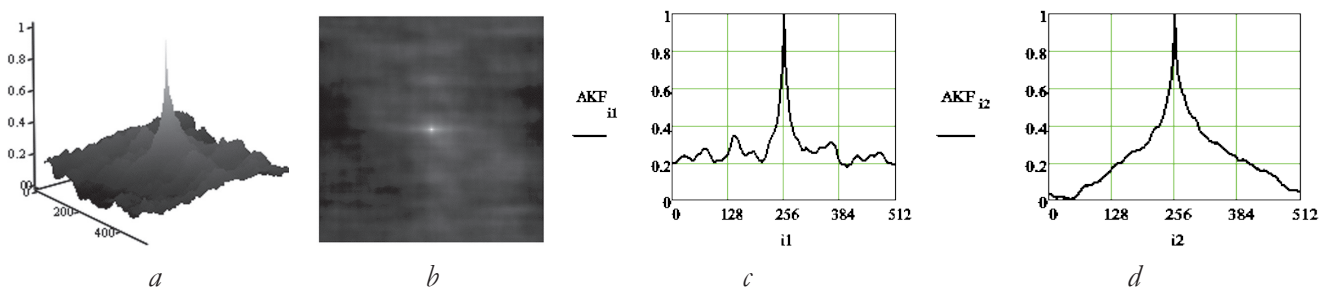


Fig. 7. Autocorrelation function for the original image "San Diego" (Fig. 3a). Volumetric image of the ACF - (a); Volumetric image of the ACF top view - (b); Cross section of the ACF - (c); Cross section of the ACF orthogonal to the section Fig. 7c - (d).

ACF correlation characteristic for the types of images used. According to the objective criteria – "average contrast" and "sharpness estimation" [18], it was found that the spline interpolation used for comparative analysis [19, 20] is significantly inferior to IMSCS. The conducted study allows us to conclude that it is fundamentally possible to use IMSCS to restore sparse images both for the reconstruction of lacunae and for the reduction of the amount of data.

4. APPLICATION

ALGORITHM FOR THE METHOD OF INTERPOLATION OF A SEQUENTIALLY CALCULATED FOURIER SPECTRUM (IMSCS)

The complete image Y_p can be written as the sum of the images outside the gap Y_{-L} and inside it Y_L :

$$Y_p = Y_{-L} + Y_L. \quad (A1)$$

Let the mask that can be used to obtain an image with a gap from the full image is denoted as L , and this mask is equal to 1 inside the gap and zero outside the gap.

Then expression (A1) can be written as

$$Y_p = Y_{-L} + LY_p. \quad (A2)$$

Let us find the spectrum (A2) and obtain

$$(1 - fL) * fY_p = fL_{-L}, \quad (A3)$$

where fL – is the spectrum of the mask L to obtain a gap; fY_p – full image spectrum; fL_{-L} is the spectrum of the image with a gap, and the sign (*) denotes the convolution operation. Solution (A3) can be produced iteratively.

Thus, the work of the method of interpolation of the sequentially calculated Fourier spectrum (IMSCS) is as follows:

1. Localize the gap, i.e. we determine the coordinates of all the pixels of the image that need to be filled using IMSCS.
2. Calculate the average brightness of the image using only reliably known pixels (without gap pixels). Thus, the zero harmonic of the spatial spectrum of the improved image is estimated.
3. Fill the gap with the brightness values calculated in the previous paragraph, that is, we get the first approximation of filling the gap. In this case, the undistorted part of the image (originally reliably known) does not undergo any changes.
4. Calculate the full spatial spectrum of the image obtained in the previous paragraph (with the gap filled).
5. Having limited the spectrum from the previous paragraph to zero and first harmonics, we calculate the second approximation of the brightness values to fill the gap.
6. Fill the gap with the brightness values calculated in the previous paragraph, and we get the second approximation of filling the gap. In this case, the undistorted part of the image (originally reliably known) does not undergo any changes.
7. Next, cycle through steps 4, 5, 6, each time sequentially, in step 5, increasing the number of harmonics in the spectrum to calculate the gap filling brightnesses by one, up to the highest possible. Thus, the gap is consistently filled, and the undistorted part of the image (originally known for certain) does not undergo any changes.

As a result of the proposed algorithm, the retouched gap is gradually filled with an image that is more and more consistent with the spectrum of the surrounding image (initially known for certain).

REFERENCES

1. Yeh S, Stark H. Iterative and one-step reconstruction from nonuniform samples by convex projections. *Journal of the Optical Society of America*, 1990, 7(3):491-499. DOI: 10.1364/JOSAA.7.000491
2. Stasiński R, Konrad J. POCS-based image reconstruction from irregularly-spaced samples. *Proceedings of the IEEE International*

- Conference on Image Processing (ICIP '00)*. September 2000, 2:315-318.
3. Park J, Park D-C, Marks RJ II, El-Sharkawi MA. Block loss recovery in DCT image encoding using POCS. *Proceedings of the IEEE International Symposium on Circuits and Systems*. September 2002, 5:245-248.
 4. Huang H, Makur A. A new iterative reconstruction scheme for signal reconstruction. *Proceedings of the IEEE Asia Pacific Conference on Circuits and Systems (APCCAS '08)*. December 2008, pp. 336-339.
 5. Ogawa T, Haseyama M. Adaptive reconstruction method of missing texture based on projection onto convex sets. *Proceedings of the IEEE International Conference on Acoustics, Speech and Signal Processing (ICASSP '07)*. April 2007, 1:697-700.
 6. Chen J, Zhang L, Luo J, Zhu Y. MRI reconstruction from 2D partial k-space using POCS algorithm. *Proceedings of the 3rd International Conference on Bioinformatics and Biomedical Engineering (ICBBE '09)*. June 2009, pp. 1-4.
 7. Feichtinger HG, Kozek W, Strohmer T. Reconstruction of signals from irregular samples of its short-time Fourier transform. *Proceedings of the SPIE: wavelet applications in signal and image processing III*. July 1995, San Diego, Calif, USA, pp. 140-150. DOI: 10.1117/12.217570.
 8. Guven HE, Ozaktas HM, Cetin AE, Barshan B. Signal recovery from partial fractional Fourier domain information and its applications. *IET Signal Processing*, 2008, 2(1):15-25. DOI: 10.1049/iet-spr:20070017.
 9. Serbes A, Durak L. Optimum signal and image recovery by the method of alternating projections in fractional Fourier domains. *Communications in Nonlinear Science and Numerical Simulation*, 2010, 15(3):675-689.
 10. Bazulin E.G., Sokolov D.M. Restoration of ultrasonic images of reflectors from incomplete data by recognition with compression. *Akusticheskiy Zhurnal*, 2019, 65(4):520-532. DOI: 10.1134/S0320791919040038 (in Russ.).
 11. Donoho DL. Compressed sensing. *IEEE Trans. Inform. Theory*, 2006:1289-1306.
 12. Foucart S, Rauhut H. *A mathematical introduction to compressive sensing*. Basel, Birkhauser, 2013, 585 p.
 13. Guameri GA, Pipa DR, Junior FN, deArruda L VR, Zibetti MVW. A sparse reconstruction algorithm for ultrasonic images in nondestructive testing. *Sensors*, 2015, 15:9324-9343.
 14. Gonzalez RC and Woods RE. *Digital Image Processing*. Prentice Hall, International Version 3rd Edition, NJ, 2012:1071.
 15. Kokoshkin AV, Korotkov VA, Korotkov KV, Novichikhin EP. Retouching and restoration of missing image fragments by means of the iterative calculation of their spectra. *Computer Optics*, 2019; 43(6):1030-1040. DOI: 10.18287/2412-6179-2019-43-6-1030-1040.
 16. Kokoshkin AV, Korotkov VA, Korotkov KV, Novichikhin EP. Using Fourier spectrum for retouching and restoration missing parts of the image which were deformed by instrumental function. *Zhurnal radioelektroniki [Journal of Radio Electronics] [online]*. 2016, №7, <http://jre.cplire.ru/jre/jul16/4/text.html>(in Russ.).
 17. Kokoshkin AV, Korotkov VA, Novichikhin EP. Reconstruction of Acoustic Signals According to Incomplete Data. *J. of Communications Technology and Electronics*, 2020, 65(12):1399-1406. DOI: 10.1134/S1064226920120104.
 18. Kokoshkin AV, Korotkov VA, Korotkov KV, Novichikhin EP. Comparison of objective methods of assessing quality of digital images. *Zhurnal radioelektroniki [Journal of Radio Electronics] [online]*. 2015, №6,

<http://jre.cplire.ru/jre/jun15/15/text.html>
(in Russ.).

19. Ashkenazy AV. *Spline surfaces. Fundamentals of the theory and computational algorithms*. Tver, Tver State University Publ., 2003, p. 82.
20. Nesterenko EA. The ability to use spline surfaces for constructing surfaces based on the results of shooting. *Journal of Mining Institute*, 2013, 204:127-133 (in Russ.).

DOI: 10.17725/rensit.2022.14.175

Numerical research of thermal changes influence to the ground in permafrost conditions

Maxim V. Muratov, Denis S. Konov, Igor B. Petrov

Moscow Institute of Physics and Technology, <https://mipt.ru/>

Dolgoprudny 141700, Moscow region, Russian Federation

E-mail: max.muratov@gmail.com, konov1999@gmail.com, petrov@mipt.ru

Received April 29, 2022, peer-reviewed May 6, 2022, accepted May 13, 2022

Abstract: The article is devoted to the numerical solution of the Stefan problem for studying the process of soil thawing in permafrost conditions. An enthalpy solution method was constructed, and the applicability of this method was considered. The numerical solution was found using the Pismen-Rekford scheme in 2D and 3D cases. The developed computational algorithms are parallelized for use on modern high performance computational systems. An approach has been implemented for modeling thermal processes in the thickness of an arbitrary array of substances, taking into account arbitrary initial conditions and environmental conditions. Mathematical modeling of the process of thawing of the upper layer of permafrost was carried out in two-dimensional and three-dimensional formulations, including the formulation with a gas reservoir located in the ground.

Keywords: mathematical modeling, permafrost, Stefan problem, enthalpy method, Pismen-Rekford scheme

UDC 004.94

Acknowledgments: The work was carried out within the framework of the Russian Science Foundation project No. 21-71-10015.

For citation: Maxim V. Muratov, Denis S. Konov, Igor B. Petrov. Numerical study of the effect of temperature changes on soil under permafrost conditions. *RENSIT: Radioelectronics. Nanosystems. Information Technologies*, 2022, 14(2):175-180e. DOI: 10.17725/rensit.2022.14.175.

CONTENTS

1. INTRODUCTION (175)
2. MATERIALS AND METHODS (176)
 - 2.1. MATHEMATICAL MODEL AND NUMERICAL METHOD (176)
 - 2.2. SOFTWARE IMPLEMENTATION (178)
3. THE RESULTS (178)
 - 3.1. FORMULATION OF THE PROBLEM (178)
 - 3.2. THE RESULTS OF MODELING THE THAWING OF FROZEN SOIL UNDER TEMPERATURE CHANGES IN THE TWO-DIMENSIONAL CASE (178)
 - 3.3. THE RESULTS OF MODELING THE THAWING OF FROZEN SOIL UNDER TEMPERATURE CHANGES IN THE THREE-DIMENSIONAL CASE (179)
4. CONCLUSION (179)
- References (180)

1. INTRODUCTION

In recent years, the Arctic coast of our country has been actively studied and developed. According to experts, the northern regions store colossal reserves of hydrocarbons that can be extracted. However, both production and exploration of deposits in this region has its own characteristics and specifics. One of the first problems that engineers face when studying soil in the northern regions is the presence of a layer of permafrost. Permafrost is a layer of soil, the temperature of which has not risen above 0°C for a long time (from 2-3 years to millennia). Groundwater in such areas are ice sheets. The thickness of the permafrost layer can reach more than 1000 m. In Russia, 60-70% of the territory is located in the

permafrost zone. Distribution zones - Eastern Siberia, Transbaikalia, northern regions near the coast of the Arctic Ocean.

A large number of natural and theoretical studies have been devoted to permafrost. The work [1] exhaustively describes permafrost, its properties and physical processes that occur in its thickness. In [2], the interaction between piles and permafrost is modeled. Also, one of the potential problems that threaten the safety of land exploitation in the permafrost zone are methane bombs.

This article proposes an approach to numerical modeling based on solving the problem of the evolution of a system with different phase states of matter and changing the location of the boundary between these phases – the Stefan problem [3-9]. Works [10-13] are devoted to the numerical solution of problems with phase transitions. In [10, 11], the method of lines was considered. The finite element method and finite difference methods are also often used in practice [12,13].

In this paper, we use the enthalpy approach [14], which has already been applied by the authors to solve the problem of melting an artificial ice island [15]. With its help, it was possible to obtain temperature distributions in the soil, as well as to simulate the process of its thawing.

2. MATERIALS AND METHODS

2.1. MATHEMATICAL MODEL AND NUMERICAL METHOD

Thermal processes in the soil in the permafrost zone cannot be modeled solely on the basis of the heat conduction equation. It is necessary to take into account melting, a phase transition that requires thermal energy. This can be done if we go to the Stefan problem, that is, set the problem of heat conduction for each phase and the boundary condition, the Stefan condition. Using the law of conservation of energy, Fourier's law of heat conduction, numbering all the phases with separate indexes i and denoting

the boundary between them $\Gamma(t)$ we arrive at the system:

$$\frac{\partial C_i^V T}{\partial t} = \bar{\nabla} \cdot (k_i \bar{\nabla} T), \quad \bar{r} \notin \Gamma(t),$$

$$\lambda^V \frac{\partial \bar{r}_\Gamma}{\partial t} \cdot \bar{dS} = (\bar{q}_L - \bar{q}_S) \cdot \bar{dS}, \quad \bar{r}_\Gamma \in \Gamma(t),$$

\bar{r} – radius vector, t – time, T – temperature field, \bar{q}_i – heat flow. By C_i^V , k_i , λ^V marked coefficients of heat capacity per unit volume, thermal conductivity and heat of phase transition, \bar{dS} – normal vector to the interface plane. At the boundary, the temperature is equal to the phase transition temperature T_p .

In general, thermophysical coefficients may depend on water saturation and soil type and may vary in space and time. For our tasks, we believe that the entire geological section can be divided into areas with constant values, where the type of soil and its water saturation does not change.

To go to specific characteristics (C_i , λ) we use formulas:

$$\rho_i C_i = C_i^V, \quad \rho_i \lambda = \lambda^V.$$

The coefficient k is effective and takes into account the heat exchange in the ground due to the mechanisms of heat conduction between solid particles, steam convection and other processes.

After adding boundary and initial conditions, the system becomes correct. But it is difficult to solve it in such a formulation. It is possible to formulate an equation for the entire region if we pass from temperature to heat content. We denote the heat content or enthalpy as H . The phase transition occurs in the range

$$C_s^V T_p = H_- < H < H_+ = C_s^V T_p + \lambda^V.$$

Then return to the temperature is possible with:

$$T = \begin{cases} \frac{H}{C_s^V}, & H < H_-, \\ T_p, & H_- < H < H_+, \\ \frac{H + (C_L^V - C_s^V) T_p - \lambda^V}{C_L^V}, & H > H_+. \end{cases}$$

It remains to determine the coefficient of thermal conductivity in the intermediate region:

$$k(H) = \begin{cases} k_s, & H < H_-, \\ k_s + (k_L - k_s) \cdot \frac{H - H_-}{H_+ - H_-}, & H_- < H < H_+, \\ k_L, & H > H_+. \end{cases}$$

Then for all interior points we arrive at the equation:

$$\frac{\partial C_i^V T}{\partial t} = \frac{\partial H}{\partial t} = \vec{\nabla} (k_i \vec{\nabla} T).$$

For the boundary, the right equality holds automatically (can be obtained from the continuity equation for heat). In total, taking into account the boundary conditions:

$$\begin{aligned} \frac{\partial H}{\partial t} &= \vec{\nabla}_r (k(H) \vec{\nabla}_r T(H)), \\ \left(\alpha T(H) + \beta \frac{\partial T(H)}{\partial n} \right) \Big|_{\partial \Omega} &= \gamma, \\ H(\vec{r}, t) \Big|_{t=0} &= H(T_0(\vec{r})). \end{aligned}$$

The system can be solved in one-dimensional, two-dimensional and three-dimensional form. To solve it numerically, it is necessary to pass to the grid function of heat content and rewrite the differential operators in the form of difference operators. The main difficulty here is the development of an efficient, that is, unconditionally stable method, with the algorithmic complexity of the transition to the next step in time linear in the total number of nodes; as well as the quasi-linear character of the equation.

It is proposed to switch to multilayer schemes, which are implicit in each of the fractional steps in only one direction. For each time step, carry out several iterations using the thermal conductivity coefficients from previous iterations. Then it is possible to solve linear equations by sweep at each iteration.

In the two-dimensional case, the Pismen-Rekford scheme is used (longitudinal-transverse scheme):

$$\frac{u_{ml}^{n+1/2} - u_{ml}^n}{\tau/2} = \Lambda_{xx} u_{ml}^{n+1/2} + \Lambda_{yy} u_{ml}^n,$$

$$\frac{u_{ml}^{n+1} - u_{ml}^{n+1/2}}{\tau/2} = \Lambda_{xx} u_{ml}^{n+1/2} + \Lambda_{yy} u_{ml}^{n+1}.$$

Differential operators (the value of k at fractional steps is chosen as the arithmetic mean):

$$\Lambda_{xx} u = k_{m+\frac{1}{2}l} \frac{u_{m+1l} - u_{ml}}{h_x^2} + k_{m-\frac{1}{2}l} \frac{u_{m-1l} - u_{ml}}{h_x^2},$$

$$\Lambda_{yy} u = k_{ml+\frac{1}{2}} \frac{u_{ml+1} - u_{ml}}{h_y^2} + k_{ml-\frac{1}{2}} \frac{u_{ml-1} - u_{ml}}{h_y^2}.$$

In the three-dimensional case, the Pismen-Rekford scheme is rewritten as:

$$\frac{u_{mlp}^{n+1/3} - u_{mlp}^n}{\tau/3} = a^2 \Lambda_{xx} u_{mlp}^{n+1/3} + a^2 \Lambda_{yy} u_{mlp}^n + a^2 \Lambda_{zz} u_{mlp}^n,$$

$$\frac{u_{mlp}^{n+2/3} - u_{mlp}^{n+1/3}}{\tau/3} = a^2 \Lambda_{xx} u_{mlp}^{n+1/3} + a^2 \Lambda_{yy} u_{mlp}^{n+2/3} + a^2 \Lambda_{zz} u_{mlp}^{n+1/3},$$

$$\frac{u_{mlp}^{n+1} - u_{mlp}^{n+2/3}}{\tau/3} = a^2 \Lambda_{xx} u_{mlp}^{n+2/3} + a^2 \Lambda_{yy} u_{mlp}^{n+1} + a^2 \Lambda_{zz} u_{mlp}^{n+1}.$$

Sustainability requires:

$$\frac{4\tau a^2}{h^2} \leq 1,$$

$$h = \min(h_x, h_y, h_z),$$

$$a = \sqrt{\max((\rho_i C_i)_q^{-1}) \cdot \max(k_j)_r}.$$

where i, j are indices of phase states, q, r are indices of substances.

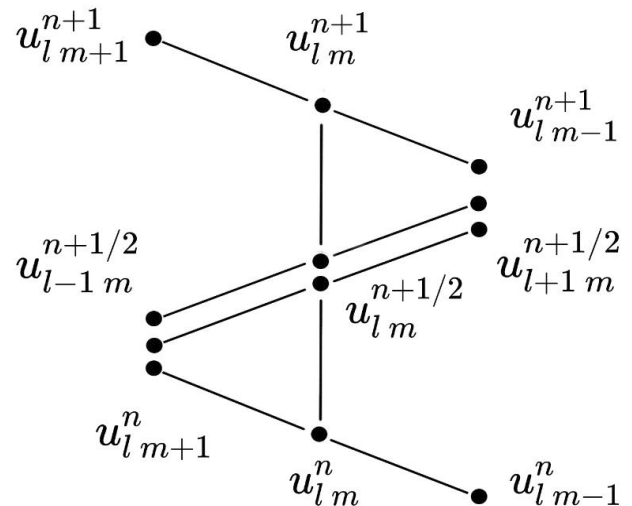


Fig. 1. Template of the Pismen-Rekford scheme.

2.2. SOFTWARE IMPLEMENTATION

The software developed on the basis of the mathematical model for solving the multidimensional Stefan problem in the enthalpy formulation can be divided into two groups. On the one hand, the main cycle with the transition between time layers is implemented in C++ using the OpenMP library to maximize performance. The initial and boundary conditions, the distribution of substances in the computational domain, and other parameters are transferred to the program from other files, which are generated separately using scripts in the slower, but more convenient for practical use, Python language.

The package of auxiliary programs includes scripts for generating a grid from geometric shapes, initial temperature distributions of their objects of complex shape, such as gradients, an XML file for the task configuration, and scripts for processing computation results.

The main program includes a module for parsing this data and a module for computation itself. It is possible to record intermediate results for further processing in VTK format files.

3. THE RESULTS

3.1. FORMULATION OF THE PROBLEM

Consider the structure of the soil, including peaty loam, loam and sand. The thermophysical characteristics of the layers [1] are given in **Table 1**.

The density of peaty loam is taken equal to $\rho = 1500 \text{ kg/m}^3$, loam $\rho = 1600 \text{ kg/m}^3$, sand $\rho = 1300 \text{ kg/m}^3$.

Schemes of the computational domain for studying the process of thawing the soil are shown in **Fig. 2**. Computations were carried out on two-dimensional (Fig. 2a) and three-dimensional (Fig. 2b) models.

Table 1

Physical characteristics of the soil

Substance	$C_s^V, \frac{kJ}{m^3 \cdot ^\circ C}$	$C_L^V, \frac{kJ}{m^3 \cdot ^\circ C}$	$\lambda, \frac{kJ}{kg}$	$k_s, \frac{W}{m \cdot ^\circ C}$	$k_L, \frac{W}{m \cdot ^\circ C}$
Peaty loam	2350	3150	71957	2.73	2.56
Loam	2350	3150	71957	1.7	1.51
Sand	1670	2010	60437	1.86	1.51

The index S denotes the frozen state, and L denotes the thawed one.

3.2. THE RESULTS OF MODELING THE THAWING OF FROZEN SOIL UNDER TEMPERATURE CHANGES IN THE TWO-DIMENSIONAL CASE

The nature of permafrost thawing for a small area (for example, under a structure or a pipeline with a constant positive temperature) was studied for the model presented in Fig. 2a. For all computations, the temperature of the upper boundary is assumed to be $+20^\circ\text{C}$. The boundary condition of zero heat flux is set on the side and lower boundaries. The results of computations are shown in **Fig. 3**.

Next, a soil with a gas cavity located at a depth of 3 m was considered (Fig. 2a). The results of the calculation for the thawing of this geological section are shown in **Fig. 4**.

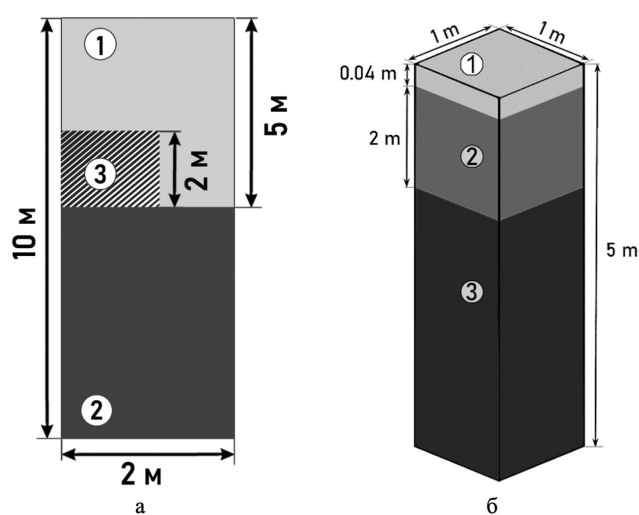


Fig. 2. Schemes of the computational domain for studying the process of soil freezing, a – two-dimensional model: 1 – peaty loam, 2 – loam, 3 – gas cavity. b – three-dimensional model: 1 – surface layer with air temperature, 2 – peaty loam, 3 – loam.

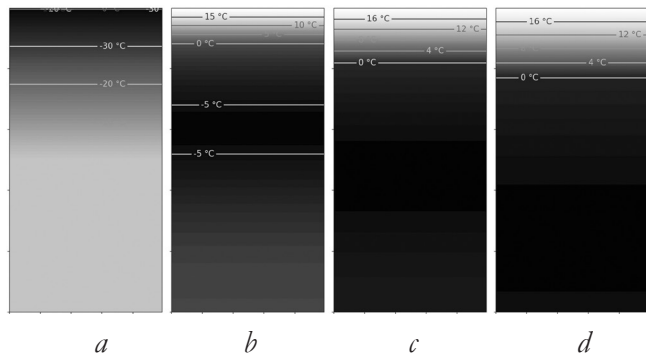


Fig. 3. Modeling results of the impact of seasonal air temperature changes on the soil on a two-dimensional model, thawing of the upper layer of permafrost, time points: a - initial moment, b - 45 days of positive temperature, c - 90 days of positive temperature: d - 135 days of positive temperature.

3.3. THE RESULTS OF MODELING THE THAWING OF FROZEN SOIL UNDER TEMPERATURE CHANGES IN THE THREE-DIMENSIONAL CASE

For the three-dimensional case, problems were solved in formulations similar to the two-dimensional case. The model of the geological section is shown in Fig. 2b. The case without a gas cavity was considered, the modeling results for which are shown in Fig. 5.

Fig. 6 shows the simulation results in the form of two-dimensional pictures on the plane of the vertical section of the temperature distribution

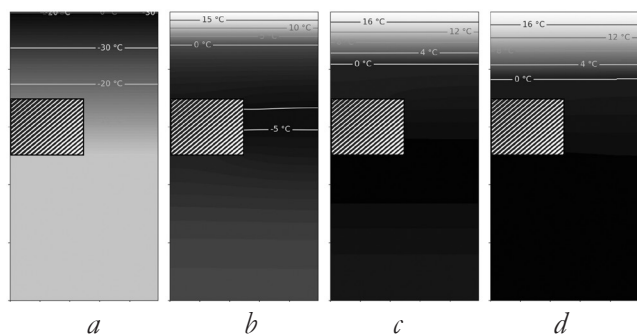


Fig. 4. Modeling results of the impact of seasonal air temperature changes on the soil with a gas reservoir on a two-dimensional model, thawing of the upper layer of permafrost, time points: a - initial moment, b - 45 days of positive temperature, c - 90 days of positive temperature: d - 135 days of positive temperature.

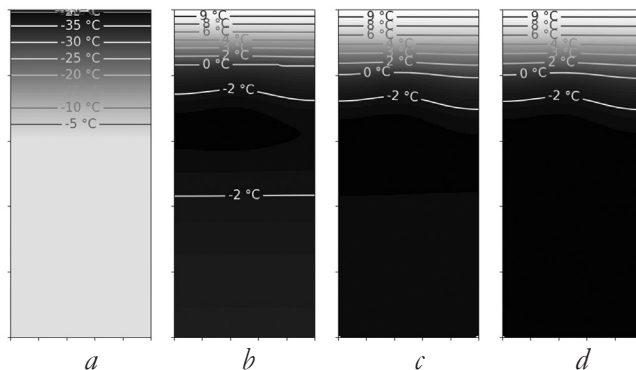


Fig. 5. Modeling results of the impact of seasonal air temperature changes on the soil on a three-dimensional model, thawing of the upper layer of permafrost, time points: a - initial moment, b - 45 days of positive temperature, c - 90 days of positive temperature: d - 135 days of positive temperature.

fields for the case of a geological section with a parallelepiped gas reservoir.

4. CONCLUSION

In this work, an enthalpy approach for solving the Stefan problem is developed, and software is developed for solving this problem in various formulations. On the basis of this program, numerical modeling of the thawing of the upper layer of permafrost was carried out and the temperature distribution in the frozen ground was found.

The logical continuation of this study is the solution of a thermoelastic problem for soil with

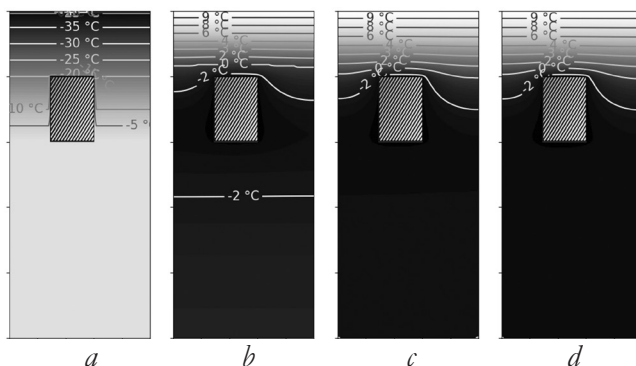


Fig. 6. Modeling results of the impact of seasonal air temperature changes on the soil with a gas reservoir on a three-dimensional model, thawing of the upper layer of permafrost, time points: a - initial moment, b - 45 days of positive temperature, c - 90 days of positive temperature: d - 135 days of positive temperature.

permafrost in order to study the resistance of upper layers to gas pressure in gaseous regions during seasonal thawing, as well as longer processes of temperature change, such as global warming.

REFERENCES

- Maslov AD, Osadchaya NV, Tumel GG, Shpolyanskaya NA. *Osnovy geokriologii: uchebnoe posobie* [Basics of geocryology: Tutorial]. Ukhta, Institute of Management, Information and Business, 2005.
- Vasiliev VI, Vasilieva MV, Grigoriev AV, Zakharov PE, Sivtsov PV, Stepanov SP. *Chislennoe modelirovanie protsessov teplo- i massoperenosa v keriolitozone* [Numerical modeling of thermos- and mass-transfer in cryolitozone]. Yakutsk, Izd. dom SVFU Publ., 2019.
- Albu AF, Zubov VI. Mathematical modeling and study of the process of solidification in metal casting. *Computational Mathematics and Mathematical Physics*, 2007, 47:843-862 (in Russ.).
- Albu AF, Zubov VI. Choosing a cost functional and a difference scheme in the optimal control of metal solidification. *Computational Mathematics and Mathematical Physics*, 2011, 51:21-34 (in Russ.).
- Biryukov VA, Miryakha VA, Petrov IB. Chislennoe modelirovanie trekhmernoi zadachi tayaniya iskusstvennogo ledyanogo ostrova entalpiinym metodom [Numerical modeling of artificial ice island melting 3D-problem by enthalpy method]. *4th vserossiyskaya konferentsiya s mezhdunarodnym uchatiem "Polyarnaya Mekhanika-2017"*, 2017, 81-86 (in Russ.).
- Jonsson T. On the one-dimensional Stefan problem with some numerical analysis Bachelor of Mathematics. *180hp Department of Mathematics and Mathematical Statistics*, 2013.
- White RE. An enthalpy formulation of the Stefan problem. *SIAM J. Numer. Anal.*, 1982, 19(6):1129-1157.
- White RE. A numerical solution of the enthalpy formulation of the Stefan problem. *SIAM J. Numer. Anal.*, 1982, 19(6):1158-1172.
- Samarskii AA. *Vvedenie v chislennyye metody* [Introduction in numerical methods]. Moscow, Nauka Publ., 1987.
- Vasil'ev FP. The method of straight lines for the solution of a one-phase problem of the Stefan type. *USSR Computational Mathematics and Mathematical Physics*, 1968, 8(1):81-101 (in Russ.).
- Bachelis RD, Mamelad VG, Schyaifer DB. Solution of Stefan's problem by the method of straight lines. *USSR Computational Mathematics and Mathematical Physics*, 1969, 9(3):113-126 (in Russ.).
- Budak BM, Solov'eva EN, Uspenskii AB. A difference method with coefficient smoothing for the solution of Stefan problems. *USSR Computational Mathematics and Mathematical Physics*, 1965, 5(5):59-76 (in Russ.).
- Dar'in NA, Mazhukin VI. Matematicheskoe modelirovanie zadachi Stefan ana adaptivnoi setke [Mathematical modeling of Stefan problem on adaptive mesh]. *Differentsial'nye uravneniya*, 1987, 23(7):1154-1160 (in Russ.).
- Buchko NA. *Entalpiinyi metod chislennogo resheniya zadach teploprovodnosti v promerzayuschikh ili protaivayuschikh gruntakh* [Enthalpy method for the numerical solution of heat conduction problems in freezing or thawing soils]. SPbGUNT IPT. http://refportal.com/upload/files/entalpiiny_metod_chislennogo_resheniya.pdf.
- Muratov MV, Biryukov VA, Konov DS, Petrov IB. Mathematical modeling of temperature changes impact on artificial ice islands. *RENSIT: Radioelectronics. Nanosystems. Information technologies*, 2021, 13(1):77-84. DOI: 10.17725/rensit.2021.13.077.

DOI: 10.17725/rensit.2022.14.181

Numerical exploration of models of geological media with methane cavities by the grid-characteristic method

Polina V. Stognii

Educational Scientific and Experimental Center of Moscow Institute of Physics and Technology, <https://kmipt.ru/>

Dolgoprudny 141700, Moscow region, Russian Federation

E-mail: stognii@phystech.edu

Nikolay I. Khokhlov, Igor B. Petrov

Scientific Research Institute for System Analysis of Russian Academy of Sciences, <https://www.niisi.ru/>
Moscow 117218, Russian Federation

E-mail: k_b@inbox.ru, petrov@mipt.ru

Received April 13, 2022, peer-reviewed April 20, 2022, accepted April 27, 2022

Abstract: A mathematical model of a homogeneous geological medium with methane cavities was developed. Based on the results of the calculations, wave patterns of the distribution of the velocity modulus in the models and seismograms of the recording of various velocity components on the receivers of reflected signals were obtained. The simulation results demonstrated the possibility of identifying the number of methane cavities by the waves reflected from them.

Keywords: seismic prospecting, methane cavities, grid-characteristic method

UDC 519.633.6

Acknowledgments: The study was financially supported by the Russian Foundation for Basic Research within the framework of scientific project No. 20-31-90034.

For citation: Polina V. Stognii, Nikolay I. Khokhlov, Igor B. Petrov. Numerical exploration of models of geological media with methane cavities by the grid-characteristic method. *RENSIT: Radioelectronics. Nanosystems. Information Technologies*, 2022, 14(2):181-186e. DOI: 10.17725/rensit.2022.14.181.

CONTENTS

1. INTRODUCTION (181)
 2. NUMERICAL METHOD (182)
 3. NUMERICAL SIMULATION RESULTS (183)
 4. CONCLUSION (184)
- REFERENCES (185)

1. INTRODUCTION

The study of problems, connected with the exploration of the Arctic region, is very actual today because of the active development of the hydrocarbon deposits in the Northern regions of our country [1]. The hydrocarbon deposits are usually located very deep into the soil, which makes

the process of their detection and further extraction rather difficult. One of the most effective ways of revealing hydrocarbons is seismic prospecting of geological areas [2]. While seismic prospecting of the examined area, geologists establish the signal source and a row of receivers on the surface of the investigated area. The impulse source sends seismic waves deep into the geological area, and the receivers detect the reflected waves from different heterogeneities, registering the velocities of the reflected waves. As a result, seismograms come to the receivers, which in future are being analyzed. The process of the real seismic works in the

area is rather difficult and not always effective because of many possible ways of interpreting seismograms. Therefore, the numerical modelling of the already explored area is conducted.

There are two ways of the numerical solution to the mentioned above problem. In the first case, the researchers solve the inverse problem or the incorrect problem of computing the characteristics of the medium based on the earlier collected seismograms. In the second case, the researchers solve the direct problem of calculating the velocities in the geological medium, including the problem of computing the meanings of velocities on the surface, imitating the signal receivers. The second formulation of the problem is solved more easily, though, demands more computations for observing different cases of the medium characteristics.

In this work we explore the problem of methane cavities detection in the Arctic conditions with the help of the numerical modelling of seismic waves spread in the heterogeneous media. Methane cavities are one of the variants of gas cavities, which are of great danger for the onshore buildings, sea ship, drilling rigs. The distinguishing characteristic of the methane layers is low density, which demands the particular approach to modelling. It is very important to be able to detect methane cavities in time and carry out their constant monitoring in order to take corresponding measures of safety in case, when methane starts rising towards the surface.

In this work we present the results of the numerical investigation of models with different numbers of methane cavities: models with three and four methane cavities.

We obtained the wave pictures of the velocity modulus spread and the seismograms of the recordings with the reflected waves from the methane cavities.

2. NUMERICAL METHOD

For describing the seismic waves spread in the geological medium, the system of equations for the linear-elastic medium was used [3]:

$$\begin{aligned} \rho \frac{\partial}{\partial t} \nu &= (\nabla \cdot \sigma)^T, \\ \frac{\partial}{\partial t} \sigma &= \lambda (\nabla \cdot \nu) I + \mu ((\nabla \times \nu) + (\nabla \times \nu)^T), \end{aligned} \quad (1)$$

where ρ is the density of the medium, ν is the speed of the seismic waves spread, σ is the Cauchy stress tensor, t is the time, λ and μ are the Lamé parameters, characterizing the medium characteristics, I is the unit tensor.

For solving the system (1), the grid-characteristic method [4] was used. For this, we present the system (1) in a view:

$$\frac{\partial q}{\partial t} + A_x \frac{\partial q}{\partial x} + A_y \frac{\partial q}{\partial y} = 0, \quad (2)$$

where vector $q = \{\sigma_{xx}, \sigma_{xy}, \sigma_{yy}, \nu_x, \nu_y\}$ matrices A_x and A_y consist of the coefficients of the system (1) and are of the following view:

$$A_x = \begin{vmatrix} 0 & 0 & -1/\rho & 0 & 0 \\ 0 & 0 & 0 & 0 & -1/\rho \\ -\lambda - 2\mu & 0 & 0 & 0 & 0 \\ 0 & -\lambda - 2\mu & 0 & 0 & 0 \\ 0 & -\mu & 0 & 0 & 0 \end{vmatrix}, \quad (3)$$

$$A_y = \begin{vmatrix} 0 & 0 & 0 & 0 & -1/\rho \\ 0 & 0 & 0 & -1/\rho & 0 \\ 0 & -\lambda & 0 & 0 & 0 \\ -\lambda & 0 & 0 & 0 & 0 \\ -\mu & 0 & 0 & 0 & 0 \end{vmatrix}.$$

Then, we apply the method of splitting across the space coordinates and obtain two 1D systems of equations:

$$\frac{\partial q}{\partial t} + A_i \frac{\partial q}{\partial i} = 0, \quad i = x, y. \quad (4)$$

Now, we examine the system (4) for the coordinate x :

$$\frac{\partial q}{\partial t} + A_x \frac{\partial q}{\partial x} = 0. \quad (5)$$

The system (5) is hyperbolic, then it can be presented as:

$$\frac{\partial q}{\partial t} + \Omega_x \Lambda_x \Omega_x^{-1} \frac{\partial q}{\partial x} = 0. \quad (6)$$

In (6) Ω_x is the matrix out of the eigen vectors of the matrix A_x , Λ_x is the diagonal matrix with the eigen values on the diagonal. The eigen values of the matrix A_x and matrix A_y are equal to $\{-c_p, c_p, -c_s, c_s, 0\}$, where c_p and c_s are the longitudinal and transverse velocities of the sound, correspondingly, which can be calculated using the formulas:

$$c_p = \sqrt{(\lambda + 2\mu) / \rho}, \quad c_s = \sqrt{\mu / \rho}. \quad (7)$$

Analogically, the system (1) for the coordinate y can be observed.

Then, we make the variable change $p = \Omega_x q$, after which the system (6) will look:

$$\frac{\partial p}{\partial t} + \Lambda_x \frac{\partial p}{\partial x} = 0. \quad (8)$$

The system (8) consists of five independent equations, each of which was solved using the Rusanov scheme of the third order of accuracy [5].

3. THE RESULTS OF THE NUMERICAL MODELLING

We conducted the numerical modelling of the seismic waves spread in models of

geological media with methane cavities. We observed three models: model with four methane cavities, model with three methane cavities and model without any methane cavities. The basic geological model with methane cavities was characterized by the following elastic properties: density – 2600 kg/m³, the longitudinal sound speed – 5000 m/s, the transverse sound speed – 3150 m/s.

The computational parameters were the following: the time step was equal to 10⁻⁴ s, the coordinate step was equal to 1 m. The influence was conducted with the help of the source of the Reiker impulse with the central frequency equal to 30 Hz, which was located on the surface of the models in the center of the computational area. In addition, the row of 40 receivers was situated on the surface of the models for detecting the reflected signals.

Fig. 1 presents the wave pictures of the seismic reflections from the methane cavities at time moment 0.3 s: in the left picture – for the model with three methane cavities, in the right picture – for the model with four methane cavities. The reflections of the seismic waves from each of the methane cavities can be detected in both wave pictures.

In **Fig. 2**, there are seismograms of the recordings of the reflected signals from the methane cavities on the receivers for different models. All the seismograms were collected after the subtraction the corresponding seismograms for the model without methane cavities. Figures 2a, 2b present the seismograms of the recordings of the V_x component of the velocity on the receivers, Figures 2c, 2d – the seismograms of the recordings of the V_y component

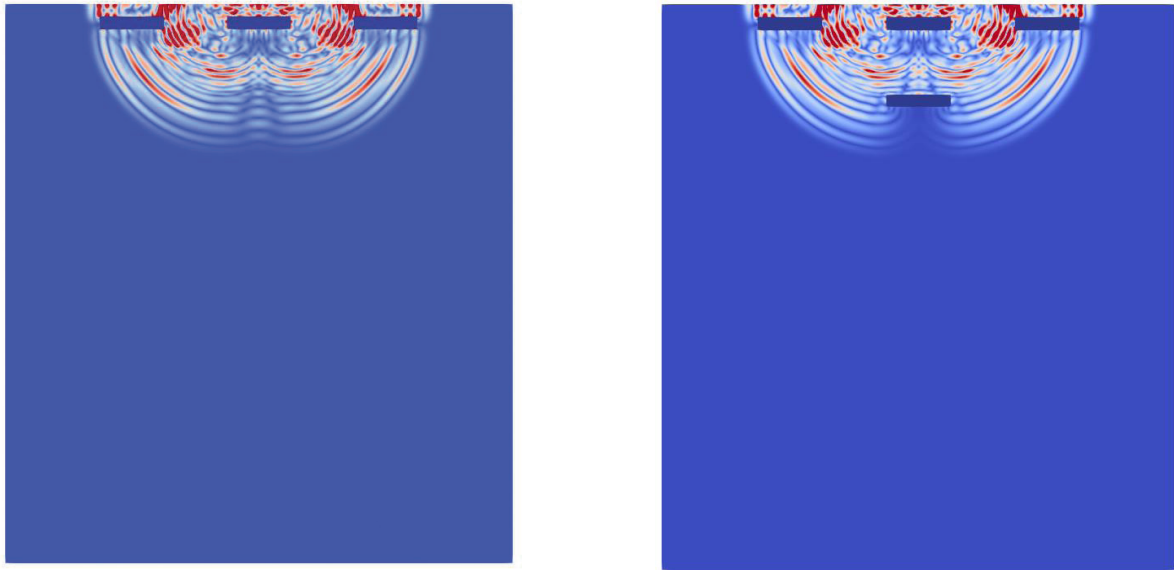


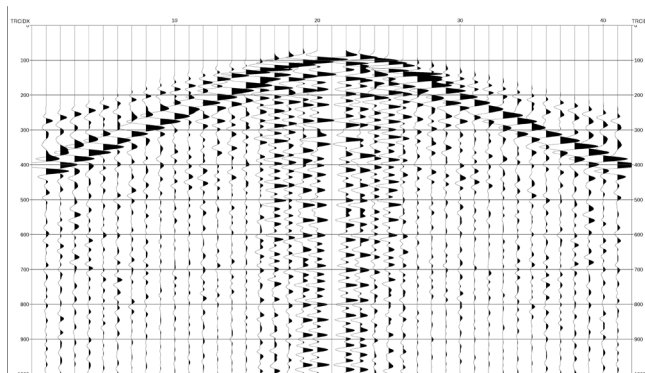
Fig. 1. Wave pictures of the velocity modulus distribution for the models with three and four methane cavities at time moment 0.3 s.

of the velocity on the receivers for the models with three and four methane cavities, correspondingly. The differences between the seismograms are present, but it is rather difficult to identify them. In Figures 2e, 2f the differences in the seismograms for the models with three and four methane cavities for the velocity components V_x and V_y are depicted, which are simpler for the interpretation and give

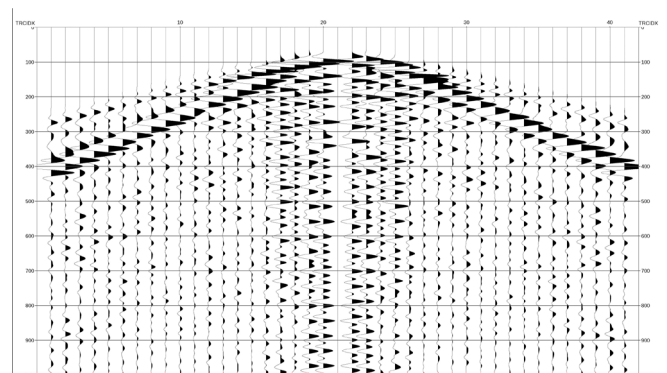
the opportunity to detect the differences between the models.

4. CONCLUSION

In this work we presented the results of the investigation of models with different numbers of the methane cavities: with three and four cavities. The wave pictures of the velocity modulus distribution in the models demonstrated the opportunity



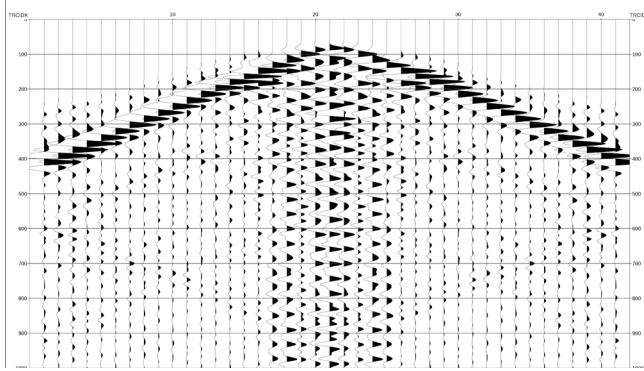
a



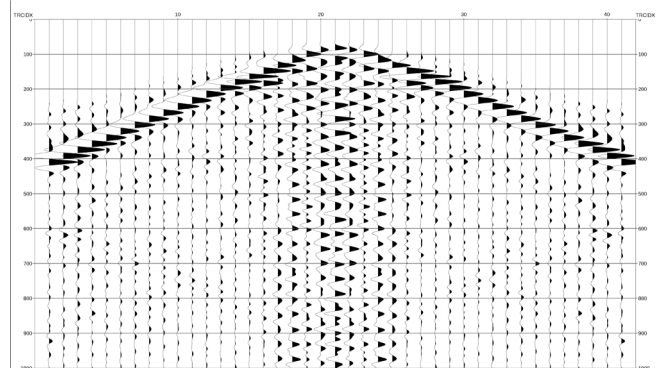
b

The seismogram of the recording of the X-component of the velocity for the model with 3 methane cavities

The seismogram of the recording of the X-component of the velocity for the model with 4 methane cavities



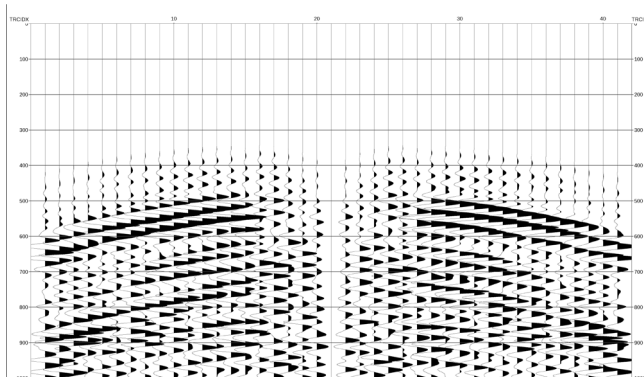
c



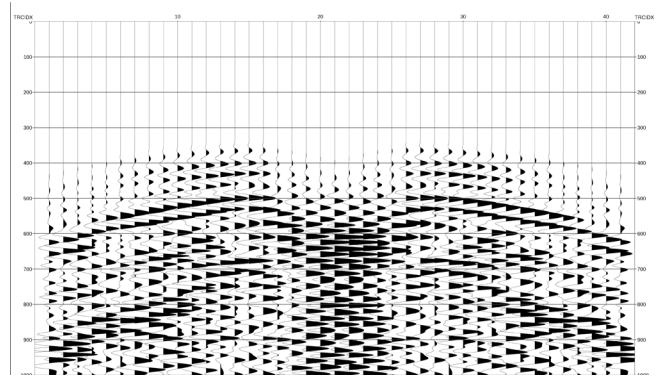
d

The seismogram of the recording of the Y-component of the velocity for the model with 3 methane cavities.

The seismogram of the recording of the Y-component of the velocity for the model with 4 methane cavities.



e



f

The seismogram of the difference of the X-component of the velocity between the models with 3 and 4 methane cavities.

The seismogram of the difference of the Y-component of the velocity between the models with 3 and 4 methane cavities.

Fig. 2. The seismograms of the recordings of different velocity components and anomalous seismograms (subtracting the seismograms for the model without methane cavities) of the recording of the reflected signals from the methane cavities on the receivers for the models with three and four methane cavities.

to identify the reflected waves from each methane cavity. The seismograms of the recordings of the reflected signals for the V_x , V_y velocity components in the models with three and four methane cavities showed the differences between the models, however, the differences of the seismograms for different models turned to be more informative and presentative by the differences between the models.

REFERENCES

1. Kontorovich AE, Epov MI, Burshtein LM, Kaminskii VD, Kurchikov AR, Malyshev NA, Prischepa OM, Safronov AF, Stupakova AV, Suprunenko OI. Geology and hydrocarbon resources of the continental shelf in Russian Arctic seas and the prospects of their development. *Russian Geology and Geophysics*, 2010, 51(1):3-11. DOI: 10.1016/j.rgg.2009.12.003.

2. Muratov MV, Petrov IB. Application of mathematical fracture models to simulation of exploration seismology problems by the grid-characteristic method. *Computer Research and Modeling*, 2019, 11(6):1077-1082.
3. Witold Nowacki. *Teoria Sprezystosci*. Warszawa, Panstwowe Wydawnictwo Naukowe, 1970, 872 p.
4. Kholodov AS. Chislennye metody resheniya uravnenii i sistem giperbolicheskogo tipa [Numerical methods of hyperbolic equations and equations systems solution]. *Entsiklopedia nizkoterperaturnoy plazmy (seria "B")*, vol. VII-1(2):91-103. Moscow, Yanus-k Publ., 2008 (in Russ.).
5. Khokhlov NI, Golubev VI. On the Class of Compact Grid-Characteristic Schemes. *Smart Modeling for Engineering Systems (Proc. Intern. Conf. "50 Years of the Development of Grid-Characteristic Method")*. 2019, p. 64-77. DOI: 10.1007/978-3-030-06228-6.

DOI: 10.17725/rensit.2022.14.187

Computer simulation of unsteady elastic stress waves in a console and a ten-storey building under fundamental influence in the form of a Heaviside function

^{1,2}Vyacheslav K. Musayev

¹Moscow State University of Civil Engineering, <https://mgsu.ru/>
Moscow 129337, Russian Federation

²Russian University of Transport, <https://www.miit.ru/>
Moscow 127994, Russian Federation

E-mail: musayev-vk@yandex.ru

Received February 14, 2022, peer-reviewed February 21, 2022, accepted March 1, 2022

Abstract: The aim of the work is to consider the problems of numerical simulation of seismic safety of a console and a ten-storey building with a base in the form of an elastic half-plane under non-stationary wave influences. Modeling of tasks of the transition period is an actual fundamental and applied scientific task. Methodology. To solve a two-dimensional plane dynamic problem of elasticity theory with initial and boundary conditions, the finite element method in displacements is used. Based on the finite element method in displacements, an algorithm and a set of programs have been developed for solving linear planar two-dimensional problems that allow solving problems with non-stationary wave effects on complex systems. The algorithmic language Fortran-90 was used in the development of the software package. **Результаты. Results.** The problem of the effect of a plane longitudinal wave in an elastic half-plane in the form of four trapezoids and in the form of two half-periods of a sinusoid is considered to assess the physical reliability and mathematical accuracy. A system of equations consisting of 8016008 unknowns is solved. The problem of the effect of a plane longitudinal elastic wave in the form of a Heaviside function on a console with a base (the ratio of width to height is one to ten) is considered. A system of equations consisting of 16016084 unknowns is solved. The problem of the effect of a plane longitudinal elastic wave in the form of a Heaviside function on a ten-storey building with a base in the form of a half-plane is considered. A system of equations consisting of 16202276 unknowns is solved. Contour stresses and components of the stress tensor are obtained in the characteristic areas of the problem under study. Based on the conducted research, the following conclusions can be drawn. Elastic contour stress on the sides of the console and a ten-story building are almost a mirror image of each other, that is, antisymmetric. The console and supporting structures of the building work like a beam during seismic action, that is, if there are tensile stresses on one side, then compressive stresses on the other. Bending waves mainly prevail on the contours of the console and supporting structures of the building under seismic influence.

Keywords: mathematical modeling, wave theory of seismic safety, seismic impact, fundamental impact, Heaviside function, verification of the numerical method, console, ten-storey building, elastic half-plane, contour stress, bending waves

UDC 539.3

For citation: Vyacheslav K. Musayev. Computer simulation of unsteady elastic stress waves in a console and a ten-storey building under fundamental influence in the form of a Heaviside function. *RENSIT: Radioelectronics. Nanosystems. Information technologies*, 2022, 14(2):187-196e. DOI: 10.17725/rensit.2022.14.187.

CONTENTS

- | | |
|--|--|
| <p>1. INTRODUCTION (188)</p> <p>2. PROBLEM STATEMENT (188)</p> | <p>3. DEVELOPMENT OF METHODOLOGY AND ALGORITHM (189)</p> <p>4. RESULTS (189)</p> |
|--|--|

4.1. MODELING OF IMPULSE PROPAGATION IN THE FORM OF FOUR TRAPEZOIDS IN AN ELASTIC HALF-PLANE (189)

4.2. SIMULATION OF PULSE PROPAGATION IN THE FORM OF TWO HALF-CYCLES OF A SINUSOID IN AN ELASTIC HALF-PLANE (190)

4.3. SEISMIC STRESS WAVES IN A CONSOLE WITH A BASE (191)

4.4. SEISMIC STRESS WAVES IN A TEN-STORY BUILDING WITH A FOUNDATION (193)

5. CONCLUSION (194)

REFERENCES (195)

1. INTRODUCTION

The aim of the work is to consider the problems of numerical modeling of the seismic safety of a cantilever and a ten-story building with a base in the form of an elastic half-plane under non-stationary wave actions. Modeling the problems of the transition period is an actual fundamental and applied scientific problem. In this work, to solve a two-dimensional plane dynamic problem of elasticity theory with initial and boundary conditions, the finite element method in displacements is used.

The formulation of some dynamic problems of the mechanics of a deformable solid body is given in [1-15].

Unique objects are subject to seismic impacts [6-7,12-15]. The safety of unique objects from seismic impacts is an urgent fundamental and applied scientific problem [6-7,12-15].

However, the reliability of stress waves in deformable bodies in published scientific papers is not presented enough for a correct assessment from the point of view of known knowledge about stress waves. On the other hand, due to scarce information about the seismic wave impact on the object under study, there may be different approaches and impact models [6-7,12-15].

In this paper, one of the approaches to solving the problem in the field of the wave theory of seismic safety is presented. Verification (physical reliability and mathematical accuracy) of the developed technique, algorithm and software package is considered in solving the problem of the propagation of plane longitudinal waves in the

form of four trapezoids and two half-periods of a sinusoid in an elastic half-plane.

A numerical solution is given to the problem of modeling non-stationary seismic waves in a cantilever (the ratio of width to height is one to ten) and a ten-story building with a base in the form of a half-plane.

Transient processes are very important for assessing the safety of complex technical systems. The main stress state is formed during a transient process, that is, a non-stationary wave process. Therefore, the development of a methodology, algorithm and a set of programs for solving the problem posed is an urgent scientific task [6-11,14].

The application of the considered numerical method, algorithm and software package in solving non-stationary wave problems in deformable bodies is given in the following works [6-11,14]. Verification (assessment of accuracy and reliability) of the considered numerical method, algorithm and software package is given in the following works [6-11].

2. PROBLEM STATEMENT

To solve the problem of modeling elastic non-stationary stress waves in deformable regions of complex shape, we consider a certain body in a rectangular Cartesian coordinate system XOY, which is subjected to a mechanical non-stationary impulse influence at the initial time $t = 0$ [1-4,6-7,14].

Let us assume that some body is made of a homogeneous isotropic material obeying Hooke's elastic law at small elastic deformations [1-4,6-7,14]. The exact equations of the two-dimensional (plane stress state) dynamic theory of elasticity have the following form [1-4,6-7,14]:

$$\begin{aligned} \frac{\partial \sigma_x}{\partial X} + \frac{\partial \tau_{xy}}{\partial Y} &= \rho \frac{\partial^2 u}{\partial t^2}, \\ \frac{\partial \tau_{yx}}{\partial X} + \frac{\partial \sigma_y}{\partial Y} &= \rho \frac{\partial^2 v}{\partial t^2}, \quad (x, y) \in \Gamma, \\ \sigma_x &= \rho C_p^2 \varepsilon_x + \rho (C_p^2 - 2C_s^2) \varepsilon_y, \\ \sigma_y &= \rho C_p^2 \varepsilon_y + \rho (C_p^2 - 2C_s^2) \varepsilon_x, \\ \tau_{xy} &= \rho C_s^2 \gamma_{xy}, \quad \varepsilon_x = \frac{\partial u}{\partial X}, \quad \varepsilon_y = \frac{\partial v}{\partial Y}, \\ \gamma_{xy} &= \frac{\partial u}{\partial Y} + \frac{\partial v}{\partial X}, \quad (x, y) \in (\Gamma \cup S), \end{aligned} \quad (1)$$

where: σ_x, σ_y and τ_{xy} are the components of the elastic stress tensor; ϵ_x, ϵ_y and γ_{xy} are the components of the elastic strain tensor; u and v are the components of the elastic displacement vector along the OX and OY axes, respectively; ρ is the density of the material; $C_p = \sqrt{\frac{E}{\rho(1-\nu^2)}}$ is the velocity of the longitudinal elastic wave; $C_s = \sqrt{\frac{E}{2\rho(1+\nu)}}$ is the velocity of the transverse elastic wave; ν is Poisson's ratio; E is the modulus of elasticity; $S (S_1 \cup S_2)$ – the boundary contour of the body G .

System (1) in the area occupied by the body Γ should be integrated under initial and boundary conditions [1-4,6-7,14].

3. DEVELOPMENT OF THE METHOD AND ALGORITHM

To solve a two-dimensional plane dynamic problem of elasticity theory with initial and boundary conditions (1), we use the finite element method in displacements [6-7,14].

Taking into account the definition of the stiffness matrix, the vector of inertia and the vector of external forces for the body Γ , we write down the approximate value of the equation of motion in the theory of elasticity [6-7,14]:

$$H\ddot{\Phi} + K\dot{\Phi} = R, \Phi|_{t=0} = \Phi_0, \dot{\Phi}|_{t=0} = \dot{\Phi}_0, \quad (2)$$

where: H is the diagonal matrix of inertia; K is the stiffness matrix; Φ is the vector of nodal elastic displacements; $\dot{\Phi}_0$ is the vector of nodal elastic displacement velocities; $\ddot{\Phi}$ is the nodal elastic accelerations vector; R is the vector of external nodal elastic forces.

To integrate equation (2) with a finite element version of the Galerkin method, we bring it to the following form [6-7,14]:

$$H \frac{d}{dt} \dot{\Phi} + K\dot{\Phi} = R, \frac{d}{dt} \Phi = \dot{\Phi}. \quad (3)$$

Integrating relation (3) over the time coordinate using the finite element version of the Galerkin method, we obtain an explicit two-layer scheme for internal and boundary nodal points [6-7,14]:

$$\dot{\Phi}_{i+1} = \dot{\Phi}_i + \Delta t H^{-1} (-K\dot{\Phi}_i + R_i), \quad (4)$$

$$\Phi_{i+1} = \Phi_i + \Delta t \dot{\Phi}_{i+1}.$$

The main relations of the finite element method in displacements are obtained using the

principle of possible displacements and the finite element version of the Galerkin method [6-7,14]. The general theory of numerical equations of mathematical physics requires for this the imposition of certain conditions on the ratio of steps along the time coordinate Δt and along the spatial coordinates, namely [6-7,14]:

$$\Delta t = k \frac{\min \Delta l_i}{C_p}, \quad (i = 1, 2, 3, \dots), \quad (5)$$

where Δl is the length of the side of the finite element.

The results of the numerical experiment showed that, at $k = 0.5$, the stability of the explicit two-layer scheme is ensured for internal and boundary nodal points on quasi-regular grids [6–7, 14].

For the area under study, which consists of materials with different physical properties, the minimum step along the time coordinate (5) is selected.

Based on the finite element method in displacements, a technique has been developed, an algorithm has been developed, and a set of programs has been compiled for solving two-dimensional wave problems of the dynamic theory of elasticity [6-7,14].

4. RESULTS

4.1. MODELING OF IMPULSE PROPAGATION IN THE FORM OF FOUR TRAPEZOIDS IN AN ELASTIC HALF-PLANE

The problem of the impact of a plane longitudinal wave in an elastic half-plane (**Fig. 1**) in the form of four trapezoids (**Fig. 2**) is considered to assess the physical reliability and mathematical accuracy [6-7,14]. The problem under study was first solved by

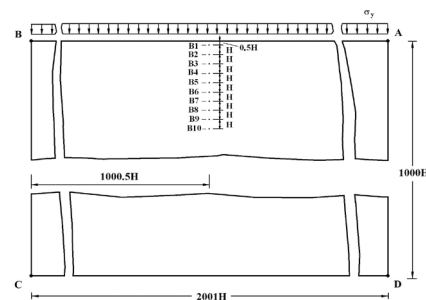


Fig. 1. Statement of the problem of the propagation of plane longitudinal waves in the form of four trapezoids in an elastic half-plane.

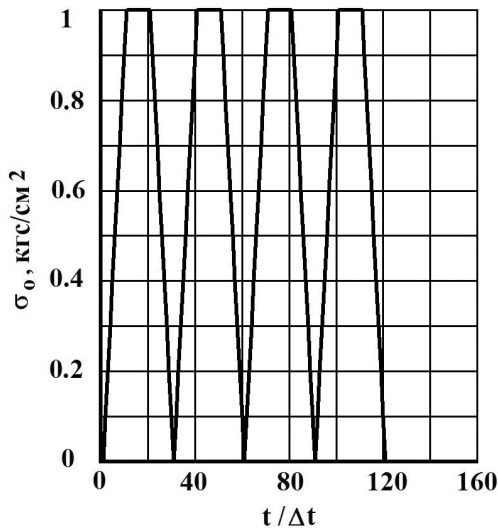


Fig. 2. Impulse action in the form of four trapezoids.

Musayev V.K. using the developed methodology, algorithm and software package [6-7,14].

Calculations were carried out with the following units of measurement: kilogram-force (kgf); centimeter (cm); second (s). For conversion to other units of measurement, the following assumptions were made: $1 \text{ kgf/cm}^2 \approx 0.1 \text{ MPa}$; $1 \text{ kgf}\cdot\text{s}^2/\text{cm}^4 \approx 10^9 \text{ kg/m}^3$.

At the boundary of the half-plane AB (Fig. 1), a normal stress σ_y is applied, which varies from $0 \leq n \leq 121$ ($n = t/\Delta t$) and the maximum value is P ($P = \sigma_0, \sigma_0 = -1 \text{ MPa}$ (-1 kgf/cm^2)). Boundary conditions for the BCDA contour at $t > 0$ $u = v = \dot{u} = \dot{v} = 0$. Reflected waves from the BCDA contour do not reach the studying points at $0 \leq n \leq 300$.

The calculations were carried out with the following initial data: $H = \Delta x = \Delta y$; $\Delta t = 1.862 \cdot 10^{-6} \text{ s}$; $E = 2.1 \cdot 10^5 \text{ MPa}$ ($2.1 \cdot 10^6 \text{ kgf/cm}^2$); $\nu = 0.3$; $\rho = 0.8 \cdot 10^4 \text{ kg/m}^3$ ($0.8 \cdot 10^{-5} \text{ kgf}\cdot\text{s}^2/\text{cm}^4$); $C_p = 5371 \text{ m/s}$; $C_s = 3177 \text{ m/s}$.

The computational domain under study has 2004002 nodal points. The system of equations is solved from 8016008 unknowns.

The calculation results were obtained at characteristic points $B1 - B10$ (Fig. 1).

As an example in Fig. 3 shows the change in the normal stress $\bar{\sigma}_y$ ($\bar{\sigma}_y = \sigma_y / |\sigma_0|$) (Fig. 2) in time n at point $B1$ (1 – numerical solution; 2 – analytical solution).

In this case, we can use the conditions at the front of a plane wave, which are described in [2]. For a

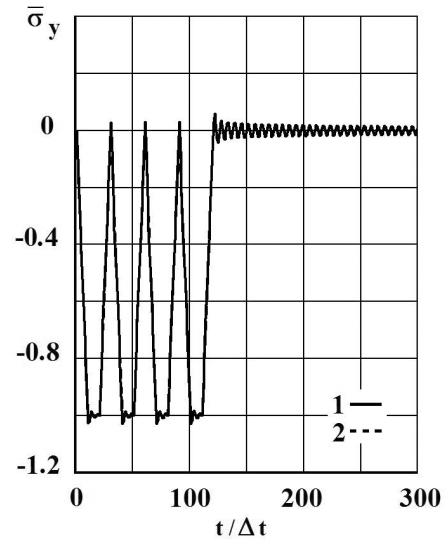


Fig. 3. Variation of the elastic normal voltages $\bar{\sigma}_y$ (the problem of the propagation of plane longitudinal waves in the form of four trapezoids in an elastic half-plane) in time $t/\Delta t$ at point $B1$: 1 – numerical solution; 2 – analytical solution.

plane stress state at the front of a plane longitudinal wave, there are the following analytical dependences $\sigma_y = -|\sigma_0|$.

Hence we see that the exact solution of the problem corresponds to the influence σ_0 (Fig. 2).

4.2. SIMULATION OF PULSE PROPAGATION IN THE FORM OF TWO HALF-CYCLES OF A SINUSOID IN AN ELASTIC HALF-PLANE

The problem of modeling plane waves in an elastic half-plane (Fig. 1) in the form of two half-periods of a sinusoid (Fig. 4) is considered.

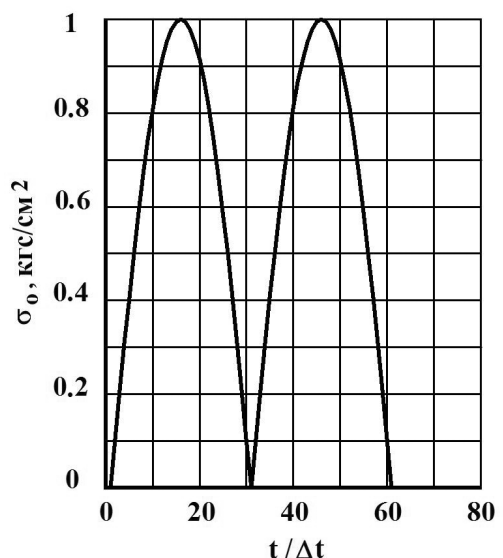


Fig. 4. Impact in the form of two half-cycles of a sinusoid.

Calculations were carried out with the following units of measurement: kilogram-force (kgf); centimeter (cm); second (s). For conversion to other units of measurement, the following assumptions were made: $1 \text{ kgf/cm}^2 \approx 0.1 \text{ MPa}$; $1 \text{ kgf}\cdot\text{s}^2/\text{cm}^4 \approx 10^9 \text{ kg/m}^3$.

The problem is solved to assess the physical reliability and mathematical accuracy of the considered numerical method [6-7,14]. The problem under study was first solved by Musaev V.K. using the developed methodology, algorithm and software package [6-7,14].

At the boundary of the half-plane AB (Fig. 1), a normal stress σ_y is applied, which varies from $0 \leq n \leq 61$ ($n = t/\Delta t$) and the maximum value is P ($P = \sigma_0$, $\sigma_0 = -0.1 \text{ MPa}$ (-1 kgf/cm^2)). Boundary conditions for the BCDA contour at $t > 0$. Reflected waves from the BCDA contour do not reach the points under study at $0 \leq n \leq 200$.

The calculations were carried out with the following initial data: $H = \Delta x = \Delta y$; $\Delta t = 1.862 \cdot 10^{-6} \text{ s}$; $E = 2.1 \cdot 10^5 \text{ MPa}$ ($2.1 \cdot 10^6 \text{ kgf/cm}^2$); $\nu = 0.3$; $\rho = 0.8 \cdot 10^4 \text{ kg/m}^3$ ($0.8 \cdot 10^5 \text{ kgf}\cdot\text{s}^2/\text{cm}^4$); $C_p = 5371 \text{ m/s}$; $C_s = 3177 \text{ m/s}$.

The system of equations is solved from 8016008 unknowns.

The calculation results were obtained at characteristic points B1 – B10 (Fig. 1).

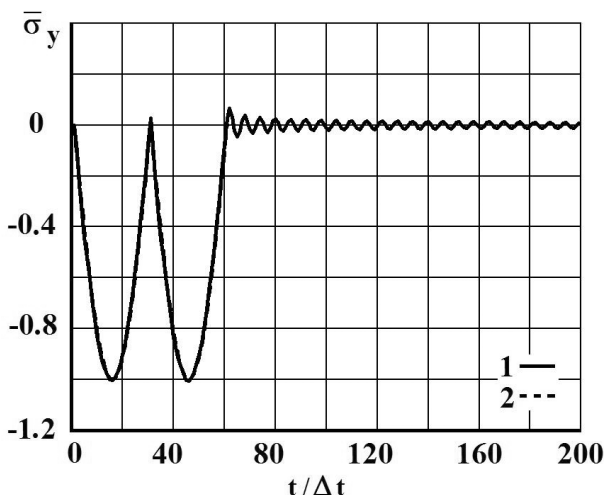


Fig. 5. Change of elastic normal voltages $\bar{\sigma}_y$ (problem of propagation of plane longitudinal waves in the form of two half-cycles of a sinusoid in an elastic half-plane) in time $t/\Delta t$ at point B1: 1 – numerical solution; 2 – analytical solution.

As an example in Fig. 5 shows the change in the normal stress $\bar{\sigma}_y$ ($\bar{\sigma}_y = \sigma_y / |\sigma_0|$) (Fig. 4) in time n at point B1 (1 – numerical solution; 2 – analytical solution).

In this case, one can use the conditions at the front of a plane wave, which are described in [2]. At the front of a plane longitudinal wave, there are the following analytical dependences for a plane stress state $\sigma_y = -|\sigma_0|$. Hence, we see that the exact solution of the problem corresponds to the action σ_0 (Fig. 4).

4.3. SEISMIC STRESS WAVES IN A CONSOLE WITH A BASE

The problem of the impact of a plane longitudinal non-stationary seismic wave on the cantilever (the ratio of width to height is one to ten) in an elastic half-plane (Fig. 6) in the form of a Heaviside function (Fig. 7) is considered.

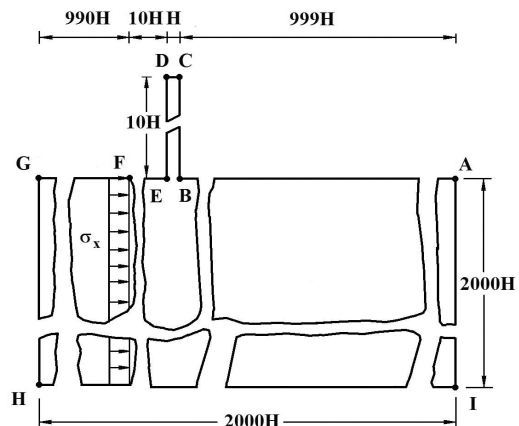


Fig. 6. Statement of the problem for the console (the ratio of width to height is one to ten) with an elastic base (half-plane).

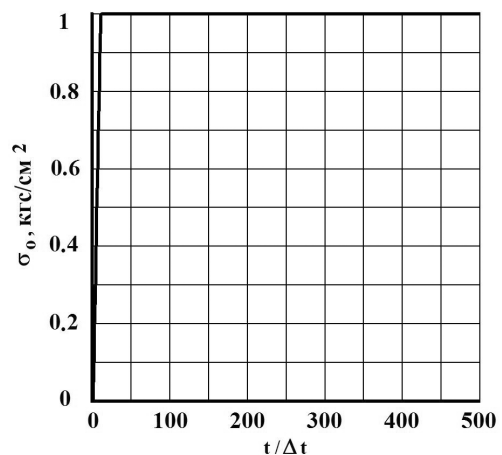


Fig. 7. Impulse influence in the form of a Heaviside function.

The problem under study was first solved by Musayev V.K. using the developed methodology, algorithm and software package [6-7,14].

Calculations were carried out with the following units of measurement: kilogram-force (kgf); centimeter (cm); second (s). For conversion to other units of measurement, the following assumptions were made: $1 \text{ kgf/cm}^2 \approx 0.1 \text{ MPa}$; $1 \text{ kgf}\cdot\text{s}^2/\text{cm}^4 \approx 10^9 \text{ kg/m}^3$.

The initial conditions are assumed to be zero. From point *F* parallel to the free surface *ABEFG*, a normal stress σ_x is applied, which at $0 \leq n \leq 11$ ($n = t/\Delta t$) changes linearly from 0 to *P*, and at $n \geq 11$ it is equal to *P* ($P = \sigma_0$, $\sigma_0 = 0.1 \text{ MPa}$ (1 kgf/cm^2)). The calculations were carried out with the following initial data: $H = \Delta x = \Delta y$; $\Delta t = 1.393 \cdot 10^{-6} \text{ s}$; $E = 3.15 \cdot 10^4 \text{ MPa}$ ($3.15 \cdot 10^5 \text{ kgf/cm}^2$); $\nu = 0.2$; $\rho = 0.255 \cdot 10^4 \text{ kg/m}^3$ ($0.255 \cdot 10^5 \text{ kgf}\cdot\text{s}^2/\text{cm}^4$); $C_p = 3587 \text{ m/s}$; $C_s = 2269 \text{ m/s}$.

Boundary conditions for the *GHIA* contour at $t > 0$, $u = v = \dot{u} = \dot{v} = 0$. Reflected waves from the *GHIA* contour do not reach the points under study at $0 \leq n \leq 500$. The *ABCDEFGH* contour is free from loads, except for point *F*.

The system of equations is solved from 16016084 unknowns.

On Fig. 9-13 shows the change in the loop stresses in the console (Fig. 8) in time $t/\Delta t$.

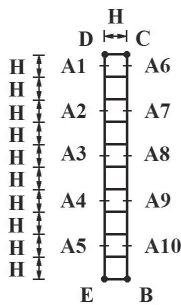


Fig. 8. Points at which contour stresses were obtained in the console.

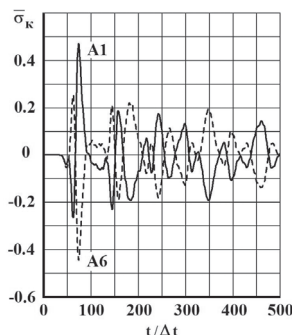


Fig. 9. Change in the elastic contour stresses $\bar{\sigma}_k$ at points *A1* and *A6* on the console contour in time $t/\Delta t$.

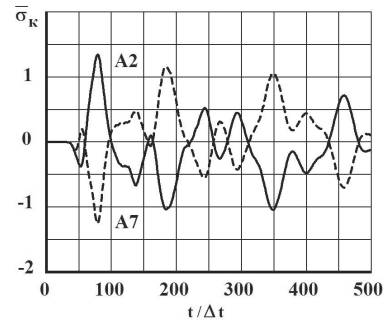


Fig. 10. Change in the elastic contour stresses $\bar{\sigma}_k$ at points *A2* and *A7* on the console contour in time $t/\Delta t$.

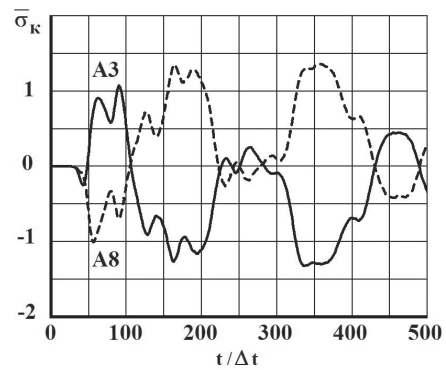


Fig. 11. Change in the elastic contour stresses $\bar{\sigma}_k$ at points *A3* and *A8* on the console contour in time $t/\Delta t$.

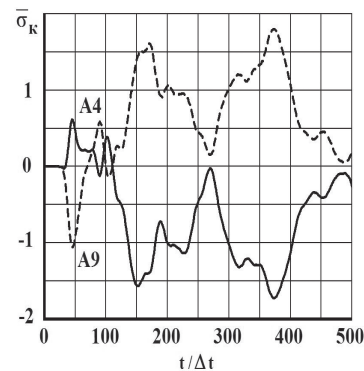


Fig. 12. Change in the elastic contour stresses $\bar{\sigma}_k$ at points *A4* and *A9* on the console contour in time $t/\Delta t$.

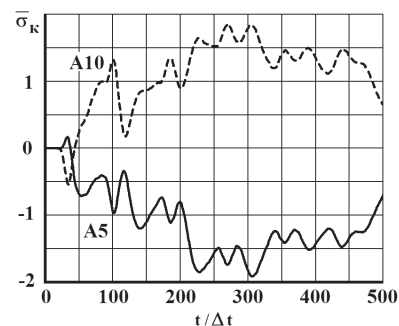


Fig. 13. Change in the elastic contour stresses $\bar{\sigma}_k$ at points *A5* and *A10* on the console contour in time $t/\Delta t$.

4.4. SEISMIC STRESS WAVES IN A TEN-STOREY BUILDING WITH A FOUNDATION

The problem of the influence of a plane longitudinal non-stationary seismic wave on a ten-storey building in an elastic half-plane (Fig. 14) in the form of a Heaviside function (Fig. 15) is considered.

The problem under study was first solved by Musayev V.K. using the developed methodology, algorithm and software package [6-7,14].

Calculations were carried out with the following units of measurement: kilogram-force (kgf); centimeter (cm); second (s). For conversion to other units of measurement, the following assumptions were made: $1 \text{ kgf/cm}^2 \approx 0.1 \text{ MPa}$; $1 \text{ kgf}\cdot\text{s}^2/\text{cm}^4 \approx 10^9 \text{ kg/m}^3$.

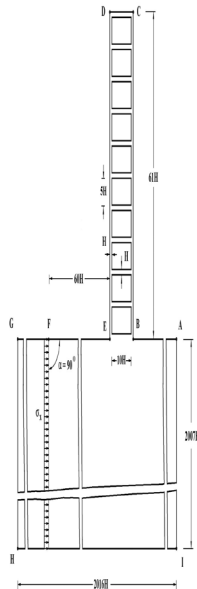


Fig. 14. Statement of the problem for a ten-storey building with an elastic foundation (half-plane).

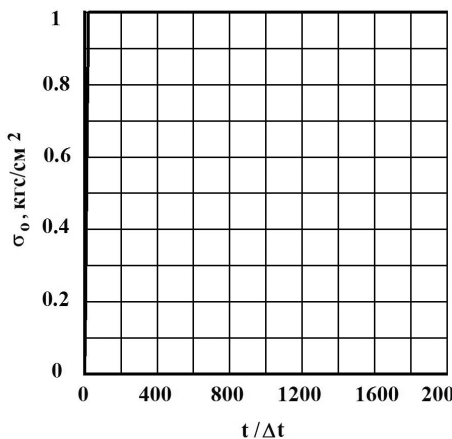


Fig. 15. Impulse influence in the form of a Heaviside function.

The initial conditions are assumed to be zero. From point F parallel to the free surface $ABEFG$, a normal stress σ_x is applied, which at $0 \leq n \leq 11$ ($n = t/\Delta t$) changes linearly from 0 to P , and at $n \geq 11$ it is equal to P ($P = \sigma_0$, $\sigma_0 = 0.1 \text{ MPa}$ (1 kgf/cm^2)). The calculations were carried out with the following initial data: $H = \Delta x = \Delta y$; $\Delta t = 1.393 \cdot 10^{-6} \text{ s}$; $E = 3.15 \cdot 10^4 \text{ MPa}$ ($3.15 \cdot 10^5 \text{ kgf/cm}^2$); $\nu = 0.2$; $\rho = 0.255 \cdot 10^4 \text{ kg/m}^3$ ($0.255 \cdot 10^5 \text{ kgf}\cdot\text{s}^2/\text{cm}^4$); $C_p = 3587 \text{ m/s}$; $C_s = 2269 \text{ m/s}$.

Boundary conditions for the $GHIA$ contour at $t > 0$, $u = v = \dot{u} = \dot{v} = 0$. Reflected waves from the $GHIA$ contour do not reach the points under study at $0 \leq n \leq 2000$.

The contour $ABCDEFG$ is free from loads, except for point F . The system of equations is solved from 16202276 unknowns. On Fig. 17-21 shows the change in the loop stresses $\bar{\sigma}_k$ in the console (Fig. 16) in time $t/\Delta t$.

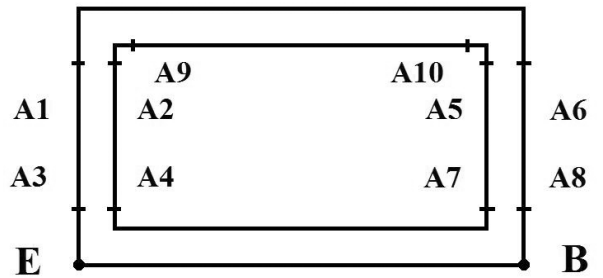


Fig. 16. Points at which contour stresses were obtained in the console.

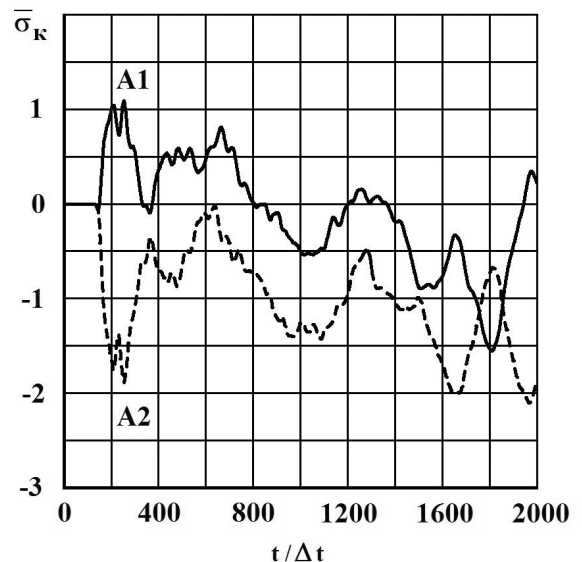


Fig. 17. Change in the elastic contour stresses $\bar{\sigma}_k$ at points $A1$ and $A2$ on the console contour in time $t/\Delta t$.

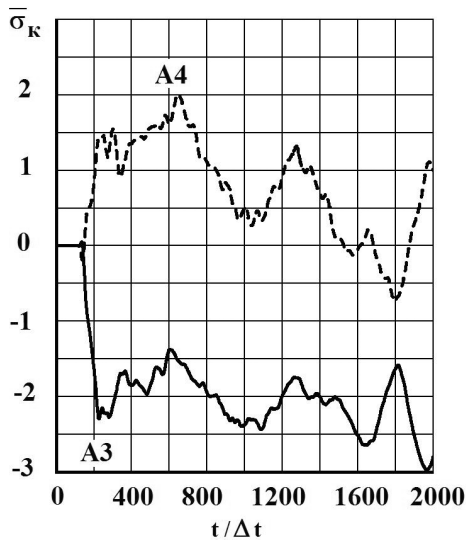


Fig. 18. Change in the elastic contour stresses $\bar{\sigma}_k$ at points A3 and A4 on the console contour in time $t/\Delta t$.

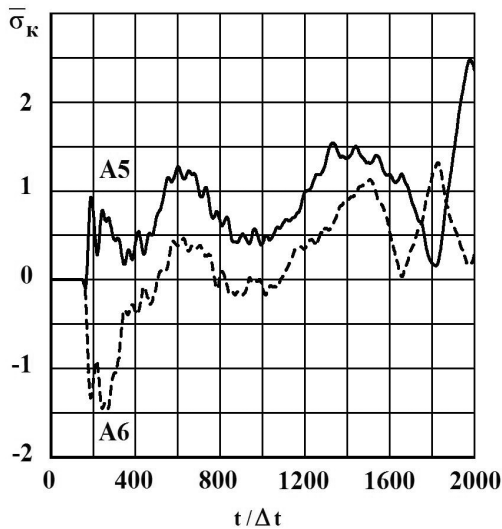


Fig. 19. Change in the elastic contour stresses $\bar{\sigma}_k$ at points A5 and A6 on the console contour in time $t/\Delta t$.

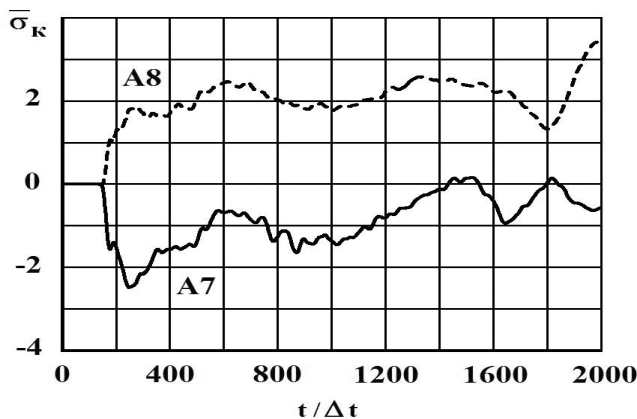


Рис. 20. Change in the elastic contour stresses $\bar{\sigma}_k$ at points A7 and A8 on the console contour in time $t/\Delta t$.

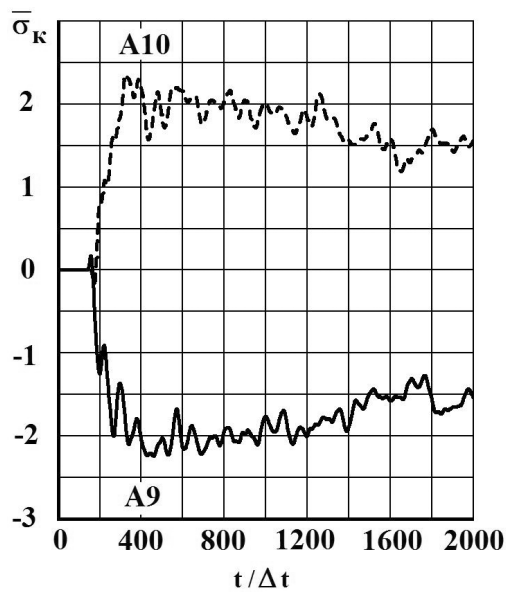


Fig. 21. Change in the elastic contour stresses $\bar{\sigma}_k$ at points A9 and A10 on the console contour in time $t/\Delta t$.

4. CONCLUSION

On the basis of mathematical modeling (finite element method), a technique, an algorithm and a set of programs for solving linear two-dimensional plane problems have been developed, which allow solving complex problems with non-stationary wave effects.

The main relations of the finite element method are obtained using the principle of possible displacements. The elasticity matrix is expressed in terms of P-wave velocity, S-wave velocity, and density. A linear dynamic problem with initial and boundary conditions in the form of partial differential equations, for solving problems under wave influences, using the finite element method, is reduced to a system of linear ordinary differential equations with initial conditions, which is solved by an explicit two-layer scheme.

To predict the seismic safety of an object, with non-stationary wave effects, numerical modeling of the equations of the wave theory of elasticity is used.

The problem of the impact of a plane longitudinal wave in the form of four trapezoids and two half-periods of a sinusoid on an elastic half-plane is solved. The system of equations from 8016008 unknowns is solved. A comparison was

made with the results of the analytical solution, which showed a quantitative match.

The problem of mathematical modeling of non-stationary elastic stresses waves in the console (the ratio of width to height is one to ten) with an elastic half-plane under seismic influence is solved. The system of equations from 16016084 unknowns is solved.

The problem of mathematical modeling of non-stationary elastic stresses waves in a ten-story building with an elastic half-plane under seismic influence is solved. The system of equations is solved from 16202276 unknowns.

The elastic contour tensions on the edges of the console and the ten-story building is almost a mirror image of one another, that is, antisymmetric. A console and a ten-story building under seismic influence work like a beam, that is, if there are tensile influences on one side, then compressive influences on the other. On the contours of the console and the ten-story building under seismic influence, bending waves mainly prevail.

REFERENCES

1. Davis R. *Tension Waves in Solids*. Moscow, Inostrannaya literatura Publ., 1961, 104 p.
2. Timoshenko SP, Goodier D. *Theory of elasticity*. Moscow, Nauka Publ., 1975, 576 p.
3. Ionov VI, Ogibalov PM. *Stresses in bodies under impulsive loading*. Moscow, Vysshaya shkola Publ., 1975, 464 p.
4. Bate K, Wilson E. *Numerical methods of analysis and finite element method*. Moscow, Stroyizdat Publ., 1982, 448 p.
5. Nemchinov VV. Numerical methods for solving flat dynamic elasticity problems. *International Journal for Computational Civil and Structural Engineering*, 2013, 9(1):90-97.
6. Musayev VK. Estimation of accuracy of the results of numerical simulation of unsteady wave of the stress in deformable objects of complex shape. *International Journal for Computational Civil and Structural Engineering*, 2015, 11(1):135-146.
7. Musayev VK. On the mathematical modeling of nonstationary elastic waves stresses in corroborated by the round hole. *International Journal for Computational Civil and Structural Engineering*, 2015, 11(1):147-156.
8. Dikova EV. Reliability of the numerical method, algorithm and software package Musayeva V.K. when solving the problem of the propagation of plane longitudinal elastic waves (the ascending part is linear, the descending part is a quarter of a circle) in a half-plane. *International Journal of Experiential Education*, 2016, 12-3:354-357.
9. Starodubtsev VV, Akatiev SV, Musayev AV, Shiyarov SM, Kurantsov OV. Modelirovanie uprugikh voln v vide impul'snogo vozdeystviya (voskhodyashchaya chast' - chetvert' kruga, niskhodyashchaya chast' - chetvert' kruga) v poluploskosti s pomoshch'yu chislennogo metoda Musayeva V.K. [Modeling of elastic waves in the form of impulse action (ascending part - a quarter of a circle, descending part - a quarter of a circle) in a half-plane using the numerical method Musayeva V.K.]. *Problemy bezopasnosti rossiyskogo obshchestva*, 2017, 1:36-40 (in Russ.).
10. Starodubtsev VV, Akatiev SV, Musayev AV, Shiyarov SM, Kurantsov OV. Modelirovanie c pomoshch'yu chislennogo metoda Musayeva V.K. nestatsionarnykh uprugikh voln v vide impul'snogo vozdeystviya (voskhodyashchaya chast' - chetvert' kruga, srednyaya - gorizontal'naya, niskhodyashchaya chast' - lineynaya) v sploshnoy deformiruemyoy srede [Modeling using the numerical method Musayeva V.K. non-stationary elastic waves in the form of impulsive action (the ascending part is a quarter of a circle, the middle part is horizontal, the descending part is linear) in a continuous deformable medium]. *Problemy bezopasnosti rossiyskogo obshchestva*, 2017, 1:63-68 (in Russ.).
11. Kurantsov VA, Starodubtsev VV, Musayev AV, Samoilov SN, Kuznetsov ME. Modelirovanie impul'sa (pervaya vetv': voskhodyashchaya chast' - chetvert' kruga, niskhodyashchaya chast' - lineynaya; vtoraya vetv': treugol'nik) v uprugoy poluploskosti s pomoshch'yu chislennogo metoda Musayeva V.K. [Simulation of an impulse (first branch:

- ascending part - a quarter of a circle, descending part - linear; second branch: triangle) in an elastic half-plane using the numerical method Musayev V.K.]. *Problemy bezopasnosti rossiyskogo obshchestva*, 2017, 2:51-55 (in Russ.).
12. Favorskaya AV, Petrov IB. Calculation of seismic resistance of various structures by the grid-characteristic method. *RENSIT: Radioelectronics. Nanosystems. Information Technologies*, 2019, 11(3):345-350. DOI: 10.17725/rensit.2019.11.345.
 13. Avershyeva AV, Kuznetsov SV. Numerical simulation of Lamb wave propagation isotropic layer. *International Journal for Computational Civil and Structural Engineering*, 2019, 15(2):14-23.
 14. Musayev VK. Mathematical modeling of non-stationary elastic waves stresses under a concentrated vertical exposure in the form of delta functions on the surface of the half-plane (Lamb problem). *International Journal for Computational Civil and Structural Engineering*, 2019, 15(2):111-124.
 15. Bratov VA, Ilyashenko AV, Kuznetsov SV, Lin NK, Morozov NF. Homogeneous horizontal and vertical seismic barriers: mathematical foundations and dimensional analysis. *Materials Physics and Mechanics*, 2020, 44(1):61-65.

DOI: 10.17725/rensit.2022.14.197

Holographic Processing of Moving Sources in a Shallow Sea with Intense Internal Waves

Venedikt M. Kuz'kin

Prokhorov Institute of General Physics of RAS, <http://www.gpi.ru/>

Moscow 119991, Russian Federation

E-mail: kumiov@yandex.ru

Sergey A. Pereselkov, Elena S. Kaznacheeva, Sergey A. Tkachenko, Pavel V. Rybyanets

Voronezh State University, <http://www.vsu.ru/>

Voronezh 394006, Russian Federation

E-mail: pereselkov@yandex.ru, elna.kaznacheeva@yandex.ru, sega-tb@mail.ru, rybyanets.edu@yandex.ru

Vladimir I. Grachev

Kotelnikov Institute of Radioengineering and Electronics of RAS, <http://www.cplire.ru/>

Moscow 125009, Russian Federation

E-mail: grachev@cplire.ru

Received May 4, 2022; peer-reviewed May 11, 2022; accepted May 18, 2022

Abstract: In a shallow water area for two frequency ranges, on the basis of numerical simulation, the influence of intense internal waves that cause the interaction of sound field modes on the formation of an interferogram and a hologram of a moving source is considered. On the hologram, the spectral densities of the source field corresponding to the unperturbed and perturbed waveguides are separated. This made it possible to reconstruct the interferogram of the unperturbed field in the presence of intense internal waves. The relative error of its reconstruction is determined. The effect of a disturbance on the reconstruction of the distance and radial velocity of a source in the presence of a disturbance is estimated.

Keywords: shallow sea, interferogram, hologram, intense internal waves, mode interaction, moving sound source

UDC 004.052.34

Acknowledgments: This work was supported by the Russian Foundation for Basic Research (project no. 19-29-06075). The work of E.S. Kaznacheeva was supported by a grant from the President of the Russian Federation MK-6144.2021.4. The work of S.A. Tkachenko was supported by a grant from the President of the Russian Federation MK-4846.2022.4.

For citation: Venedikt M. Kuz'kin, Sergey A. Pereselkov, Elena S. Kaznacheeva, Vladimir I. Grachev, Sergey A. Tkachenko, Pavel V. Rybyanets. Holographic Processing of Moving Sources in a Shallow Sea with Intense Internal Waves. *RENSIT: Radioelectronics. Nanosystems. Information Technologies*, 2022, 14(2):197-204e. DOI: 10.17725/rensit.2022.14.197.

CONTENTS

1. INTRODUCTION (197)
 2. CHARACTERISTICS OF INTENSE INTERNAL WAVES (199)
 3. NUMERICAL SIMULATION (199)
 4. CONCLUSION (202)
- REFERENCES (203)

1. INTRODUCTION

The problem of detection and localization of low-noise underwater sources is one of the poorly developed problems in ocean acoustics. Difficulties in the approach to its solution stem from the limitations of the

applied mathematical models for describing the source signal. Currently, active interest from many scientific teams is attracted by the solution of the problem based on holographic processing based on stable structural features of the interference pattern of the sound field formed by a broadband sound source. We note the main works [1–4], where significant results were obtained in this direction for regular waveguides.

Holographic processing implements quasi-coherent accumulation of spectral density along localized fringes of an interference pattern (interferogram) in frequency-time variables. An interferogram is understood as the square of the module of the received signal in frequency-time variables. The location geometry of the localized bands is determined by the parameters of the waveguide, the speed and trajectory of the sound source. A two-dimensional Fourier transform (2D-FT) is applied to the accumulated spectral density of the interferogram. At the output of the integral transformation (hologram), the spectral density is localized in a narrow band in the form of focal spots corresponding to different numbers of interfering modes. The coordinates of the maxima of the focal spots are related to the radial velocity (velocity projection in the direction to the receiver) and the distance of the source through the spatial frequency scales of the interferogram variability. The interference spectral density on the interferogram accumulates incoherently and is distributed over the entire region of the hologram. Such a mechanism for distributing the spectral density of the noise emission of the source and interference provides high noise immunity of processing, significantly exceeding the noise immunity of known processing methods. The hologram

records the amplitudes of the interfering modes and the phase difference between them in all intermediate states that the source successively passes during the observation time. The physical and mathematical principles of hologram formation were first described in [1,2].

When developing holographic processing [1–4], it was assumed that the oceanic environment is homogeneous, i.e. its characteristics in the space-time domain are unchanged. In many cases of practical interest, information is transmitted against the background of hydrodynamic perturbations that distort the interferogram and increase the number of intense focal spots in the hologram. A particular aspect of the stability of holographic processing with respect to regular perturbations of the waveguide depth and sound velocity in the water column was analyzed in [5].

In the presence of hydrodynamic perturbations, the interferogram can be approximately represented as the sum of source interferograms formed by an unperturbed (in the absence of a perturbation) and a perturbed waveguide. The 2D-FT transformation is a linear process, which allows the hologram to be considered as a linear superposition of the unperturbed and perturbed waveguide holograms. If the spectral densities of the unperturbed and perturbed holograms are separated, then the holographic processing is stable against hydrodynamic perturbations. In this case, the inverse transformation of the 2D-FT to the allowed spectral densities of the holograms will make it possible to observe the unperturbed and perturbed interferograms of the source field.

In inhomogeneous media, holographic interferometry was first used when

processing data from the SWARM-95 experiment [6–8], when intense internal waves (IIWs) on a stationary path (stationary source and receiver) led to horizontal refraction and interaction of acoustic field modes. It was shown that holographic processing resolves the interferograms of the unperturbed and perturbed fields [9,10]. Shortly thereafter, this effect was theoretically described and confirmed by the results of numerical simulation, and the errors in the reconstruction of unperturbed interferograms were estimated [11,12].

In this paper, we present and discuss the results of numerical simulation of holographic processing of noise emission from a moving source (with a fixed receiver) in the presence of IIWs, which determine the interaction of acoustic field modes. The effect of IIWs on the error in reconstructing the distance, the radial velocity of the source, and the interferogram of the unperturbed field is estimated.

2. CHARACTERISTICS OF INTENSE INTERNAL WAVES

Intense internal waves are a hydrodynamic phenomenon that is widespread in the oceanic environment. In shallow water areas, they represent trains of intense short-period fluctuations of the water surface of constant density, interpreted as trains of solitons that propagate towards the coastline at a speed of $u \sim 0.5-1$ and are separated by periods of calm $\delta L \sim 10$ km, which makes the pattern of the internal wave field non-stationary. The reason for their occurrence is due to internal tides: on the shelf, energy is transferred from internal tidal waves to short-period ones [13]. According to the experimental data, the length of the trains is $L \sim 2-4$ km, the period is $\Lambda \sim 200-400$ m (the distance between the

crests of neighboring solitons), the half-width is $\eta \sim 50-150$ m, and the amplitude is $B \sim 10-30$ m [14-16]. Soliton trains are characterized by: a) anisotropy in the horizontal plane, the radius of curvature of the front is $r \sim 15-25$ km; b) quasi-sinusoidality in the direction of propagation, i.e. narrowness of the spatial spectrum; c) synchronism of vertical displacements in depth, which indicates the dominance of the first gravity mode. These properties determine the horizontal refraction and interaction of source field modes if the acoustic path is located at small and large angles to the soliton train wavefront, respectively [17,18].

3. NUMERICAL SIMULATION

To be able to compare the results of holographic processing for the cases of a stationary and moving source in the IIWs field, which determine the interaction of modes, the simulation data were chosen the same as in [12].

The depth distribution of the speed of sound is shown in Fig. 1. Two frequency

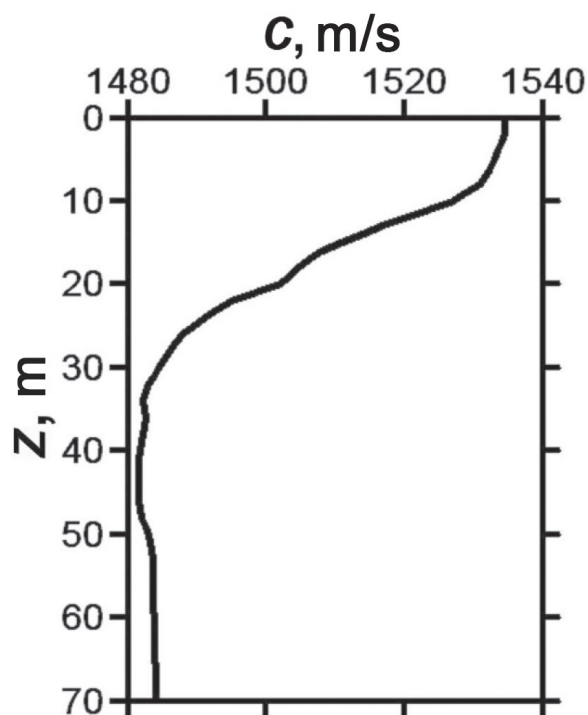


Fig. 1. Unperturbed sound velocity profile [8].

ranges were considered: $\Delta f_1 = 100-120$ Hz and $\Delta f_2 = 300-320$ Hz. Parameters of the liquid absorbing bottom: the ratio of the density of soil and water $\rho = 1.8$; for the first frequency range Δf_1 the complex refractive index $n = 0.84(1 + i0.03)$, for the second frequency range $\Delta f_2 - n = 0.84(1 + i0.05)$. In the frequency range Δf_1 the field was formed by $M = 4$ modes, in the frequency range $\Delta f_2 - M = 10$ modes. Mode propagation constants $h_m(\omega_0)$ and their frequency derivatives $(dh_m(\omega_0)/d\omega)$ at mid-range frequencies $f_0 = 110.310$ Hz are given in **Table 1, 2**. The scheme of the source movement relative to the IIW propagation is shown in **Fig. 2**.

At the initial time $t_0 = 0$, the distance between the moving source and the receiver is $x_0 = 10$ km. The source was located at a depth of $z_s = 12.5$ m, the receiver – at a depth of $z_q = 35$ m. The radial velocity of the source $w = -1$ m/s (when the source approaches the receiver, the radial velocity is negative, while moving away it is positive). A uniform spectrum was set. Pulses with duration $T = 4$ s (frequency sampling step 0.25 Hz) of sound pressure were recorded at intervals $T_* = 5$ s. The model of a single soliton was used. Soliton parameters: amplitude $B = 15$ m, half-width $\eta = 150$ m, velocity $u = 0.7$ m/s. The soliton moved in the direction from the source to the receiver, at the time $t_0 = 0$ it is removed from the receiver at a

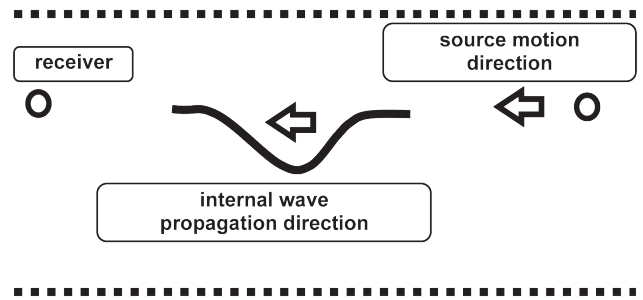


Fig. 2. Scheme of source motion in the IIW field.

distance $x = 5$ km. The observation time $\Delta t = 20$ min, during this time the soliton traveled the distance $\Delta x = 840$ m. The sound field at the receiving point was calculated within the modal approach of mode interaction.

The simulation results are shown in **Fig. 3-6**. The dotted line on the holograms shows the band in which the spectral density of the received signal is concentrated. Linear dimensions of the band: $\delta\tau \approx 0.15$ s, $\delta\nu \approx 0.002$ Hz, which is consistent with the theoretical estimates of the sizes of focal spots $\delta\tau = 0.1$ s, $\delta\nu = 0.0017$ Hz [1,2]. Here τ and ν are the time and frequency of the hologram.

Based on the first focal spot of the hologram closest to the origin, the radial velocity w and the initial distance x_0 are estimated as [1,2]

$$\dot{w} = -|k_w|v_1, \quad \dot{x}_0 = |k_x|\tau_1, \tag{1}$$

where

$$k_w = \frac{M-1}{h_{1M}(\omega_0)}, \quad k_x = \frac{M-1}{dh_{1M}(\omega_0)/d\omega}. \tag{2}$$

Here v_1 and τ_1 are the coordinates of the maximum of the first focal spot; h_m is the real part of the horizontal wave number of the m -th mode, $h_{1M} = h_1 - h_M$. The restored source parameters, in contrast to the model values, are indicated by a dot at the top.

Table 1

Frequency $f_0 = 110$ Hz.

Mode numbers, m	1	2	3	4
h_m, M^{-1}	0.4635	0.4557	0.4450	0.4310
$(dh_m/d\omega)/10^{-4}, c/M$	6.7624	6.8085	6.9014	7.0914

Table 2.

Frequency $f_0 = 310$ Hz.

Mode numbers, m	1	2	3	4	5	6	7	8	9	10
h_m, M^{-1}	1.3123	1.3073	1.3006	1.2920	1.2826	1.2730	1.2630	1.2525	1.2403	1.2258
$(dh_m/d\omega)/10^{-4}, c/M$	6.7511	6.7619	6.7813	6.7973	6.8080	6.8150	6.8312	6.8753	6.9703	7.0574

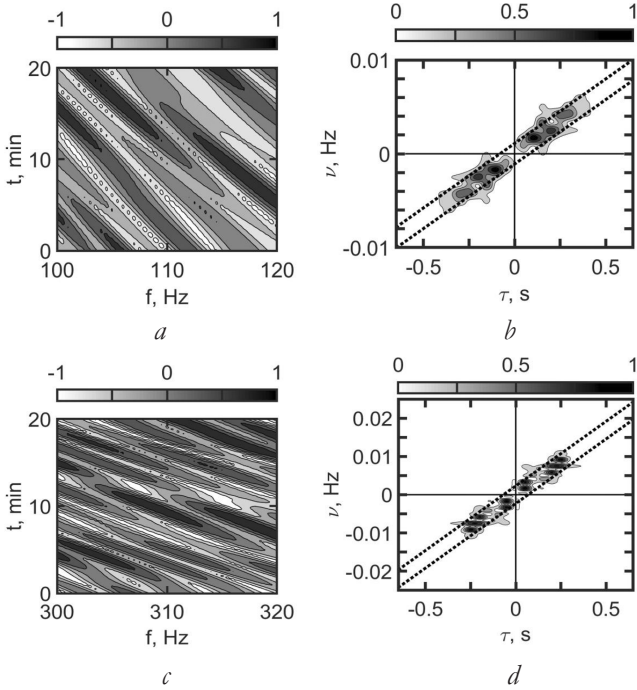


Fig. 3. Normalized interferograms (a, c) and holograms (b, d) in the absence of disturbance: (a, b) – frequency range Δf_1 , (b, d) – frequency range Δf_2 .

On **Fig. 3** shows the interferograms and moduli of the source field holograms in the absence of perturbation. Interference fringe slopes: $\delta f/\delta t \approx -0.016 \text{ s}^{-2}$ (frequency range Δf_1) and $\delta f/\delta t \approx -0.035 \text{ s}^{-2}$ (frequency range Δf_2). Coordinates of the peak of the first focal spot: $\tau_1 = 0.1 \text{ s}$, $\nu_1 = 1.71 \cdot 10^{-3} \text{ Hz}$ (Δf_1); $\tau_1 = 3.80 \cdot 10^{-2} \text{ s}$, $\nu_1 = 0.002 \text{ Hz}$ (Δf_2). According to (1) and the data of Table 1, 2 restored source parameters: $\dot{w} = -0.99 \text{ m/s}$, $\dot{x}_0 = 9.1 \text{ km}$ (Δf_1); $\dot{w} = -1.3 \text{ m/s}$, $\dot{x}_0 = 11.1 \text{ km}$ (Δf_2).

The interferograms and moduli of the source field holograms as the soliton moves along the path are shown in **Figs. 4**. Perturbation of the aquatic environment leads to distortions of localized fringes of interferograms and the appearance of additional intense focal spots of holograms compared to the unperturbed medium. The spectral density along the localized fringes of interferograms becomes highly nonuniform, acquiring the form of focal spots (Fig. 4(a,c)). This mechanism becomes

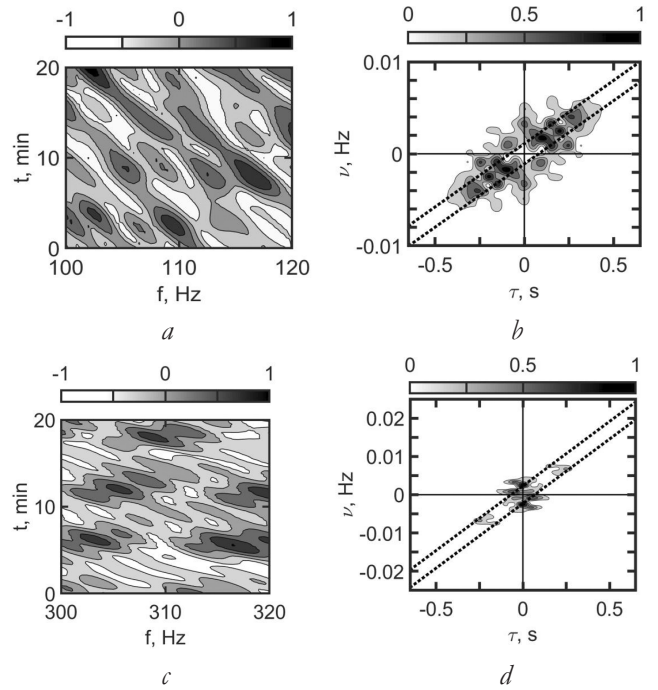


Fig. 4. Normalized interferograms (a, c) and holograms (b, d) in the presence of a disturbance: (a, b) – frequency range Δf_1 , (c, d) – frequency range Δf_2 .

more acute with an increase in the frequency range, which is explained by an increase in the effect of scattering by inhomogeneities with increasing frequency. In the holograms (Fig. 4(b,d)) with an increase in the frequency range, the concentration of the spectral density along the frequency axis increases, which indicates the predominant influence of the perturbation on the formation of the hologram appearance.

The results of cleaning the spectral densities of the holograms from the perturbed field in the vicinity of the frequency axis ν and their Fourier image are shown in **Figs. 5**. The shape of the arrangement of spectral densities on the holograms of the unperturbed waveguide (Fig. 3(b,d)) and reconstructed in the presence of a perturbation (Fig. 5(b,d)) are close to each other. The peak coordinates of the first focal spot are estimated as: $\tau_1 = 1.19 \cdot 10^{-1} \text{ s}$, $\nu_1 = 0.002 \text{ Hz}$ (Δf_1); $\tau_1 = 4.08 \cdot 10^{-2} \text{ s}$, $\nu_1 = 1.63 \cdot 10^{-3} \text{ Hz}$ (Δf_2). According to (1) and the data of Table 1, 2 restored source parameters

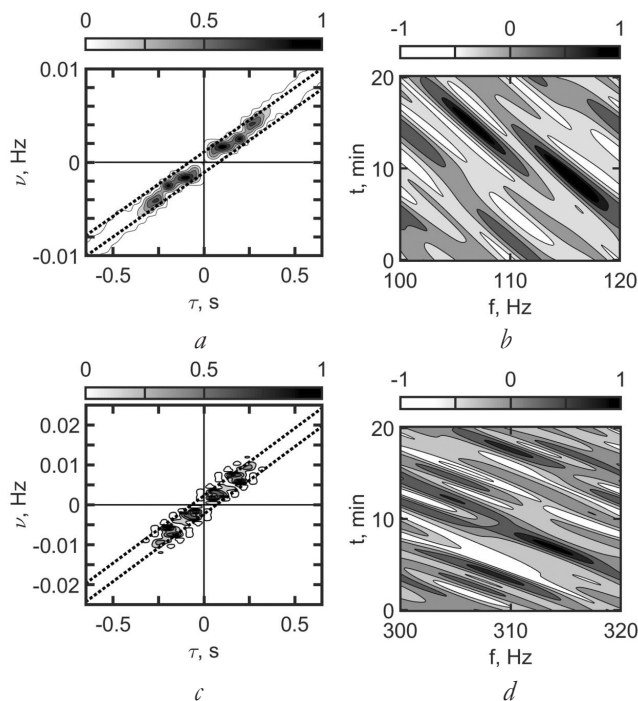


Fig. 5. Normalized filtered modules of holograms (*a*, *c*) of the unperturbed field and interferograms reconstructed from them (*b*, *d*): (*a*, *b*) – frequency range Δf_1 , (*c*, *d*) – frequency range Δf_2 .

$\dot{w} = -1.1$ m/s, $\dot{x}_0 = 10.8$ km (Δf_1); $\dot{w} = -1.1$ m/s, $\dot{x}_0 = 12.0$ km (Δf_2). The reconstructed interferograms of the unperturbed field in the presence of a disturbance are shown in Figs. 5(*b,d*). The slopes of the interference fringes are estimated as $\delta f/\delta t \approx -0.016$ s $^{-2}$ (Δf_1) and $\delta f/\delta t \approx -0.035$ s $^{-2}$ (Δf_2).

On **Fig. 6** shows one-dimensional normalized interferograms of unperturbed fields in the absence of a disturbance (solid line) and reconstructed (dots) in its presence. The normalized value is indicated at the top

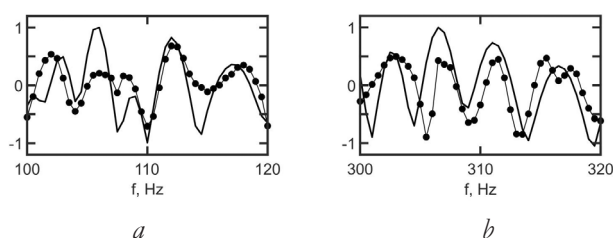


Fig. 6. Dependences of normalized one-dimensional interferograms of unperturbed fields on frequency f in the absence of a disturbance (solid line) and reconstructed in its presence (dots): (*a*) frequency range Δf_1 , (*b*) frequency range Δf_2 .

with the “lid” icon. The interferograms are horizontal sections of the corresponding two-dimensional interferograms (Fig. 3, 5). The error in the reconstruction of interferograms will be characterized by the quantity

$$d = \frac{\sum_{j=1}^J |I_1(f_j) - I_2(f_j)|}{\sum_{j=1}^J |I_1(f_j)|}, \quad (3)$$

where the number of samples $J = 80$. Here $I_{1,2}$ is the interferogram of the unperturbed field in the absence of perturbation and reconstructed in its presence, respectively. For the frequency range Δf_1 Hz, the error is $d = 0.635$, for the frequency range Δf_2 Hz – $d = 0.821$. Compared to a stationary source [12], the error increased by a factor of 45.4 and 11.1 times for the frequency ranges Δf_1 and Δf_2 , respectively. The indicated difference in the error values is explained by the different character of the medium variability. With a stationary source, there is a temporal variability of the oceanic environment, and with a moving source, there is a spatio-temporal variability. Thus, in the case of a moving source in the presence of IIW, the interferogram of the unperturbed field is not restored.

4. CONCLUSION

On the basis of numerical simulation data, the stability of the holographic method for detecting and localizing a moving underwater source against the background of IIWs, which determine the interaction of sound field modes, is considered.

In the case of a moving source, IIWs cause spatio-temporal variability of the aquatic environment, which leads to more significant distortions of the interferogram of the unperturbed field compared to a stationary source. In the presence of such strong distortions in the hologram, the

spectral density in the form of intense focal spots is concentrated mainly in the region of the frequency axis, which indicates the predominant effect of IIWs on the formation of the hologram. An essential factor in the formation of a hologram, as in the case of a stationary source, is the possibility of separating the spectral densities of the perturbed and unperturbed fields. This makes it possible to restore the hologram of the unperturbed field of a moving source with minimal distortions in the presence of IIWs and to estimate its parameters.

The results of the numerical experiment demonstrated the stability of the holographic method for detecting and localizing a moving underwater source against the IIWs sbackground. In the presence of IIWs and in their absence, the estimates of the radial velocity and remoteness of the source are close to each other. In contrast to a stationary source, in the case of a moving source, in the presence of IIWs, it is impossible to restore the interferogram of the unperturbed field. In this case, however, the angular coefficients of the interference fringes practically remain unchanged.

REFERENCES

1. Kuznetsov GN, Kuzkin VM, Pereselkov SA. Spectrogram and localization of a sound source in a shallow sea. *Acoustical Physics*, 2017, 63(4):449-461. DOI: 10.1134/S1063771017040078.
2. Kaznacheev IV, Kuznetsov GN, Kuzkin VM, Pereselkov SA. Interferometric method for detecting a moving sound source with a vector-scalar receiver. *Acoustical Physics*, 2018, 64(1):37-48. DOI: 10.1134/S1063771018010104.
3. Emmetiere R, Bonnel J, Gehant M, Cristol X, Chonavel Th. Understanding deep-water striation patterns and predicting the waveguide invariant as a distribution depending on range and depth. *J. Acoust. soc. Am.*, 2018, 143(6):3444-3454.
4. Emmetiere R, Bonnel J, Cristol X, Gehant M, Chonavel T. Passive source depth discrimination in deep-water. *IEEE J. of Selected Topics in Signal Processing*, 2019, 13(1):185-197.
5. Pereselkov SA, Kuz'kin VM. Interferometric processing of hydroacoustic signals for the purpose of source localization. *J. Acoust. soc. Am.*, 2022, 151(2):666-676.
6. Apel JR, Badiy M, Chiu C-S, Finette S, Headrick RH, Kemp J, Lynch JF, Newhall AE, Orr MH, Pasewark BH, Tielburger D, Turgut A, von der Heydt K, Wolf SN. An overview of the SWARM 1995 shallow-water internal wave acoustic scattering experiment. *IEEE J. Ocean. Eng.*, 1997, 22:465-500.
7. Frank SD, Badiy M, Lynch J, Siegmann WL. Analysis and modeling of broadband airgun data influenced by nonlinear internal waves. *J. Acoust. soc. Am.*, 2004, 116(6):3404-3422.
8. Badiy M, Katsnelson BG, Lynch JF, Pereselkov S, Siegmann WL. Measurement and modeling of three-dimensional sound intensity variations due to shallow-water internal waves. *J. Acoust. soc. Am.*, 2005, 117(2):613-625.
9. Kuz'kin VM, Pereselkov SA, Zvyagin VG, Malykhin AYu, Prosovetskiy DYu. Intense internal waves and their manifestation in interference patters of received signals on oceanic shelf. *Phys. wave phenom.*, 2018, 26(2):160-167.
10. Badiy M, Kuz'kin VM, Lyakhov GA, Pereselkov SA, Prosovetskiy DYu,

- Tkachenko SA. Intense internal waves and their manifestation in the interference patterns of received signals on oceanic shelf. Part II. *Phys. wave phenom.*, 2019, 27(4):313-319.
11. Kaznacheeva ES, Kuz'kin VM, Pereselkov SA. Interferometric processing of hydroacoustic information in the presence of intense internal waves. *Phys. wave phenom.*, 2021, 29(3):278-284.
 12. Kuzkin VM, Lyakhov GA, Pereselkov SA, Kaznacheeva ES. Transmission of information through a randomly inhomogeneous oceanic medium. *Fundam. appl. hydrof.*, 2021, 14(2):54-64.
 13. Konyaev KV, Sabinin KD. *Waves inside the ocean*. St. Petersburg, Gidrometeoizdat Publ., 1992, 271 p.
 14. Zhou J, Zhang XZ, Rogers PH. Resonant interaction of sound wave with internal solitons in the coastal zone. *Acoust. soc. Am.*, 1991, 90(4):2042-2054.
 15. Silver AN. Manifestation of the properties of solitons in internal waves on the shelf. *Izv. Academy of Sciences of the USSR, Physics of the atmosphere and ocean*, 1993, 29(2):285-293.
 16. Hsu MK, Liu AK, Liu C. An study of internal waves in the China seas and yellow sea using SAR. *Continental Shelf Res.*, 2000, 20(4-5):389-410.
 17. Katsnelson BG, Pereselkov SA. Low-frequency horizontal acoustic refraction caused by internal wave solitons in a shallow sea. *Acoustical Physics*, 46(6):684-691. DOI: 10.1134/1.1326723.
 18. Katsnelson BG, Pereselkov SA. Space-Frequency Dependence of the Horizontal Structure of a Sound Field in the Presence of Intense Internal Waves. *Acoustical Physics*, 50(2):169-176. DOI: 10.1134/1.1675872.

DOI: 10.17725/rensit.2022.14.205

Long-term phosphorescence in cooled organic substances solid solutions – temporal dynamics and spectral memory effect

^{1,2}Dmitry Yu. Tsipenyuk

¹Prokhorov General Physics Institute of the Russian Academy of Sciences, <http://gpi.ras.ru/>
Moscow 119991, Russian Federation

²Moscow Polytechnic University, <https://new.mospolytech.ru/>
Moscow 107023, Russian Federation

E-mail: tsip@kapella.gpi.ru

Alexander V. Voropinov

Laser Graphic Art Ltd., <http://www.lasergraphicart.com/>
Moscow 105318, Russian Federation

E-mail: avv@lasergraphicart.com

Received April 15, 2022, peer-reviewed April 22, 2022, accepted April 29, 2022

Abstract: The paper presents the results of delayed phosphorescence study in organic substances solid solutions at cryogenic temperatures. This work continues the series of our works devoted to the study of the physical mechanism of excitation of long-term phosphorescence and the prospects for creating new active laser media based on an analogue of the Shpolsky matrix. The article also describes the observed effect of spectral memory in solid organic solutions upon excitation of long-term delayed phosphorescence by radiation from a mercury lamp.

Keywords: Long-term phosphorescence, organic compounds, cryogenic temperature, Shpolsky matrix, solid solutions, spectral memory effect

PACS: 78.45.+h, 78.47.+p, 78.90.+t

Acknowledgements: The authors express their gratitude for the assistance in carrying out measurements to the Center for Collective Use "Technological and Diagnostic Center for the Production, Research and Certification of Micro- and Nanostructures" of the Prokhorov General Physics Institute of the Russian Academy of Sciences and the company "LaserGraphicArt Ltd."

For citation: Dmitry Yu. Tsipenyuk, Alexander V. Voropinov. Long-term phosphorescence in cooled organic substances solid solutions – temporal dynamics and spectral memory effect. *RENSIT: Radioelectronics. Nanosystems. Information technologies*, 2022, 14(2):205-212e. DOI: 10.17725/rensit.2022.14.205.

CONTENTS

1. INTRODUCTION (205)
 2. DESCRIPTION OF THE INSTALLATION AND MEASUREMENT TECHNIQUE (207)
 3. EXPERIMENTAL RESULTS AND DISCUSSION (209)
 4. CONCLUSION (210)
- REFERENCES (211)

1. INTRODUCTION

Complex organic compounds under normal conditions have luminescence spectra in the form of continuous wide bands. Because of this, it is difficult to extract information about the structure of molecules and their composition from such spectra. To solve this problem, E.V. Shpolsky and his collaborators [1-3] proposed in the middle of the last century to use the

effect discovered by them of the appearance of quasilinear electronic-vibrational spectra in complex organic compounds cooled to cryogenic temperatures. This effect allowed researchers to analyze spectra consisting of narrow spectral lines instead of broadband spectra. Subsequently, the development of research methods based on the Shpolsky effect led to the creation of optical selective laser spectroscopy of impurity molecules in solid solutions [4-6]. At present, optical spectroscopy of impurity molecules in solid solutions is widely used in solving problems in biophysics, quantum optics, physical chemistry, and technological applications.

In [7-8], the authors proposed the creation of active laser media based on analogues of the Shpolsky matrices. An experimental setup created for these purposes is described. This setup makes possible to study the phosphorescence of matrices cooled up to cryogenic temperatures. In the experiments described in [8-10], the “photon flame” effect previously discovered in [11] was additionally investigated. “Photon flame” is a long-term phosphorescence from 1 to 12 s when nanostructured matrices based on artificial opal SiO_2 are excited by a single-mode radiation of a giant ruby laser pulse.

The matrices were filled with various liquids based on organic substances (acetone, ethanol) and cooled up to liquid nitrogen temperature. Based on the results of processing the experimental data obtained in [8-9], it was concluded that ultralong-term phosphorescence (up to 60 s) in solid solutions of organic substances frozen to cryogenic temperatures can be initiated without the use of single-mode laser radiation and an opal matrix. It turned out that to excite ultra-high-power phosphorescence, it is sufficient to apply broadband radiation from a mercury lamp in the region of 240-310 nm as a pump.

In [10], studies of the temporal and spectral characteristics of ethanol $\text{C}_2\text{H}_5\text{OH}$, isopropyl $\text{CH}_3\text{CH}(\text{OH})\text{CH}_3$, and benzyl $\text{C}_6\text{H}_5\text{CH}_2\text{OH}$ alcohols cooled to cryogenic temperatures were continued when their phosphorescence spectra were excited for 10 s by ultraviolet radiation from a mercury lamp.

An analysis of the data obtained in [7-10] and literature [12-18] allows us to conclude that the phosphorescence spectra of various substances cooled to cryogenic temperatures can degrade over time, and the spectrum itself can “shift” depending on the phosphorescent molecule or atom matrix in which it is “placed”.

Several mechanisms are proposed to explain the microscopic effects of the radiation of an artificial opal arising in a crystal under the action of high-power pulsed laser radiation: the mechanism of four-photon parametric scattering and the mechanism of successive three-frequency wave interactions in periodically inhomogeneous media. In this case, the efficiency of stimulated emission in the blue-green region is provided by anomalies in the density of photon states near the edges of the Brillouin zone. The effect is observed only at low temperatures, since then the relaxation processes of photon decay with the transition of light energy into the thermal energy of the crystal lattice are suppressed [11].

We believe that the long afterglow in the blue-green region of ethyl alcohol or acetone samples frozen to cryogenic temperatures under the influence of pumping with ultraviolet radiation indicates the possibility of other, non-threshold mechanisms for the occurrence of this phenomenon, not related to photonic crystals and pulsed laser radiation.

It was also found in [8] that with increasing temperature, the afterglow effect decreases and in the region of 165 K the effect disappears. In this case, the main spectrum of long-term phosphorescence of the substances studied in

[8] is in the region of 400-555 nm. The relative intensity of the phosphorescence spectra of the studied samples differs markedly. For example, as was found in [9] from a comparison, the relative intensity under the same conditions of excitation of phosphorescence in Kalosha gasoline is about 3000 rel. units, for immersion oil – about 1800 rel. units, while ethanol has only 180 rel. units.

There is also a difference in the temporal dynamics of the phosphorescence spectra shapes of various substances. Over time, the phosphorescence spectra of ethanol and Kalosha gasoline decay proportionally over the entire range from 300 to 600 nm [9]. At the same time, the decay dynamics of the phosphorescence spectrum of immersion oil is different: the short-wavelength part (range 350-425 nm) of the phosphorescence spectrum decays faster than the long-wavelength part (range 475-525 nm), as a result of which the shape of the spectra recorded after 0.5 and 1.0 s is significantly differs from the spectra shape recorded after 2.0 and 5.5 s.

The effect of long-term phosphorescence is usually associated with a nonradiative transition in the triplet radiation scheme [10-17]. At the same time, the authors of the article consider other possible models for describing this phenomenon. For example, related to the mechanism of capture and long-term retention of electromagnetic radiation by the field of an atom or molecule within the framework of the extended space model [19-20].

In the presented work, new results of our experimental studies of the spectral characteristics of phosphorescence of organic substances cooled to the temperature of liquid nitrogen are presented. In particular, the observed effect of spectral memory in solid organic solutions upon excitation of long-term phosphorescence by radiation from a mercury lamp is described.

2. DESCRIPTION OF THE INSTALLATION AND MEASUREMENT TECHNIQUE

To study the spectral properties of organic substances cooled up to the temperature of liquid nitrogen, a laboratory setup was created, which is schematically shown in **Fig. 1**. A pulsed YAG:Nd³⁺ laser with a frequency doubler (radiation wavelength 1064, 532 nm, 15 mJ/pulse, 15 ns duration, repetition rate 50 Hz) or continuous radiation from a DRT-230 mercury lamp could be used as a pump source in the setup.

The pump radiation from a mercury lamp 1 passed through a replaceable light filter combined with a mechanical radiation interrupter 2. Next, the radiation was focused onto the surface of the test sample using a collimator 3, a rotary prism 4, and a focusing quartz lens 5 into liquid nitrogen, which was poured into a thermos cuvette open at the top. The time of irradiation of samples with pump radiation varied and ranged from several minutes to 5 s in different experimental series.

The phosphorescence of the samples was recorded by a digital spectrum analyzer 7

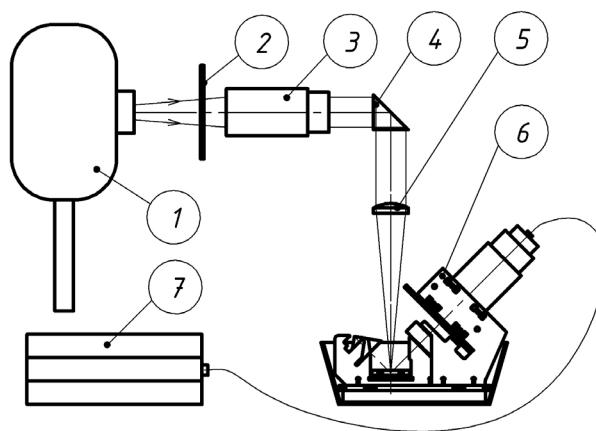


Fig. 1. Installation diagram. 1 – mercury lamp; 2 – replaceable light filter/mechanical radiation interrupter; 3 – collimator of a mercury lamp; 4 – rotary prism; 5 – focusing lens; 6 – sample exposure unit; 7 – spectrometer.

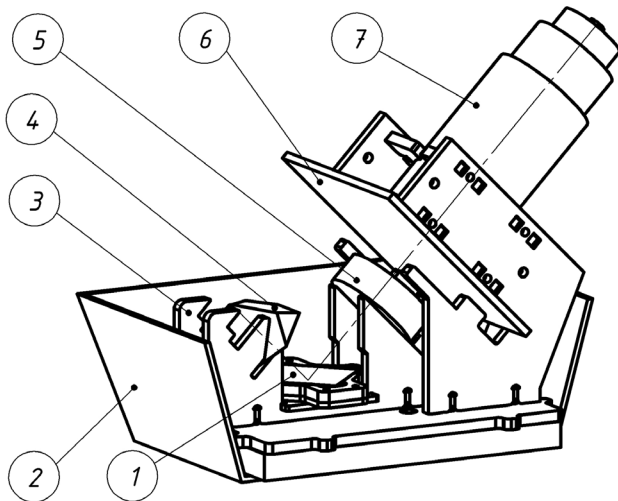


Fig. 2. Arrangement of the sample exposure unit. 1 – frozen sample; 2 – cell body for liquid nitrogen (section); 3 – constructive from PMMA (polymethyl methacrylate); 4 – replaceable rear mirror (trippelprism); 5 – replaceable front mirror; 6 – replaceable light filter; 7 – collimator of the light guide of the spectrometer.

connected to a computer or a digital camera after the pump radiation was blocked by a mechanical chopper.

Fig. 2 shows in more detail the arrangement of the unit for exposing samples, which is schematically shown. When designing the assembly for exposure, we took into account the features in measuring the optical characteristics of the Shpolsky matrices, which we obtained in the study of similar objects [7-8].

The design of the exposure unit made it possible to work with samples of organic substances partially immersed in liquid nitrogen without fogging the prism/mirrors 4, 5 and collimator 7. To measure the phosphorescence spectra, the cooled sample was illuminated by pump radiation for 30-60 s. After the end of irradiation, the light flux from the mercury lamp was mechanically blocked by an opaque metal shutter. Before measuring the experimental spectra, we recorded the control noise spectrum of the ruler, which was then subtracted from the working spectra. The exposure time of the noise and experimental

spectra in each experimental series was the same. To estimate the scatter in the intensity of the spectral data, series of 10-15 spectra of the same samples were recorded under the same conditions. The resolution of the Ocean Optics HR4000 spectrometer was about 0.75 nm/channel, the measurement range was 200-1100 nm.

Fig. 3 shows the spectrum of scattered radiation of a DRT-230 mercury lamp from liquid nitrogen in a steel cell, obtained on our experimental setup.

It should be noted that the radiation of a mercury lamp depends on the design and type of the lamp (DRT-230 is an arc mercury-helium high-pressure quartz lamp) and is variable in time as the mercury lamp heats up during operation [21,22]. Therefore, when using a mercury lamp as a fluorescence excitation source, in each series of experiments, before and at the end of the measurements, we controlled the initial radiation spectrum from the DRT-230. According to the manufacturer's passport data, the power consumption of the DRT-230 lamp is 230 W, the radiant flux in the range $\lambda = 240-320$ nm is 24.6 W, and the radiation power distribution in regions A, B, and C with respect to the entire radiation power: region A: 315-400 nm – 21%; region B: 280-315 nm – 25% and region C: 230-280 nm – 11%. As can be seen from Fig. 3, the strongest emission lines

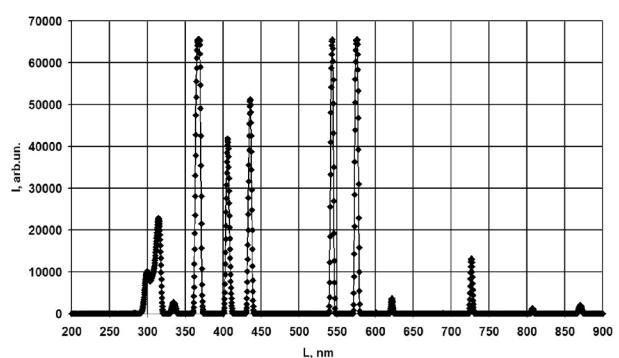


Fig. 3. Scattered radiation spectrum of a DRT-230 mercury lamp in liquid nitrogen in a steel cell.

of DRT-230 are located in the areas: 300-315; 336; 368; 406; 435; 544; 576; 622 and 727 nm.

When conducting research, we also took into account the results of studies of the spectral composition and temporal dynamics of radiation from various types of mercury lamps [21-22].

The measurement technique described above allowed us to control the spectral parameters of the exciting radiation and consistently obtain well-repeated results of spectral measurements from identical samples in different experimental series.

3. EXPERIMENTAL RESULTS AND DISCUSSION

Below we present the results of further studies initiated in a series of works [7-10].

The magnitude of the excitation efficiency of long-term phosphorescence at cryogenic temperatures was studied in complex organic substances having a similar composition.

As samples for comparison, we examined Cosmofen PMMA Cosmo SL-650.110 diffuse adhesives; Cosmo SL-650.120 and Cosmo SL-660.210 (manufactured by Weiss Chemie). Cosmo SL-650.110 and Cosmo SL-650.120 are PMMA diffuse acrylic adhesives in solvent. The SL-650.110 specified by the manufacturer contains dichloromethane CH_2Cl_2 , acetone $\text{C}_3\text{H}_6\text{O}$ and butanone $\text{C}_4\text{H}_8\text{O}$, in contrast to the specified Cosmo SL-650.120. It was found that under the same excitation conditions, the relative intensity of the phosphorescence spectra of Cosmo SL-650.110 is approximately 70 times greater than that of Cosmo SL-650.120 **Fig. 4**.

In Fig. 4, the phosphorescence intensity of Cosmo SL-650.110 cooled to 77.4 K is displayed on a logarithmic scale and refers to the left scale, and the intensity of the phosphorescence spectrum of SL-650.120

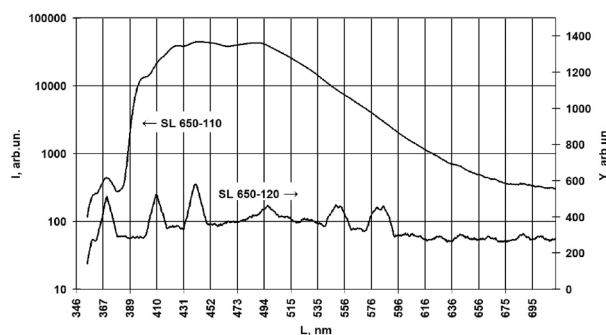


Fig. 4. Phosphorescence spectra of cooled to 77.4 K Cosmo SL-650.110 and Cosmo SL-650.120 exposure 200 ms, the spectra were recorded 400 ms after the excitation radiation from the DRT-230 mercury lamp was blocked.

cooled to 77.4 K refers to the linear scale located in Fig. 4 on the right.

Such a large difference in the intensity of the excited phosphorescent spectra can be attributed to the above three substances that are included in Cosmo SL-650.110 and are absent in Cosmo SL-650.120.

However, in our further experiments with Cosmo SL-650.120, which contains both acetone $\text{C}_3\text{H}_6\text{O}$ and butanone $\text{C}_4\text{H}_8\text{O}$, an extremely weak delayed phosphorescence was recorded. Therefore, we come to the conclusion that almost two orders of magnitude more efficient excitation of phosphorescence in the Cosmo SL-650.110 sample cooled to liquid nitrogen temperature compared to Cosmo SL-650.120 and in Cosmo SL-650.120 is associated only with the presence of dichloromethane CH_2Cl_2 in its composition.

It is necessary to note one more effect that we discovered in the study of the phosphorescence spectra of organic substances cooled to cryogenic temperatures. On the phosphorescence spectra of Cosmo SL-650.110 and Cosmo SL-650.120 Fig. 4, one can see broad lines that coincide with the arrangement of emission lines of a mercury lamp. From the comparison of Fig. 3 and

Fig. 4, it can be seen that the Cosmo SL-650.120 sample has broad lines in the 363-372 nm regions in the phosphorescence spectrum; 402-410; 431-448; 539-558 and 570-590 nm corresponding to the arrangement of emission lines of a mercury lamp. For the Cosmo SL-650.120 sample, the spectrum shown in Fig. 4 this effect is clearly visible in the region of 363-372 nm, relatively weakly in the regions of 402-410; 431-448 nm, and is not observed in the regions of 539-558 and 570-590 nm. This effect of the spectral memory of organic substances cooled to 77.4 K was recorded on the phosphorescence spectra recorded 400 ms after the complete overlap of radiation from the DRT-230 source, with an exposure time of 200 ms.

A similar result, in the time range from 0.2 to 8.0 s, was obtained by us in the study of phosphorescence of isopropanol C₃H₈O cooled to 77.4 K. On **Fig. 5** shows the temporal dynamics of the phosphorescence spectra of isopropanol. The total time of visually observed superlong phosphorescence

of isopropanol cooled to a temperature of 77.4 K was about 60 s.

As can be seen from the data shown in Fig. 5, the effect of spectral memory in solid organic solutions cooled to 77.4 K upon excitation of long-term phosphorescence by radiation from a mercury lamp is well observed in isopropanol in the range of time delays from 0.2 to 3.2 s.

In this case, as can be seen, the dynamics of the effect is different in different wavelength ranges. Comparison of the attenuation of broad lines of isopropanol phosphorescence in areas coinciding with the radiation of a mercury lamp in the ranges: 363-372; 402-410; 431-448; 539-558 and 570-590 nm shows that in the regions of 363-372 and 431-448 nm the effect of spectral memory is manifested in all seven spectra; in area 402-410; 539-558 and 570-590 nm the effect is reliably identified only in the first two spectra taken with a delay of 200 and 400 ms.

4. CONCLUSION

Many works have been devoted to the study of the spectral properties of organic and inorganic substances at cryogenic temperatures [23-30]. Literature analysis allows us to draw the following conclusions: the effect of long-term phosphorescence is usually associated with a nonradiative transition in the triplet radiation scheme. It was also been found that the phosphorescence spectra of samples can degrade over time. The phosphorescence spectrum can also be shifted to the short-wavelength or long-wavelength region, depending on the matrix in which the phosphorescent molecule or atom is "placed".

Our results are in qualitative agreement with the above properties of cryogenic phosphorescence of organic compounds described in the authors' works [3-6;12-18]. Experimental results show the promise of

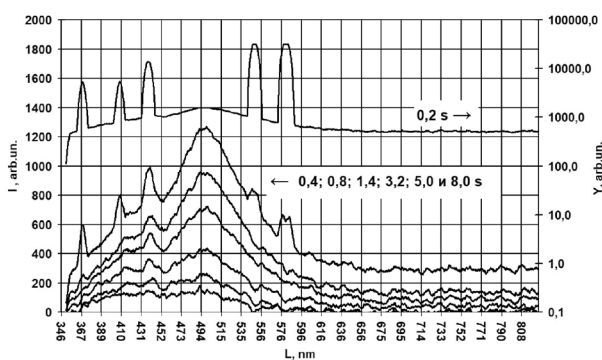


Fig. 5. Time dynamics of phosphorescence spectra of isopropanol cooled to 77.4 K. The exposure time of the spectra is 200 ms, the delay times of the recorded spectra are from 0.2 to 8.0 s. The spectrum taken with a delay of 0.2 s corresponds to the right logarithmic intensity scale, the remaining spectra with delays from 0.4 to 8.0 s corresponds to the left linear scale.

studying the possibility of creating cryogenic lasers based on organic compounds [7-8].

The observed effect of spectral memory in solid solutions of organic substances cooled to cryogenic temperatures upon excitation of phosphorescence by radiation from a mercury lamp deserves further detailed experimental study in the opinion of the authors.

The studies carried out indicate the possibility of the appearance in the sample of a potential well capable of capturing and retaining optical radiation for a long time in solid solutions of organic substances cooled up to a liquid nitrogen temperature of 77.4 K under the influence of the ultraviolet part of the radiation of a mercury lamp shorter than 300 nm.

To describe this phenomenon, we plan to study in subsequent works the possibility of using the mechanism of capture and long-term retention of electromagnetic radiation by the field of an atom or molecule as a model for describing this phenomenon within the framework of the extended space model [19-20].

REFERENCES

1. Shpolsky EV, Ilyina AA, Klimova LA. Fluorescence spectrum of Koronen in frozen solutions. *DAN SSSR*, 1952, 87(6):935 (in Russ.).
2. Shpol'skii EV. Problems of the Origin and Structure of Quasiline Spectra of Organic Compounds at Low Temperatures. *UFN*, 1962, 77:321-336 (in Russ.).
3. Shpolsky EV. Emission Spectral Analysis of Organic Compounds. *UFN*, 1959, 68:51 (in Russ.).
4. Naumov AV. Spectroscopy of organic molecules in solid matrices at low temperatures: from the Shpolsky effect to laser luminescence spectroscopy of all efficiently emitting single molecules. *UFN*, 2013, 183:633-652 (in Russ.).
5. Orrit M, Bernard J, Personov RI. High-resolution spectroscopy of organic molecules in solids: from fluorescence line narrowing and hole burning to single molecule spectroscopy. *J Phys. Chem.*, 1993, 97(40):10256.
6. Naumov AV, Weiner YuG. Single molecules as spectral nanoprobe for diagnostics of dynamic processes in solid media. *UFN*, 2009, 179:322-328 (in Russ.).
7. Voropinov AV, Tsipenyuk DYu. Active laser media based on the Shpolsky effect. *Sat. scientific works "Lasers in science, technology, medicine"*, M., 2018, 29:93. eLIBRARY ID: 35454387.
8. Aleshin YuK, Tsipenyuk DYu, Platonov VN, Voropinov AV. Development of a laser generator based on an analogue of the Shpolsky matrix. *Vestnik Moscow university, Ser. Phys. Astron.*, 2019, 1:48-51 (in Russ.).
9. Aleshin YK, Tsipenyuk DYu and Voropinov AV. The Time Characteristics and Phosphorescence Spectra of Cooled Carbon-Containing Analogues of the Shpolsky Matrix. *Moscow Univ. Phys. Bull.*, 2020, 75:148.
10. Voropinov AV, Tsipenyuk DYu, Shevchenko MA, Umanskaya SF, Mironova TV, Tcherniega NV, Kudryavtseva AD. Long-term luminescence in organic liquids at low temperatures. *Laser Phys. Lett.*, 2021, 18(7):075301. DOI: 10.1088/1612-202X/ac063a.
11. Gorelik VS, Kudryavtseva AD, Tareeva MV, Chernega NV. Spectral characteristics of the radiation of crystals of artificial opal under the effect of a photon flame. *Pis'ma v Zh. Èksper. Teoret. Fiz.*, 2006, 84(9):575-578; *JETP Letters*, 2006, 84(9):485-488.

12. Minkoff GJ. *Frozen Free Radicals*. N-Y, Interscience Publishers Inc., 1960, 144 p.
13. Zhongfu An, Chao Zheng, Ye Tao, Runfeng Chen, Huifang Shi, Ting Chen, Zhixiang Wang, Huanhuan Li, Renren Deng, Xiaogang Liu, Wei Huang. Stabilizing triplet excited states for ultralong organic phosphorescence. *Nature Materials*, 2015, 14(7):685-690. DOI: 10.1038/nmat4259.
14. Zhdanova NV, Deryabin MI. Phosphorescence spectrum and kinetics of dibromodiphenylene sulfide in n-hexane at 77 K. *Nauka. Innovations. Technologies. Physical and mathematical sciences*, 2016, 1:7-16.
15. Kirko DL. Luminescence of liquid nitrogen after pulsed exposure to ultraviolet radiation. *Fizika Nizkikh Temperatur*, 2015, 41(4):393-398. *Low Temperature Physics*, 2015, 41:303. DOI: 10.1063/1.4918956.
16. Kirko DL, Savelov AS, Kadetov VA. Study of glowing regions in liquid nitrogen. *Pis'ma Zh.Tekh. Fiz.*, 1995, 21:78.
17. Brown DC. The promise of cryogenic solid-state lasers. *IEEE J. Sel. top. Quantum Electron.*, 2005, 11(3):587-599.
18. Emanuel NM, Kuzmin MG (Eds.). *Experimental methods of chemical kinetics*. Moscow, Lomonosov MSU Publ., 1985, 384 p.
19. Andreev VA, Tsypenyuk DYu. Electromagnetic and gravitational fields in a 5-dimensional extended space model, their localization and interaction with matter. *RENSIT: Radioelectronics. Nanosystems. Information technologies*, 2019, 11(2):93-102; doi: 10.17725/rensit.2019.11.093.
20. Tsipenyuk DYu, Belyaev VB. Shell structures in microphysical objects in a 5-D extended space model. *RENSIT: Radioelectronics. Nanosystems. Information technologies*, 2019, 11(3):249-260; doi: 10.17725/rensit.2019.11.249.
21. Konyushenko I. Mini-spectrometers of the MS series from Hamamatsu. *Components and technologies*, 2021, 127(2):24-26, <https://kit-e.ru/sensor/mini-spektrometry-serii-ms-firmy-hamamatsu/>.
22. Avramenko EV, Kamskova EA, Pestov IE, Smirnov YuYu, Sherstobitova AS, Yaskov AD. Time dependence of the mercury emission spectrum - helium lamp DRGS-12. *Measuring Equipment*, 2015, 58(3):39-40.